CHALMERS

Development of Separation Phenomena on a Passenger Car

SABINE BONITZ

Department of Mechanics and Maritime Sciences
Vehicle Engineering & Autonomous Systems
CHALMERS UNIVERSITY OF TECHNOLOGY
Göteborg, Sweden 2018

THESIS FOR THE DEGREE OF DOCTOR OF PHILOSOPHY IN THERMO AND FLUID DYNAMICS

Development of Separation Phenomena on a Passenger Car

SABINE BONITZ

Department of Mechanics and Maritime Sciences

Vehicle Engineering & Autonomous Systems

CHALMERS UNIVERSITY OF TECHNOLOGY

Göteborg, Sweden 2018

Development of Separation Phenomena on a Passenger Car
SABINE BONITZ
ISBN 978-91-7597-785-0

Doktorsavhandlingar vid Chalmers tekniska högskola
Ny serie nr. 4466
ISSN 0346-718X
Department of Mechanics and Maritime Sciences
Vehicle Engineering & Autonomous Systems
Chalmers University of Technology
SE-412 96 Göteborg
Sweden
Telephone: +46 (0)31-772 1000

Chalmers Reproservice
Göteborg, Sweden 2018

Development of Separation Phenomena on a Passenger Car
Thesis for the degree of Doctor of Philosophy in Thermo and Fluid Dynamics
SABINE BONITZ
Department of Mechanics and Maritime Sciences
Vehicle Engineering & Autonomous Systems
Chalmers University of Technology

Abstract

The general shape of a vehicle influences its aerodynamic performance through separation phenomena and flow structure development. Since these flow characteristics have a direct influence on the energy efficiency, safety and comfort, it is essential to study their formation and evolution into the freestream. The energy efficiency is determined by the aerodynamic drag, while the safety and comfort aspects are dependent on the noise generation, vehicle soiling, handling and stability.

The objective of this work is to achieve a more detailed physical understanding of the development of flow structures by analysing their surface properties and their evolution into the freestream. The concept of limiting streamlines is used to investigate and characterize the near wall flow, and surface properties such as the surface pressure, the wall shear stress and the vorticity are analysed and correlated with the flow patterns. The detachment of the flow from the surface and its development into the freestream are investigated using 2D streamlines and flow properties such as vorticity.

This study is based on numerical simulations of a detailed full scale passenger car of the notchback type. Results are compared to experimental flow visualisations and pressure measurements performed on a full scale vehicle. Special focus is put on the flow around the antenna, the flow over the rear window, the flow downstream of the front wheel and on the base wake flow.

Based on this analysis, it is found that the surface patten can be used to identify evolving flow phenomena. Analysing the limiting streamline pattern and 2D planes, together with the vorticity distribution, makes it possible to predict and study occurring flow phenomena. Flow structures developing in the main flow direction were the most dominant and are the least suppressed. It is shown that the only mechanisms, of flow detaching from the surface, must be either through singular points or along separation lines.
The study of particular areas around the vehicle shows different flow phenomena and explains the formation of flow structures. Familiar phenomena such as the A-pillar vortex and the trailing vortices behind the vehicle are discussed. For instance, it is shown that, in the near wake an up-wash zone is created (crucial for contamination) and in the far wake, the two trailing vortices create a down-wash; both phenomena emanate from the vehicle base.

Keywords: complex flows, flow separation, limiting streamlines, vortex formation, crossflow separation, vehicle aerodynamics

The important thing is not to stop questioning.
Curiosity has its own reason for existing.
Albert Einstein

Acknowledgements

Over the last five years, many people supported me in my studies and on my way taking this step. All of them made an important contribution to this thesis!

First of all I would like to thank Prof. Lennart Löfdahl, without whom I would not have taken the chance for this work. From the very beginning you were giving me the option and support needed to start up first a Diploma thesis, which opened up the idea and the chance to follow up with this PhD project in your research group.

Prof. Lars Larsson I would like to thank for his input and support. I appreciated the many hours we spent on enlightening discussions and I would like to thank you for your patience, availability and all the knowledge you shared with me.

I am also glad for the chance of having Alexander Broniewicz as an industrial supervisor. Thanks for all the help, especially in the wind tunnel, and the trust to make ideas and chances possible. Your view on the project gave this work an additional perspective.

I would also like to thank Prof. Simone Sebben for her supervision. It was great that you joined the supervision group. Thanks for all the feedback and support.

Teddy Hobeika, Emil Ljungskog, Randi Franzke and Magnus Urquhart I would like to thank for the many hours of discussion, your input and feedback, as well as technical and mental support.

All the members of the Steering Committee I would like to thank for their valuable input and advice: Lennart Löfdahl, Lars Larsson, Alexander Broniewicz, Anders Tenstam, Per Elofsson, Kamran Noghabai.

This project would not have been possible without the funding provided by the Swedish Energy Agency, within the framework Strategic Vehicle Research and Innovation, Volvo Cars, Volvo Trucks and Scania.

Nomenclature

β	local flow direction close to the surface	[-]
δ_{ij}	Kronecker Delta	[-]
μ	dynamic viscosity	$[\frac{\mathrm{N\,s}}{\mathrm{m^2}}]$
ϱ	density	$[\frac{\mathrm{kg}}{\mathrm{m^3}}]$
ν	kinematic viscosity	$[\frac{\mathrm{m^2}}{\mathrm{s}}]$
τ_{ij}	shear stress tensor	$[\frac{\mathrm{N}}{\mathrm{m^2}}]$
τ_{W}	wall shear stress	$[\frac{\mathrm{N}}{\mathrm{m^2}}]$
$\vec{\omega}$	vorticity vector	$[\frac{1}{\mathrm{s}}]$
ω_i	vorticity vector component	$[\frac{1}{\mathrm{s}}]$
$\vec{\omega_{\mathrm{W}}}$	wall vorticity	$[\frac{1}{\mathrm{s}}]$
Ω_{ij}	vorticity tensor or rotation tensor	$[\frac{1}{\mathrm{s}}]$
ε_{ijk}	Levi-Civita tensor	[-]
Γ	Circulation	$[\frac{\mathrm{m^2}}{\mathrm{s}}]$
σ_{ij}	Cauchy stress tensor	$[\frac{\mathrm{N}}{\mathrm{m^2}}]$
ϕi	Vorticity flux	$[\frac{1}{\mathrm{sm}}]$
A	frontal area of the vehicle	$[\mathrm{m^2}]$
a	acceleration	$[\frac{\mathrm{m}}{\mathrm{s^2}}]$
b	distance between adjacent limiting streamlines	[m]
c_{D}	drag coefficient	[-]
c_{L}	lift coefficient	[-]
c_{Lf}	lift coefficient front	[-]
c_{Lr}	lift coefficient rear	[-]
c_{p}	pressure coefficient	[-]
F	force	[N]
F_{p}	pressure force	[N]
F_{v}	viscous force	[N]
g	gravitational constant	$[\frac{\mathrm{m}}{\mathrm{s^2}}]$
h	distance of a limiting streamline from the surface	[m]
L	length of the vehicle	[m]

l_{wb}	wheelbase length	[m]
$\dot{m}$	mass flow	$[\frac{\mathrm{kg}}{\mathrm{s}}]$
m	mass	[kg]
N	node point	[-]
N′	half node	[-]
p_∞	static pressure of the incident flow	$[\frac{\mathrm{N}}{\mathrm{m}^2}]$
p	local static pressure	[Pa]
q	dynamic pressure of the incident flow	$[\frac{\mathrm{N}}{\mathrm{m}^2}]$
R	curvature radius	[m]
Q	Q criterion	$[\frac{1}{\mathrm{s}}]$
S	saddle point	[-]
S′	half saddle	[-]
S_{ij}	strain rate tensor	$[\frac{1}{\mathrm{s}}]$
t	time	[s]
U	velocity magnitude	$[\frac{\mathrm{m}}{\mathrm{s}}]$
U_∞	free stream velocity	$[\frac{\mathrm{m}}{\mathrm{s}}]$
$\underline{u}$, u_i	velocity vector	$[\frac{\mathrm{m}}{\mathrm{s}}]$
u, v, w	velocity vector components	$[\frac{\mathrm{m}}{\mathrm{s}}]$
$\dot{V}$	volumetric flow	$[\frac{\mathrm{m}^3}{\mathrm{s}}]$

Abbreviations

PVT	Aerodynamic Wind Tunnel of Volvo Car Corporation
VCC	Volvo Car Corporation
WDU	Wheel Drive Unit
BLC	Boundary Layer Control
CFD	Computational Fluid Dynamics
MRF	Multiple Refrence Frame
RANS	Reynolds Averaged Navier Stokes
RST	Reynolds Stress Transport turbulence model
CFS	cross flow separation

Definitions

1 drag count $\Delta c_{\mathrm{D}} = 0,001$

List of Publications

This thesis is a monograph based on the work reported in the following publications:

Journal Articles

Paper 1:

S. Bonitz, L. Larsson, L. Lofdahl, and A. Broniewicz. "Structures of Flow Separation on a Passenger Car". In: SAE International Journal of Passenger Cars - Mechanical Systems *8.1 (2015).* ISSN*: 1946-4002.* DOI*: 10.4271/2015-01-1529*

Paper 2:

S. Bonitz, D. Wieser, A. Broniewicz, L. Larsson, L. Lofdahl, C. Nayeri, and C. Paschereit. "Experimental Investigation of the Near Wall Flow Downstream of a Passenger Car Wheel Arch". In: SAE International Journal of Passenger Cars - Mechanical Systems *11.1 (2018).* ISSN*: 1946-4002.* DOI*: 10.4271/06-11-01-0002*

Paper 3:

S. Bonitz, L. Larsson, L. Löfdahl, and S. Sebben. "Numerical Investigation of Crossflow Separation on the A-Pillar of a Passenger Car". In: ASME J. Fluids Eng. *140.11 (2018).* ISSN*: 00982202.* DOI*: 10.1115/1.4040107*

Paper 4:

S. Bonitz, L. Larsson, and S. Sebben. "Unsteady Pressure Analysis of the Near Wall Flow Downstream the Front Wheel of a Passenger Car under Yaw Conditions". In: International Journal of Heat and Fluid Flow *accepted for publication (2018)*

Peer Reviewed Conference Papers

Paper 5:

S. Bonitz, L. Löfdahl, L. Larsson, and A. Broniewicz. "Investigation of Three-Dimensional Flow Separation Patterns and Surface Pressure Gradients on a Notchback Vehicle". In: International Vehicle Aerodynamics Conference*. Ed. by IMechE. [S.l.]: Woodhead, 2014, pp. 55–65.* ISBN*: 9780081001998*

Paper 6:

D. Wieser, S. Bonitz, L. Lofdahl, A. Broniewicz, C. Nayeri, C. Paschereit, and L. Larsson. "Surface Flow Visualization on a Full-Scale Passenger Car with Quantitative Tuft Image Processing". In: SAE 2016 World Congress and Exhibition. *SAE Technical Paper Series. SAE International400 Commonwealth Drive, Warrendale, PA, United States, 2016.* DOI*: 10.4271/2016-01-1582*

Paper 7:

C. Kounenis, S. Bonitz, E. Ljungskog, D. Sims-Williams, L. Lofdahl, A. Broniewicz, L. Larsson, and S. Sebben. "Investigations of the Rear-End Flow Structures on a Sedan Car". In: SAE 2016 World Congress and Exhibition. *SAE Technical Paper Series. SAE International400 Commonwealth Drive, Warrendale, PA, United States, 2016.* DOI*: 10.4271/2016-01-1606*

Paper 8:

S. Bonitz, L. Löfdahl, L. Larsson, and A. Broniewicz. "Flow Structure Identification over a Notchback Vehicle". In: International Conference on Vehicle Aerodynamics. *Ed. by IMechE. Woodhead, 2016*

Conference Papers

Paper 9:

D. Wieser, S. Bonitz, C. Nayeri, Christian O. Paschereit, A. Broniewicz, L. Larsson, and L. Löfdahl. "Quantitative Tuft Flow Visualization on the Volvo S60 under realistic driving Conditions". In: 54th AIAA Aerospace Sciences Meeting. *AIAA SciTech. American Institute of Aeronautics and Astronautics, 2016.* DOI*: 10.2514/6.2016-1778.* URL*: http://dx.doi.org/10.2514/6.2016-1778*

Contents

Abstract i

Acknowledgements v

Nomenclature vii

Abbreviations ix

Definitions ix

List of Publications xi

1 Introduction 1

2 Limiting Streamlines and Singular Points 3
2.1 Calculation of limiting streamlines . . . 3
2.2 Singular points . . . 5
2.3 Forces acting on limiting streamlines . . . 6

3 Vorticity and Vortex Dynamics 9
3.1 Stress and deformation rate tensor . . . 9
3.2 Vorticity . . . 10
3.3 Vorticity production . . . 10
3.4 Circulation . . . 11
3.5 Vorticity transport equation . . . 12
3.6 Vortex identification . . . 14

4 Flow Separation 15
4.1 Two dimensional flow separation . . . 15
4.2 Classical necessary condition for flow separation . . . 16
4.3 Description and characterization of separation phenomena - a literature review . . . 18
4.3.1 Maskell 1955 . . . 18
4.3.2 Lighthill 1963 . . . 19
4.3.3 Tobak & Peake 1982 . . . 20
4.3.4 Chapman & Yates 1991 . . . 22

4.3.5 Wu et al. 2000 . . . 27
4.3.6 Surana et al. 2006 . . . 27
4.3.7 Summary of the classification concepts . . . 29

5 Experimental Method **31**
5.1 The Volvo full scale wind tunnel - PVT . . . 31
5.1.1 Technical specifications . . . 31
5.1.2 Moving ground system . . . 32
5.1.3 Boundary layer control (BLC) . . . 32
5.2 Test object . . . 33
5.3 Pressure measurements . . . 34
5.4 Paint visualizations . . . 35
5.5 Tuft visualizations . . . 35

6 Numerical Method **37**
6.1 Computational domain and geometry specification . . . 37
6.2 Mesh specifications . . . 38
6.3 Solver specifications . . . 40
6.4 Mesh investigation . . . 40

7 Identification of Separation **43**
7.1 Surface flow pattern around the antenna . . . 43
7.1.1 Review on junction flows . . . 44
7.1.2 Flow topology . . . 45
7.1.3 Surface properties . . . 48
7.2 Surface flow pattern over the rear window . . . 52
7.2.1 Review on the rear end flow topology of vehicle geometries . . . 52
7.2.2 Flow topology . . . 54
7.2.3 Surface properties . . . 57
7.2.4 Unsteady aspects of the near wall flow over the rear window . . . 60
7.3 Surface flow pattern along the A-pillar . . . 61
7.3.1 Review on generic A-pillar flows . . . 61
7.3.2 Flow topology . . . 62
7.3.3 Surface properties . . . 63
7.4 Surface flow downstream of the front wheelhouse . . . 65
7.4.1 Flow topology . . . 65
7.4.2 Surface properties . . . 66
7.4.3 Unsteady aspects of the near wall flow behind the front wheel arch 68
7.5 Surface flow on the vehicle base . . . 72
7.5.1 Review on wake flow structures behind passenger vehicles . . . 72
7.5.2 Flow topology . . . 73
7.5.3 Surface properties . . . 74

8 Development of Separation Structures into the Flow **77**
8.1 Antenna flow . . . 77
8.2 Rear window flow . . . 80

8.3 A-pillar flow . . . 86
8.4 Flow downstream of the front wheel arch . . . 90
8.5 Base wake flow . . . 90

9 Discussion **101**
9.1 Reynolds number effects . . . 101
9.2 Effects of geometry changes . . . 102
9.2.1 Smoothed rear window . . . 102
9.2.2 Flow development without the antenna geometry . . . 106
9.3 Simulation method . . . 108
9.4 On the identification and prediction of separation phenomena . . . 112
9.4.1 Discussion on different methods to identify and predict separation 112
9.4.2 Correlation between characteristic topological features and surface properties . . . 113

10 Conclusions **117**

References **121**

List of Figures

2.1 Flow directions close to the surface 4
2.2 Stramlines in different heights above the surface 5
2.3 Types of singular points: node, focus, saddle point 5
2.4 Acting forces on a fluid particle 6
2.5 Pressure force acting on a fluid element in a curved flow 7

3.1 Ideal vortex 12

4.1 Velocity profiles before, at and after a 2D separation 16
4.2 Types of separation according to Maskell [24] 19
4.3 Schematic of the creation of a streamsurface 20
4.4 Surface flow pattern of a horn-type separation [34] 21
4.5 Separatrixes 23
4.6 The appearance of node-saddle-node combinations depending on their scale 24
4.7 Saddle point of separation and its development into the flow [36] 24
4.8 Types of bifurcation 25
4.9 Classification of separation pattern according to [36] 26
4.10 Vorticity and shear stress lines across a separation line 28

5.1 Boundary layer control system [45] 33
5.2 S60 test object setup in the wind tunnel 34
5.3 Experimental setup of the tuft image acquisition at the side of the vehicle [2] 36

6.1 Numerical wind tunnel 37
6.2 Virtual vehicle model 38
6.3 Wall y^+ distribution on the vehicle body 39
6.4 Mesh refinement zones 39
6.5 x-vorticity distribution with limiting streamlines for three different mesh configurations 41

7.1 Area of investigation behind the antenna 43
7.2 Schematic flow around a cylinder mounted to the ground 44
7.3 Numerical and experimental limiting streamline pattern around the antenna - top view 45
7.4 Detailed limiting streamline pattern around the antenna - front and rear view 47

7.5 Limiting streamline pattern around the antenna; surface coloured by wall shear stress magnitude . . . 49
7.6 Limiting streamline pattern around the antenna; surface coloured by pressure coefficient . . . 50
7.7 Limiting streamline pattern around the antenna; surface coloured by x-vorticity . . . 51
7.8 Detailed limiting streamline pattern on the antenna rear end; surface coloured by z-vorticity . . . 51
7.9 Limiting streamline pattern over the rear window . . . 55
7.10 Limiting streamline pattern over the rear window, calculated using the tuft visualisation method . . . 56
7.11 Limiting streamline pattern over the rear window; surface coloured by wall shear stress magnitude . . . 57
7.12 Limiting streamline pattern over the rear window; surface coloured by pressure coefficient . . . 58
7.13 Surface pressure distribution over the rear window; experimental result . . 58
7.14 Limiting streamline pattern over the rear window; surface coloured by x-vorticity . . . 59
7.15 Standard deviation of the tuft orientation . . . 60
7.16 Limiting streamline pattern along the A-pillar . . . 62
7.17 Limiting streamline pattern along the A-pillar; surface coloured by wall shear stress magnitude . . . 63
7.18 Limiting streamline pattern along the A-pillar; surface coloured by pressure coefficient . . . 64
7.19 Limiting streamline pattern along the A-pillar; surface coloured by x-vorticity 64
7.20 Limiting streamline pattern downstream of the front left wheel . . . 66
7.21 Experimental and numerical limiting streamline pattern downstream of the front wheelhouse; surface coloured by surface pressure . . . 67
7.22 Distribution of the standard deviation of the tuft angle . . . 68
7.23 Pressure sensor distribution and identification downstream of the front wheel 69
7.24 Distribution of the standard deviation of the pressure coefficient . . . 70
7.25 Cross correlation matrix respective sensor S2 and sensor S15 . . . 71
7.26 Cross correlation between sensor S6/S10, S6/S11 and S6/S12 . . . 71
7.27 2D streamlines in the symmetry plane through the wake . . . 72
7.28 Limiting streamline pattern on the vehicle base . . . 73
7.29 Limiting streamline pattern on the vehicle base; surface coloured by wall shear stress magnitude . . . 74
7.30 Limiting streamline pattern on the edges between trunk and vehicle base as well as side and vehicle base; surface coloured by wall shear stress magnitude 75
7.31 Limiting streamline pattern on the vehicle base; surface coloured by pressure coefficient . . . 76

8.1 Crossplane 100 mm behind the antenna base; coloured by x-vorticity . . . 77
8.2 Crossplanes downstream of the antenna base; coloured by x-vorticity . . . 79
8.3 Schematic, explaining the development of induced vorticity . . . 80

8.4 Isosurface Q = 500000; coloured by vorticity magnitude 81
8.5 Isosurface Q = 1000; coloured by vorticity magnitude 82
8.6 Crossplanes over the rear window - part 1; coloured by x-vorticity 83
8.7 Crossplanes over the rear window - part 2; coloured by x-vorticity 84
8.8 Crossplanes over the rear window; coloured by Q criterion 85
8.9 Defined coordinate system and locations of crossplanes used in the discussion 86
8.10 Perspective view on four different crossplanes (A, B, C and H) along and downstream the A-pillar; coloured by x-vorticity and showing 2D streamlines in the crossplanes 87
8.11 A-pillar vortex visualized by the Q criterion Isosurface Q=0 and colored by the x-vorticity 88
8.12 Perspective view on four different crossplanes (D, E, F and G); coloured by vorticity magnitude and showing 2D streamlines in the crossplanes . . 89
8.13 Crossplane with 2D streamlines at the rear end ($x/L = 0$) and $x/L = 0.8$ downstream of the vehicle base; coloured by x-vorticity 91
8.14 Crossplanes upstream of the vehicle base - part 1; coloured by x-vorticity 92
8.15 Crossplanes upstream and downstream of the vehicle base - part 2; coloured by x-vorticity 93
8.16 Crossplanes upstream of the vehicle base coloured by Q criterion, $Q > 0$ - part 1 94
8.17 Crossplanes downstream of the vehicle base coloured by Q criterion, $Q > 0$ - part 2 96
8.18 Crossplanes downstream of the vehicle base coloured by Q criterion, $Q > 0$ - part 3 97
8.19 Crossplane $x/L = 1.40$; coloured by Q criterion, $Q > 0$ 98
8.20 Crossplanes downstream of the vehicle base; coloured by vorticity magnitude 99

9.1 Wall y^+ distribution for 100 km/h and 140 km/h 102
9.2 Limiting streamline pattern for the two rear window geometries 103
9.3 Comparision of the flow field in Plane B 104
9.4 Comparison of the flow field in Plane D; coloured by x-vorticity 105
9.5 Comparision of the flow field in plane F (1100 mm downstream of plane A); coloured by Q-criterion 106
9.6 Wall shear stress pattern over the rear window, without an antenna; surface coloured by x-vorticity 107
9.7 Crossplane over the rear window without an antenna; coloured by x-vorticity 108
9.8 Crossplane over the trunk without antenna; coloured by Q-criterion . . . 108
9.9 Limiting streamline pattern over the rear window for a steady and unsteady solution 109
9.10 Limiting streamline pattern downstream of the front wheel; comparision between an unsteady CFD solution and experimental results 111
9.11 Change in x-vorticity across a bifurcation line 115

List of Tables

5.1 Repeatability uncertainties 32
5.2 Vehicle specifications 34

Chapter 1

Introduction

The phenomenon of separated flows has been the focus of several researchers over centuries. One of the first descriptions of the detachment of flow can be found in a work by Hermann von Helmholtz from 1868 [10], however, researchers are still working on a detailed description of separating and separated flow. In regions of separated flow the velocity, pressure and also the temperature can change drastically and this leads to changes of the flow field. In addition, separated regions are characterized by an unsteady flow field with possibly occurring coherent periodic structures which are convected into the wake [11].

As a viscous flow problem, the separation of flow is not only important for science, but also for practical applications. A typical example is the flow around wing profiles, which create separated regions depending on their angle off attack or the creation of the familiar tip vortices. Other areas which are concerned about separating flows are for instance the turbine industry [12–14], the building sector [15, 16], ship design [17], biofluid flows [18, 19], the area of sport aerodynamics [20, 21] or the field of vehicle aerodynamics [16, 22, 23].

The separation of flow is connected to the creation of vortices and wake regions, which usually results in energy losses and forces acting on the objects. One of the focus areas in the research of flow separation is its impact on drag and the possibilities of reducing it. Other, not less important attributes affected by separated flow are the creation of noise and the contamination by dirt and water of specific parts and areas.

To be able to improve the applications regarding their aerodynamic performance and their related attributes, it is of importance to understand the flow physics. It is desired to be able to predict the creation of flow structures and their development as well as their impact onto the overall performance. Hence, it is important to understand the mechanisms of the fluid-body interaction, the near wall flow behaviour and the development of flow structures into the bulk flow. Additionally, its unsteady nature leads to further phenomena, for instance vortex shedding, which need to be analysed and understood.

Considering the field of road vehicles, all the described aspects play an important role throughout the design and development process. The aerodynamic performance determines important parameters as handling and stability, as well as the aerodynamic drag, which directly affects the energy consumption. The creation of noise is especially uncomfortable for the passengers and in the first place the driver, as it expedites mental fatigue and lack of concentration. Last the flow field determines the vehicle contamination which is undesired from a customer point of view as well as for safety aspects (contamination of sensors, reduced visibility of the driver,...).

In this work the development of separation phenomena on a Volvo S60 passenger car will be described and discussed. Around the car five areas are chosen where different types and situations of separation occur. The flow around a geometry connected to a wall is represented by the antenna, which shows characteristic flow features that are also observed in other junction flows. On the rear window, various singular points can be identified, whereby created focus pairs attract attention. A fairly isolated observation of a so-called crossflow separation can be found along the A-pillar. Further the near wall flow downstream of the front wheel is studied, which discusses an area characterized by a high level of flow structure interaction. Last, the wake flow behind the vehicle is investigated.

Based on the flow topology the development of flow structures is discussed. The footprint created by the limiting streamlines is connected to surface quantities, for instance the surface pressure or the wall shear stress. The near wall flow behaviour and the transport of occurring phenomena into the bulk flow are studied by a detailed flow field analysis. The main analysis is based on a numerical steady state approach (Reynolds Averaged Navier Stokes (RANS) with a $k-\omega\,SST$ turbulence model). These numerical results are compared to experimental data obtained from paint visualisations, tuft visualisations and pressure measurements. For selected areas, unsteady (experimental) results are available, which are discussed in the respective sections. Besides an analysis and discussion on the creation of the observed phenomena for this particular S60 model, the description of the results and their interpretation are generalized.

Chapters 2 and 3 will give theoretical background on the concepts of limiting streamlines as well as vorticity dynamics. These are followed by a literature review on flow separation. The experimental and numerical methods are described in Chapter 5 and 6, followed by the anaylsis and discussion of the flow around a passenger car.

The flow study is divided into two parts. Chapter 7 describes the limiting streamline pattern and surface properties on different areas on the car. In the analysis of the surface flow topology the identification of singular points and general separation patterns is in the focus. The identified characteristics are further correlated with surface properties. In Chapter 8 it is studied, how the near wall flow develops into the bulk flow and how the resulting separation structures evolve.

In Chapter 9 different aspects possibly influencing the limiting streamline pattern are discussed. Further, the findings from the previous chapters are combined in order to provide a picture of the mechanisms leading to a separation of flow. The thesis closes with a summary of all findings in the conclusion chapter (Chapter 10).

Chapter 2

Limiting Streamlines and Singular Points

To understand the flow around three dimensional geometries, a language is required, which describes and characterizes this flow. The velocity field can be visualized and studied by means of streamlines. Streamlines are by definition lines where at each point the velocity vector $\underline{u} = (u, v, w)$ corresponds to the actual flow direction; in other words at each point of a streamline the velocity vector is tangential to it. Further, they are not allowed to cross each other at any regular point, nor can they start or end in the interior of the fluid. Hence, they either have to start and end on a body surface or form a closed curve in the fluid. Discontinuities are represented by singular points. To describe the flow topology on the surface of a body, the concept of limiting streamlines can be used as a describing language.

2.1 Calculation of limiting streamlines

At the surface, the velocity relative to the body is zero due to the no-slip condition, therefore streamlines cannot be drawn on the surface. However, it can be shown that the flow direction on the surface corresponds to the direction of the wall shear stress. The lines on the surface which are determined by the direction of the shear stress correspond then to the limit of the streamlines approaching the wall. These lines are therefore called limiting streamlines [17].

The following derivation shows that the limit of the flow direction, when the distance to the surface tends to zero, corresponds to the direction of the shear stress. Figure 2.1 shows the velocity vector $\underline{u}$ close to the surface, where it only has components in the x and z direction. The origin of the shown coordinate system lies on the surface and the x

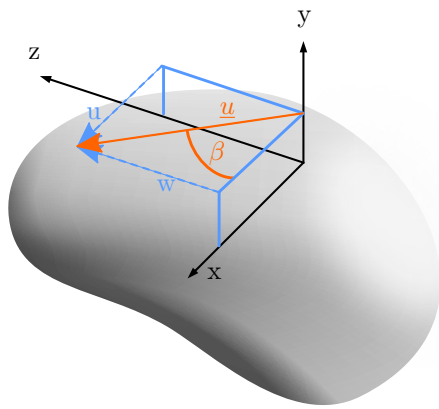

Figure 2.1: *Flow directions close to the surface*

coordinate points in the direction of the free stream flow. The angle between x and the local flow direction, β, can be calculated as follows

$$\begin{aligned} \tan\beta &= \frac{w}{u} \\ \beta &= \operatorname{atan}\left(\frac{w}{u}\right) \end{aligned} \tag{2.1}$$

Due to the no-slip condition the velocity is zero at the wall. Therefore $\lim_{y\to 0}\frac{w}{u}$ is indeterminate. However, according to l'Hospital's rule the quotient of the first derivative can be used to calculate the limit.

$$\lim_{x\to x_0}\frac{f'(x)}{g'(x)} = c \;\Rightarrow\; \lim_{x\to x_0}\frac{f(x)}{g(x)} = c \tag{2.2}$$

Applying this rule to calculate the flow direction leads to

$$\begin{aligned} \beta_{\mathrm{W}} &= \lim_{y\to 0}\operatorname{atan}\left(\frac{w}{u}\right) \\ &= \lim_{y\to 0}\operatorname{atan}\left(\frac{\frac{\partial w}{\partial y}}{\frac{\partial u}{\partial y}}\right) \end{aligned} \tag{2.3}$$

The partial derivative in numerator and denominator are exactly the components of the wall shear stress τ_{wz} and τ_{wx}, when y tends to zero.

$$\beta_{\mathrm{W}} = \operatorname{atan}\frac{\tau_{\mathrm{wz}}}{\tau_{\mathrm{wx}}} \tag{2.4}$$

Figure 2.2 compares the streamline pattern behind the antenna on a vehicle roof (Figure 2.2a) for limiting streamlines (Figure 2.2b) and streamlines 10 mm above the surface (Figure 2.2c). It can be seen that for Figure 2.2c the streamlines are aligned with the mean flow over the roof of the car. Moving closer to the surface the antenna influences the flow field, creating a characteristic flow pattern which is completely different.

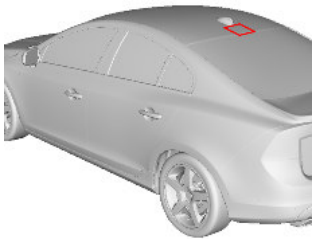

(a) *Location of the investigated flow behind the antenna*

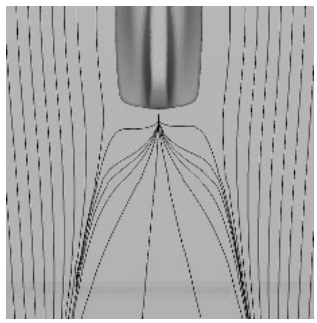

(b) *Limiting Streamlines*

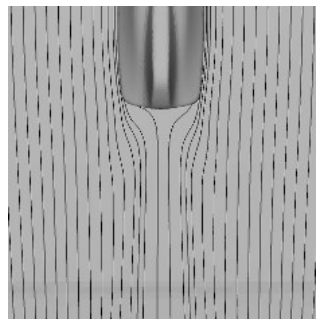

(c) *Streamlines* 10 mm *above the surface*

Figure 2.2: *Streamlines in different heights above the surface*

2.2 Singular points

Points where streamlines leave the surface are called points of separation. Points where streamlines attach to the surface are called points of attachment. Usually, points on a streamline are continuous and single valued. Except from points of attachment and points of separation. These are allowed to be many-valued and discontinuous. That means in such points streamlines can change their direction discontinuously and streamlines can meet without having a cusp [24]. These points are also called singular points or critical points. A, for aerodynamics familiar singular point, is the stagnation point of attachment at the nose of a wing profile.

These singular points are characteristic for the flow field and can be divided into two groups: i) saddle points and ii) nodal points, whereby nodal points can be subdivided into nodes and foci. An overview of occurring singular points is given in Figure 2.3.

The common lines, to which the limiting streamlines converge, are called negative bifurcation lines. If they diverge from a common limiting streamline it is called a positive bifurcation line. Separation lines are those lines were limiting streamlines converge (negative bifurcation line) and leave the surface. After leaving the solid body, the so-called separation surface is created. More detailed examples will be given in the following sections.

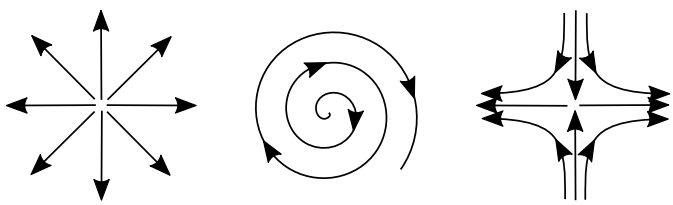

Figure 2.3: *Types of singular points: node, focus, saddle point*

2.3 Forces acting on limiting streamlines

Consider a flow which is free of any acting body forces, then the only acting forces result either from pressure or shear. A fluid particle which is located at the wall, resides within the viscous sublayer, as sketched in Figure 2.4. In the viscous sub-layer the velocity profile is linear, hence the wall shear stress

$$\tau_{\mathrm{W}} = \mu \frac{\partial u}{\partial y} \tag{2.5}$$

is constant throughout this layer. The resulting shear force acting on the considered fluid particle results from the difference between the shear acting on the top and the shear acting on the bottom of the particle (Figure 2.4). However, the derivative of the shear stress is zero as the shear stress is constant. Therefore the viscous force does not have an influence onto the particle in the viscous sublayer. Merely, the pressure force acts. However, the viscous force is determined at the upper edge of the viscous sublayer and changes therefore the shear forces within the sublayer in the flow direction. Hence, viscous forces and pressure force act onto a limiting streamline and can influence its flow path.

To understand the effect of pressure forces, a fluid element travelling along a streamline with curvature R is shown in Figure 2.5. Consider Newton's second law in the η direction

$$F_\eta = m\, a_\eta \tag{2.6}$$

The force F_η consists of pressure forces and viscous forces.

$$F_\eta = F_{\mathrm{p}} + F_{\mathrm{v}} \tag{2.7}$$

It was discussed before that locally only the pressure force has to be considered. This can be written as follows

$$F_{\mathrm{p}} = -\left(\left(p + \frac{\partial p}{\partial \eta}\, d\eta\right) d\xi\, d\zeta - p\, d\xi\, d\zeta\right) = -\frac{\partial p}{\partial \eta}\, d\eta\, d\xi\, d\zeta \tag{2.8}$$

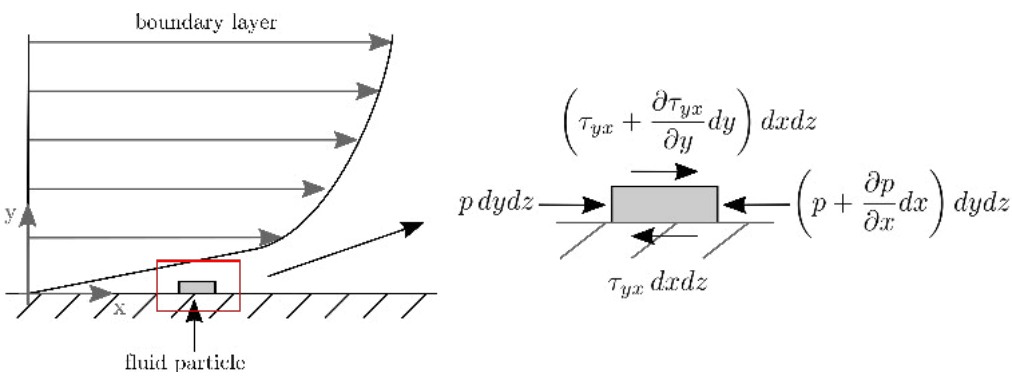

Figure 2.4: *Acting forces on a fluid particle*

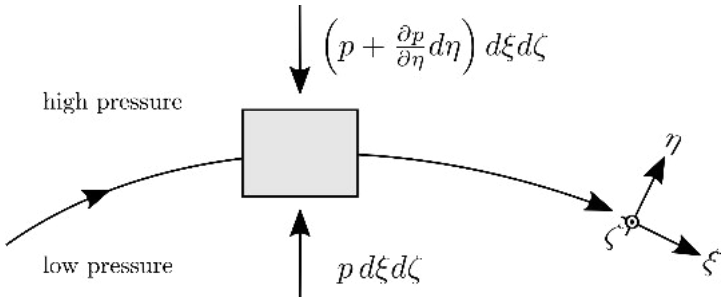

Figure 2.5: *Pressure force acting on a fluid element in a curved flow*

The mass for a fluid particle and the acceleration reads

$$m = \varrho\, d\eta\, d\xi\, d\zeta \tag{2.9}$$

$$a_\eta = -\frac{U_\xi^2}{R} \tag{2.10}$$

The expressions can be included in Equation 2.6 which leads to the following

$$F_\eta = F_\mathrm{p} + \underbrace{F_\mathrm{v}}_{=0} = m\, a_\eta \tag{2.11}$$

$$\underbrace{-\frac{\partial p}{\partial \eta}\, d\eta\, d\xi\, d\zeta}_{F_\mathrm{p}} = \underbrace{\varrho\, d\eta\, d\xi\, d\zeta}_{m} \left(\underbrace{-\frac{U_\xi^2}{R}}_{a_\eta} \right) \tag{2.12}$$

$$\frac{\partial p}{\partial \eta} = \varrho \frac{U_\xi^2}{R} \tag{2.13}$$

The radial pressure equation shows how the flow is influenced by an acting pressure gradient. ξ is the streamwise and η the transverse component. U_ξ is the velocity in streamwise direction and R the radius of curvature.

From a low to high pressure a gradient is acting ($\frac{\partial p}{\partial \eta}$), which causes a centripetal acceleration ($\frac{U_\xi^2}{R}$). A streamline under the influence of a transverse pressure gradient is curved. The low momentum flow close to the surface is very sensitive to the pressure gradient and changes its direction easily.

Chapter 3

Vorticity and Vortex Dynamics

In the following chapter a summary of the theoretical background on vorticity and vortex dynamics is given. Additionally relevant vortex identification methods are reviewed.

3.1 Stress and deformation rate tensor

The velocity gradient tensor $\frac{\partial u_i}{\partial x_j}$ can be split up into a symmetric and anti-symmetric part as given below. The tensor is given in index notation and Einstein's summation rule is used.

$$\begin{aligned}\frac{\partial u_i}{\partial x_j} &= \frac{1}{2}\left(\frac{\partial u_i}{\partial x_j} + \frac{\partial u_j}{\partial x_i}\right) + \frac{1}{2}\left(\frac{\partial u_i}{\partial x_j} - \frac{\partial u_j}{\partial x_i}\right) \\ &= S_{ij} + \Omega_{ij}\end{aligned} \tag{3.1}$$

S_{ij} is the symmetric part and called the strain-rate tensor
Ω_{ij} is the anti-symmetric part and called the vorticity tensor or rotation tensor

The constitutive law for Newtonian viscous fluids reads

$$\sigma_{ij} = -p\delta_{ij} + \tau_{ij} \tag{3.2}$$

whereby for incompressible isotropic Newtonian viscous fluids the shear stress τ_{ij} can be formulated as

$$\tau_{ij} = 2\mu S_{ij} - \frac{2}{3}\mu \underbrace{\frac{\partial u_k}{\partial x_k}}_{=0}\delta_{ij} = \mu\left(\frac{\partial u_i}{\partial x_j} + \frac{\partial u_j}{\partial x_i}\right) \tag{3.3}$$

Because of the continuity equation, the velocity gradient $\frac{\partial u_k}{\partial x_k}$ is zero for incompressible fluids. The shear stress tensor gradient can thus be written as

$$\frac{\partial \tau_{ij}}{\partial x_j} = \frac{\partial}{\partial x_j}\left(2\mu S_{ij}\right) = \mu \frac{\partial}{\partial x_j}\left(\frac{\partial u_i}{\partial x_j} + \frac{\partial u_j}{\partial x_i}\right) = \mu \frac{\partial^2 u_i}{\partial {x_j}^2} \tag{3.4}$$

3.2 Vorticity

Vorticity is defined as the curl of the velocity vector and can be written in index notation, using the Levi-Civita tensor ε_{ijk} as

$$\omega_i := \varepsilon_{ijk} \frac{\partial u_k}{\partial x_j} \tag{3.5}$$

The components of the vorticity vector are as follows:

$$\omega_x = \frac{\partial w}{\partial y} - \frac{\partial v}{\partial z}, \qquad \omega_y = \frac{\partial u}{\partial z} - \frac{\partial w}{\partial x}, \qquad \omega_z = \frac{\partial v}{\partial x} - \frac{\partial u}{\partial y} \tag{3.6}$$

The flow is often classified based on its rotation. It is called rotational flow if the vorticity is non zero ($\omega_i \neq 0$) and irrotational or potential flow if the the vorticity is zero ($\omega_i = 0$). It can be said that vorticity is connected to the rotation of a fluid particle.

3.3 Vorticity production

Looking at a fluid element, only shear stresses can rotate the fluid particle. As the pressure acts through the centre of the fluid particle it does not contribute to the rotational movement. It can be shown that the relation between vorticity and viscous terms can be described as

$$\frac{\partial \tau_{ij}}{\partial x_j} = \mu \frac{\partial^2 u_i}{\partial {x_j}^2} = -\mu \varepsilon_{inm} \frac{\partial \omega_m}{\partial x_n} \tag{3.7}$$

A detailed derivation can for instance be found in Panton [25]. This relation shows that

- without the viscous terms there is no vorticity and without vorticity there are no viscous terms
- vorticity is created by the viscous terms due to an imbalance in shear stresses

Vorticity is always generated at surfaces and it can be shown [25] that the relation between vorticity and wall shear stress can also be expressed as

$$F_{i,viscous} = n_j \tau_{ji} = -\mu \varepsilon_{ijk} n_j \omega_k \tag{3.8}$$

A detailed derivation for this relation is given in [25]. Equation 3.8 shows that the vorticity is directly proportional to the wall shear stress, with the viscosity as the proportionality

constant. In [25] it is further shown that a quantity *vorticity flux* can be defined, which indicates, how much vorticity is leaving the surface. The vorticity flux is defined as

$$\phi_i \equiv -n_j \frac{\partial \omega_i}{\partial x_j} \tag{3.9}$$

The vector ϕ_i gives the flux of i vorticity across a plane with normal n_j [25]. Consider a flat wall, with a coordinate system at a point P. The x-z plane is along the wall and y is normal to the wall. Hence, the vorticity flux introduced in Equation 3.9 gives the amount of i vorticity across the x-z plane with the normal in y direction ($n_j = (0, 1, 0)$).

A way to write the momentum equation, used by Panton [25], is

$$\frac{\partial u_i}{\partial t} + \frac{\partial\left(\frac{1}{2}U^2 + \frac{p}{\varrho}\right)}{\partial x_i} = -\varepsilon_{ijk}\omega_j u_k - \nu\varepsilon_{ijk}\frac{\partial \omega_k}{\partial x_j} \tag{3.10}$$

At the wall the velocity components are zero ($u_i = 0$) and Equation 3.10 yields to

$$\frac{\partial p}{\partial x_i} = -\mu\varepsilon_{ijk}\frac{\partial \omega_k}{\partial x_j} \tag{3.11}$$

With x-z the plane along the wall, and y in normal direction to the wall, gives the following relationships for the pressure gradient components along the wall

$$\frac{\partial p}{\partial x} = -\mu\frac{\partial \omega_z}{\partial y} = \mu\phi_z \tag{3.12}$$

$$\frac{\partial p}{\partial z} = \mu\frac{\partial \omega_x}{\partial y} = -\mu\phi_x \tag{3.13}$$

From this, it is shown that a pressure gradient along the surface is necessary to sustain a vorticity flux from the wall into the fluid. The third vorticity flux component into the fluid can be calculated evaluating $\frac{\partial \omega_i}{\partial x_i} = 0$ at the wall.

$$\phi_y = -\frac{\partial \omega_y}{\partial y} = \frac{\partial \omega_x}{\partial x} + \frac{\partial \omega_z}{\partial z} \tag{3.14}$$

The flux ϕ_y is determined by the vorticity distribution ω_x and ω_z. This shows that altough ω_y itself is zero at the wall, a flux out out of the wall is possible.

3.4 Circulation

Closely related to vorticity is circulation, which is defined as

$$\Gamma = \oint v_m t_m dl \tag{3.15}$$

and can be rewritten using Stokes' theorem as

$$\Gamma = \oint u_m t_m dl = \int_S \varepsilon_{ijk} \frac{\partial u_k}{\partial x_j} n_i dS \tag{3.16}$$

Vorticity vs. vortex

Based on the ideal vortex line, it can be explained that the classical understanding of a vortex is different from vorticity. Consider a potential flow, where the fluid moves along circular paths. This is called an ideal vortex line and is visualized in Figure 3.1.

The sketch shows that the fluid particle moves along the vortex line, but its diagonal keeps its direction, meaning the particle does not rotate. The figure further shows that it is possible to deform the particle. This is due to off-diagonal elements (shear) in the strain-rate tensor, which are non zero.
Hence, a fluid particle in an ideal vortex can deform, but by definition it does not rotate. However, this is a special case and in general a vortex has vorticity. Thus a qualitative description of a vortex according to Wu [26] is given as follows: *"[...] A vortex is a connected fluid region with a high concentration of vorticity compared with its surrounding."* [26] The above introduced vorticity tensor and the vorticity vector components are related as

$$\Omega_{ij} = \frac{1}{2} \varepsilon_{ijk} \omega_k \tag{3.17}$$

$$\omega_i = \varepsilon_{ijk} \left(S_{kj} + \Omega_{kj} \right) \tag{3.18}$$

3.5 Vorticity transport equation

The vorticity transport equation can be derived from the Navier-Stokes equation, as shown in Panton [25],

$$\frac{\partial u_i}{\partial t} + u_j \frac{\partial u_i}{\partial x_j} = -\frac{1}{\varrho} \frac{\partial p}{\partial x_i} + \nu \frac{\partial^2 u_i}{\partial {x_j}^2} \tag{3.19}$$

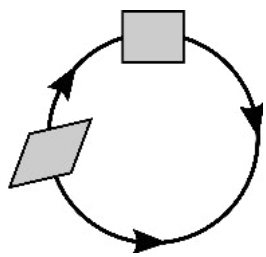

Figure 3.1: *Ideal vortex*

using the following substitution

$$u_j \frac{\partial u_i}{\partial x_j} = \frac{\partial\left(\frac{1}{2}u_j u_j\right)}{\partial x_i} + \varepsilon_{ijk}\omega_j u_k \tag{3.20}$$

which leads to

$$\frac{\partial u_i}{\partial t} + \frac{\partial\left(\frac{1}{2}u_j u_j\right)}{\partial x_i} + \varepsilon_{ijk}\omega_j u_k = -\frac{1}{\varrho}\frac{\partial p}{\partial x_i} + \nu\frac{\partial^2 u_i}{\partial {x_j}^2} \tag{3.21}$$

The formulation 3.21 is then differentiated with $\frac{\partial}{\partial x_q}$ and multiplied by ε_{pqi}, which leads to

$$\underbrace{\frac{\partial\left(\varepsilon_{pqi}\frac{\partial u_i}{\partial x_q}\right)}{\partial t}}_{\frac{\partial \omega_p}{\partial t}} + \underbrace{\varepsilon_{pqi}\frac{\partial\left(\frac{1}{2}u_j u_j\right)}{\partial x_q \partial x_i}}_{=0} + \varepsilon_{pqi}\frac{\partial(\varepsilon_{ijk}\omega_j u_k)}{\partial x_q} = - \frac{1}{\varrho}\underbrace{\varepsilon_{pqi}\frac{\partial p}{\partial x_q \partial x_i}}_{=0} + \nu\underbrace{\varepsilon_{pqi}\frac{\partial u_i}{\partial x_q \partial x_j \partial x_j}}_{\frac{\partial^2 \omega_p}{\partial {x_j}^2}} \tag{3.22}$$

The first term is the time derivative of the vorticity. The two terms identified as zero result from a multiplication of an asymmetric and symmetric tensor and the last terms contains again the vorticity. The third term on the left hand side can be rewritten as

$$\begin{aligned}\varepsilon_{pqi}\varepsilon_{ijk}\frac{\partial(\omega_j u_k)}{\partial x_q} &= \frac{\partial(\omega_p u_k)}{\partial x_k} - \frac{\partial \omega_j u_p}{\partial x_j} \\ &= u_k\frac{\partial \omega_p}{\partial x_k} + \omega_p\underbrace{\frac{\partial u_k}{\partial x_k}}_{=0} - u_p\underbrace{\frac{\partial \omega_j}{\partial x_j}}_{=0} - \omega_j\frac{\partial u_p}{\partial x_j} \\ &= u_k\frac{\partial \omega_p}{\partial x_k} - \omega_j\frac{\partial u_p}{\partial x_j}\end{aligned} \tag{3.23}$$

The vorticity equation then reduces to

$$\underbrace{\frac{\partial \omega_i}{\partial t}}_{\text{unsteady term}} + \underbrace{v_j\frac{\partial \omega_i}{\partial x_j}}_{\text{convective term}} = \underbrace{\omega_j\frac{\partial u_i}{\partial x_j}}_{\substack{\text{amplification,}\\ \text{rotation/tilting}}} + \underbrace{\nu\frac{\partial^2 \omega_i}{\partial {x_j}^2}}_{\text{diffusive term}} \tag{3.24}$$

The term $\omega_j\frac{\partial u_i}{\partial x_j}$ on the right hand side represents amplification and rotation/ tilting of the vorticity lines. The diagonal terms of this matrix give the vortex stretching, while the off diagonal terms represent vortex tilting. These two phenomena act in three dimensions and is the explanation that turbulence can only happen in three dimensional flows. Additionally, the convective and diffusive terms can be identified.

3.6 Vortex identification

It was mentioned that a vortex can be identified when a high vorticity concentration of arbitrary shape occurs. This can have a layer-like or an axial structure, whereby the layer-like structures are known as attached vortex layers (boundary layer) and free vortex layer (shear layer or mixing layer). Usually only the axial structures are called vortices, which can be subdivided into disk-like vortices (e.g. hurricane) or columnar vortices (e.g. tornado) [26].

There are different methods used to indicate and identify vortices in the flow. Their advantages and disadvantages are discussed widely in the literature, for instance in [27]. The most common ones, which are also used in this work, are briefly reviewed. The probably most widely used method, is the visualisation of vortices with 2D and 3D streamlines, to show their swirling motion. Especially in crossplanes it is convenient to show the 2D streamlines created by the velocity components in the respective planes. A vortex is then identified if a focus structure is observed. This method however does not give any quantitative indication of the amount of vorticity contained in the potential vortex.

Hence, it seems to be more descriptive to use the vorticity itself. Aside from the vorticity magnitude it is practical to use the specific vorticity component in direction of the vortex core. This allows to calculate the strength by means of circulation and gives the sense of rotation of the identified vortex structure. However it is difficult to determine an exact vortex boundary, as just the existence of vorticity does not describe a vortex.

Vorticity can be created by rotation and shear. Therefore, Hunt et al. [28] introduced the Q criterion in order to describe a vortex region more quantitatively. The Q criterion is defined as the second invariant of the velocity gradient tensor and results in a scalar value which can be calculated as follows

$$\begin{aligned} Q &= \frac{1}{2}\left(\frac{\partial^2 u_i}{\partial {x_i}^2} - \frac{\partial u_i}{\partial x_j}\frac{\partial u_j}{\partial x_i}\right) = -\frac{1}{2}\frac{\partial u_i}{\partial x_j}\frac{\partial u_j}{\partial x_i} \\ &= \frac{1}{2}\left(\|\mathbf{\Omega}\|^2 - \|\mathbf{S}\|^2\right) \end{aligned} \tag{3.25}$$

It is used to identify a vortex if $Q > 0$, which shows all areas in the flow, where rotation dominates over shear.

Chapter 4

Flow Separation

While the two-dimensional case is well understood and described, it is not yet clear which are the driving forces for flow separation in three dimensions. The velocity field around bluff bodies is a continuous vector field. To describe the pattern of the flow which can lead to a flow separation, a mathematical model is used, which describes the flow by means of streamlines and characteristic points. In experimental investigations, these can be visualized, for instance by using paint, which will be explained in a later chapter.

4.1 Two dimensional flow separation

In 1924 Ludwig Prandtl developed a concept to describe flow separation in steady, axisymmetric and 2-dimensional flows. He found that two criteria have to be fulfilled to be able to observe detachment from the surface [29].

- an adverse pressure gradient
- viscous effects in the fluid

If one of these criteria is not fulfilled, the flow will not separate from the surface. This happens for instance using a suction system, where the boundary layer and therefore the viscous influence is removed. Within the boundary layer viscous effects result in a change of velocity perpendicular to the surface; in other words a velocity gradient $\frac{\partial u}{\partial y}$ exists, similar to the first profile in Figure 4.1.

At the wall the no-slip condition is valid and therefore the velocity is zero. With an increasing distance from the wall the velocity increases until it reaches the inviscid flow velocity at the edge of the boundary layer. Within the boundary layer the flow is retarded and the velocity is lower close to the surface (first velocity profile in Figure 4.1). Further, close to the surface the momentum of the flow is small and it becomes much harder to

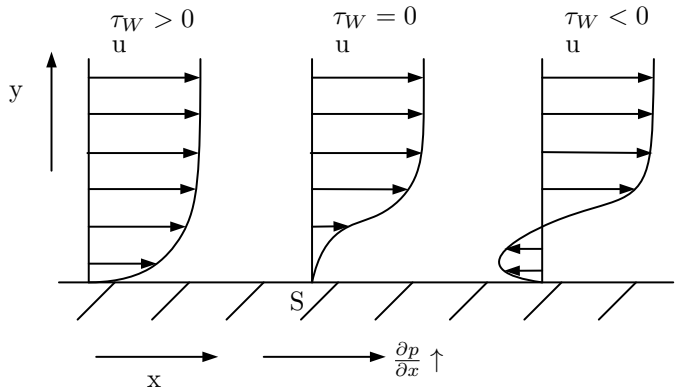

Figure 4.1: *Velocity profiles before, at and after a 2D separation*

overcome a large adverse pressure gradient. The flow is able to withstand a certain pressure gradient until it reaches the point where the low momentum fluid cannot overcome the acting pressure gradient and the particles are stopped (second profile in Figure 4.1). After the separation point a reverse flow occurs due to the still increasing adverse pressure(third profile in Figure 4.1). That means, in order to define the separation point S the velocity gradient in y direction has to be zero. Or in other words, the shear stress at the wall has to be zero as can be seen in Equation 4.1.

$$\tau_{\mathrm{W}} = \mu \frac{\partial u}{\partial y} = 0, \text{ because } \frac{\partial u}{\partial y} = 0 \text{ for } y = 0 \tag{4.1}$$

4.2 Classical necessary condition for flow separation

In a viscous fluid, tangential forces are transferred via molecular exchange of momentum and at the surface a boundary layer develops. An increasing adverse pressure gradient can cause a detachment of the boundary layer from the surface due to vorticity ejected into the flow. This can be explained as follows.

The vorticity equation in a Cartesian coordinate system is given in 3.5. For simplification, we assume a steady, incompressible 2D flow. The vorticity equation 3.5 can than be reduced to the following, where only the advection and diffusion terms are left.

$$u_j \frac{\partial \omega_i}{\partial x_j} = \nu \frac{\partial^2 \omega_i}{\partial {x_i}^2} \tag{4.2}$$

Let us assume a 2D flow in the x,y plane, where y is normal to the surface. The only non-zero component of the vorticity vector is the z component

$$\omega_z = \frac{\partial v}{\partial x} - \frac{\partial u}{\partial y} \tag{4.3}$$

and its derivative in y direction

$$\frac{\partial \omega_z}{\partial y} = \frac{\partial^2 v}{\partial x \partial y} - \frac{\partial^2 u}{\partial y^2} \tag{4.4}$$

At the wall all velocity components in x are zero which results in

$$\left(\frac{\partial u}{\partial x}\right)_{y=0} = \left(\frac{\partial v}{\partial x}\right)_{y=0} = 0 \tag{4.5}$$

The continuity equation gives

$$\frac{\partial u}{\partial x} + \frac{\partial v}{\partial y} = 0 \;\rightarrow\; \left(\frac{\partial v}{\partial y}\right)_{y=0} = 0 \;\rightarrow\; \left(\frac{\partial^2 v}{\partial x \partial y}\right)_{y=0} = 0 \tag{4.6}$$

This results in the following at the wall

$$\omega_z = -\frac{\partial u}{\partial y} \tag{4.7}$$

$$\frac{\partial \omega_z}{\partial y} = -\frac{\partial^2 u}{\partial y^2} \tag{4.8}$$

The Navier-Stokes equation in x direction is given in Equation 4.9

$$u\frac{\partial u}{\partial x} + v\frac{\partial u}{\partial y} = -\frac{1}{\varrho}\frac{\partial p}{\partial x} + \nu\frac{\partial^2 u}{\partial x^2} + \nu\frac{\partial^2 u}{\partial y^2} \tag{4.9}$$

Applying similar considerations at the wall ($y = 0$) as above, equation 4.9 can be reduced to

$$\frac{1}{\varrho}\frac{\partial p}{\partial x} = \nu\frac{\partial^2 u}{\partial y^2} \tag{4.10}$$

Using Equation 4.8, 4.10 can be rewritten as

$$\frac{1}{\varrho}\frac{\partial p}{\partial x} = -\frac{\partial \omega_z}{\partial y} \tag{4.11}$$

For the oncoming flow the vorticity has a negative sign (Equation 4.8). After the separation point the sign of $\left(\frac{\partial u}{\partial y}\right)_{y=0}$ changes. This means that also the sign for the vorticity has to change (positive vorticity, see equation 4.7). It is discussed in [30] that the presence of viscosity drives a diffusion process down the vorticity gradient (diffusion from a higher to lower vorticity). Therefore it can be said that the sign of the vorticity gradient at the wall determines the sign of the vorticity which is ejected into the flow at the wall. As explained in the previous paragraph, the vorticity after the separation point is positive, and enters a region with predominately negative vorticity, that means that the vorticity gradient $\frac{\partial \omega_z}{\partial y}$ is negative (directed to the wall), while the diffusion away from the surface is driven. The following statement can be made: introduction of positive vorticity into the

flow requires a negative vorticity gradient $-\frac{\partial \omega_z}{\partial y}$. From equation 4.11 it can be seen that this is the case in regions where the pressure gradient along the x direction is positive.

$$\frac{\partial p}{\partial x} > 0 \tag{4.12}$$

This is a well known necessary but not sufficient condition for separation. A more detailed explanation of this derivation can be found in [30].

4.3 Description and characterization of separation phenomena - a literature review

The description and characterization of the separation phenomena has concerned researchers for decades. Some look onto this problem from a phenomenological approach, others from a topological. Several terms were introduced to characterize the structures and effects. Often they describe similar observations, but with slight differences in the characterization. In the following sections, relevant publications are reviewed to give an overview over the research history and summarize key findings and definitions.

4.3.1 Maskell 1955

With the concept of surface streamlines or limiting streamlines new methods were developed to describe and explain the separation phenomena. Eichelbrenner and Oudart [31, 32] concluded, towards the development of a suitable concept, that the separation line must be an envelope of the surface streamlines. But this was still an imprecise description. Maskell [24] analyzed 3D separation based on surface streamlines and what happens in the neighborhood of such separation lines. He gave a clear definition of such surface streamlines and defined the so-called limiting streamlines. Further he stated that two different types of separation phenomena are existent:

i) the separation bubble
ii) the free vortex layer.

To be able to describe flow structures and the path of fluid particles, Maskell distinguished between 'open' and 'closed' paths. An open path begins infinitely upstream and ends infinitely downstream. Closed paths lie in the fluid and are named in his work also standing eddies which are isolated from the main flow. The separation surface separates the standing eddies from the outer flow, so that a closed region is built. Maskell called these closed regions bubbles, cf. [24].

Bubbles are well known concepts in two dimensions, as can be seen in Figure 4.2a. It shows the concept of a closed region, with a standing eddy as mentioned above. In this case one line of separation formed the bubble; resulting in one standing eddy. A three-dimensional separation bubble, formed by two separation lines as shown in Figure

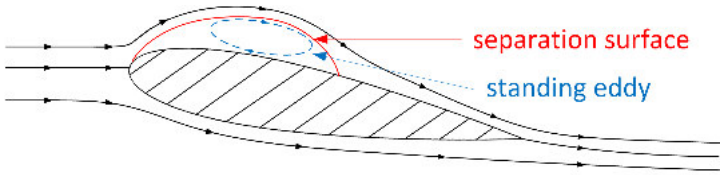

(a) *2D bubble separation with a standing eddy*

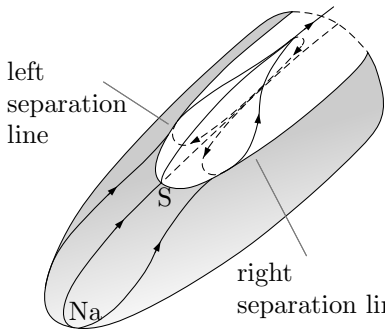

(b) *3D bubble separation with two counter rotating vortices*

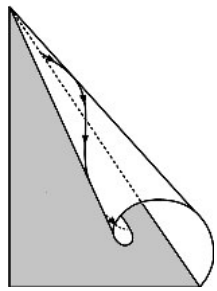

(c) *Free vortex sheet separation*

Figure 4.2: *Types of separation according to Maskell [24]*

4.2b results in the formation of two counter-rotating eddies. The surface of the bubble is again the separation surface. The observable standing eddies are forced by diffusion and the velocity of the flow within the bubble is usually much slower than the main flow. This difference in velocity is also often used to locate such a separation bubble.

The second type of separation described by Maskell is the free vortex layer. This occurs when a separation surface is formed and rolled up spirally. The characteristic feature for this structure is that it is created by main flow fluid and consists of a sheet of open separation streamlines which built a skeleton, cf. [24]. Such free vortex layers can be observed for instance at the leading edge of delta wings (Figure 4.2c), but also as a result of converging streamlines on a body surface.

According to Maskell, one can investigate the qualitative nature of separating flow just by studying the surface flow pattern. However, Maskell further pointed out, that the two described separation patterns usually appear together.

4.3.2 Lighthill 1963

It is still an open question which mechanisms cause the flow to separate. In 1963 Lighthill [33] explains the importance of vorticity and how it can be used to investigate flow separation. As separation is described as the phenomenon, where streamlines have a strong upwelling and leave the surface, it is of interest to understand, under which

conditions that can happen. Therefore a rectangular streamtube is considered. The width b is considered as the distance between two neighbouring streamlines. The height is given by the distance h. It follows:

$$\frac{1}{2}\omega_W h^2 b = \dot{V} \tag{4.13}$$

Streamlines can therefore only increase the distance z to the surface by

- a decrease of ω_W
  This mechanism occurs always together with a saddle point. An example is the 3D separation bubble in Figure 4.2b.
- a decrease of b (convergence of limiting streamlines)

These are according to Lighthill alternative mechanisms of separation which have to be kept in mind.

4.3.3 Tobak & Peake 1982

Tobak&Peake [34] explained Lighthill's criterion by expressing it in terms of shear stress. Looking at the rectangular stream-tube, built by the distance b between two limiting streamlines and the height h which is the distance to the wall (as shown in Figure 4.3), the following two statements can be made:

i) the mass flow through the stream-tube is constant, whereby $\bar{u}$ = mean velocity

$$\dot{m} = \varrho h b \bar{u} \tag{4.14}$$

ii) Since the velocity profile is linear close to the surface, the resulting shear stress can be written as follows

$$\tau_W = \mu \frac{\bar{u}}{h/2} \tag{4.15}$$

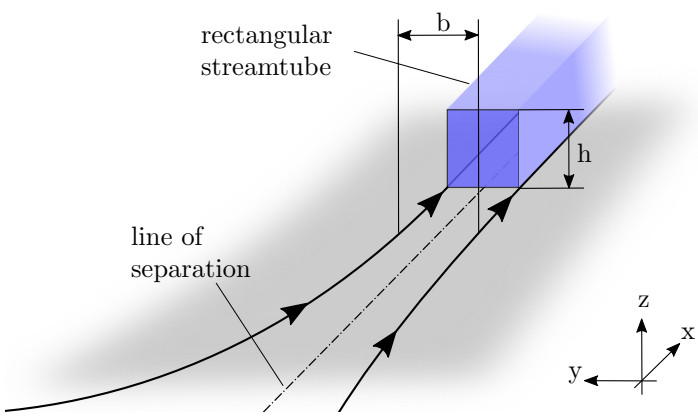

Figure 4.3: *Schematic of the creation of a streamsurface*

As soon as the line of separation is reached, h increases rapidly and the streamlines are leaving the surface. This can be explained by two mechanisms.

i) if the distance b decreases, as the streamlines converge, the height h has to increase to fulfil the continuity equation 4.14. That means that, an observed convergence of limiting streamlines has to lead to a separation line, which is the origin of a dividing surface. The fluid in this line leaves the surface as an up-rolling vortex sheet, similar to the free vortex layer described by Maskell.
ii) the resultant shear stress drops rapidly to a minimum (τ_W has not necessarily to become zero), therefore h has to increase. τ_W becomes zero in the case it approaches a saddle point.

A remaining case, described in this work is the occurrence of a focus. It appears invariably together with a saddle point. The resulting flow structure is named a "horn-type separation", which was observed in experiments done by Werlé in 1962 [35]. It is characterized by a focus on the surface where fluid leaves the surface like a tornado. Further a saddle point has to be present to connect the streamlines according to a continuous vector field. The surface flow pattern for this case is shown in the following Figure 4.4.

The study of singular points by themselves would not have a meaningful contribution in the description of the flow field. The connection between the singular points describes a relationship. Fortunately, topological rules exist, which describe this. The three most important rules for the amount of occurring singular points shall be cited in the following.

i) Counting nodes and saddles on the surface of a three-dimensional body, one has to find two more nodes (N) than saddles (S).

$$\Sigma N - \Sigma S = 2 \tag{4.16}$$

ii) is a 3D body considered, which is connected to a wall, the same amount of saddles and nodes can be found.

$$\Sigma N - \Sigma S = 0 \tag{4.17}$$

iii) A third rule which is interesting to study, considers a cross plane or a cut through a 3D geometry.

$$\Sigma N + \frac{1}{2}\Sigma N' - \Sigma S - \frac{1}{2}\Sigma S' = -1 \tag{4.18}$$

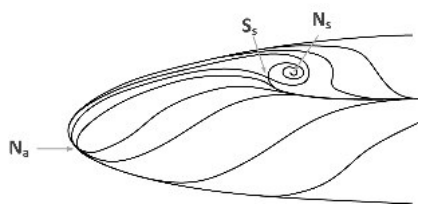

Figure 4.4: *Surface flow pattern of a horn-type separation [34]*

The here used half nodes (N') and half saddles (S') describe a node or saddle which occurs on a boundary while looking onto the cross plane. As this rule does not take into account the velocity component out of the plane, the rule has to be used carefully.

Although rules and ways of describing the flow pattern are available, it is still unanswered how three dimensional flow patterns originate and how they are created. An investigation of stability aspects can lead to further insights.

Structural Stability. As structural stable, a pattern on the surface is understood which has the same topological structure before and after an infinitesimal change (e.g. change of angle of attack, Reynolds number,...).
Structural stability of the external flow. A small change in one parameter does not change the topological structures, meaning that it does not change the number and types of singular points in the external three-dimensional velocity field.
Asymptotic stability of the external flow. With time going towards infinity, small perturbations are damped out to zero.
Structural and asymptotic instability. Here it will also be distinguished between local and global instabilities. A permanent change of the topological structure is called global instability (valid for the surface pattern and the external flow). On the other hand an instability is called local if it does not change the topological structure of the vector field (on the surface and the external). Therefore a structural instability is necessarily a global one, while asymptotic instability can be one or the other (cf. [34]). It is important to note that "asymptotic instability of the external flow leads to the notation of bifurcation, symmetry breaking and dissipative structures " [34].

The introduction of the local and global terminology also explains the distinction between *global* and *local separation* phenomena on the surface pattern. If a change in parameters does not change the surface pattern, a convergence of limiting streamlines can only be a local phenomenon resulting in a local line of separation (it appears without a creation or change of singular points). But if a surface pattern is changed in the sense of a change in singular points, a global phenomenon is observed. Therefore separation lines starting at (new) singular points are called global lines of separation.

4.3.4 Chapman & Yates 1991

Chapman and Yates [36] explain that the description of a three-dimensional flow, within a topological framework, requires the description of the following four points:

1. description of the occurring singular points
2. global properties which these singular points must obey in various planes
3. the extension of singular points into the third dimension
4. the use of bifurcation theory to provide basis on which changes in the topological structure can be considered

Looking onto the surface flow pattern local properties have also to be considered.

i) *Local summation rule for singular points*
Consider a region on the surface within a closed boundary. After a change of one parameter, the pattern might change, but the vectors crossing the boundary do not change, then the topological rule according to equation 4.17 has to be fulfilled.

ii) *Separatrix from one saddle cannot connect with another saddle*
Separatrixes are the lines which intersect in the saddle point (Figure 4.5).
Saddle to saddle combinations are highly unstable and are usually not possible.

iii) *Singular lines may occur on 3D bodies*
When a singular line occurs, the singular line has zero contribution to the summation rule. Under a small perturbation this singular line would split up and an even number of singular points would be created so that the summation rule is fulfilled again. An example is a body of revolution with angle of attack zero. In this case separation and reattachment result in a singular line and not in isolated singular points.

iv) *The issue of scale*
In some cases singular points are so close to each other that it is hard to separate them. As a result they often appear as one singular point. An example is the following node-saddle-node combination (Figure 4.6a).
In a global point of view they appear as a node. In Figure 4.6b it is shown how the appearance of the three singular points can change when they are moving closer together. According to Chapman&Yates it is useful in many cases to look at the large-scale point of view. Usually this can be done without causing any problems in the study of the flow pattern.

Regarding 3: Just the study of the singular points on the surface cannot give a sufficient understanding of the separation phenomena and how the singular points contribute to it. Therefore it has to be considered what happens above the surface. It can be shown that only four different types of 3D singular points are possible. Two types are possible if the surface pattern shows a node point. There is only one trajectory passing this point. It can either be a node of attachment, if the vector points towards the singular point, or it can be a point of separation, if it points away from the surface. If a saddle point occurs, then two further types of singular points are possible. There is only one plane leaving the

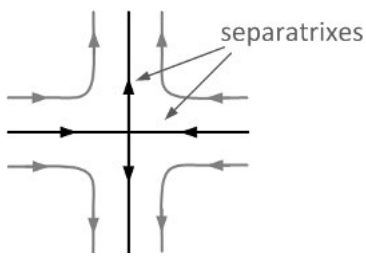

Figure 4.5: *Separatrixes*

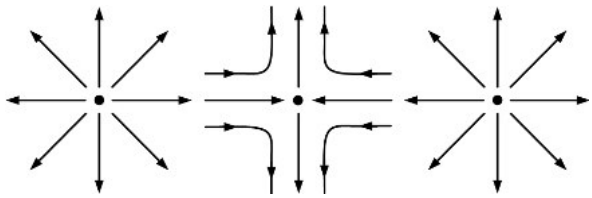

(a) *Node-saddle-node combination*

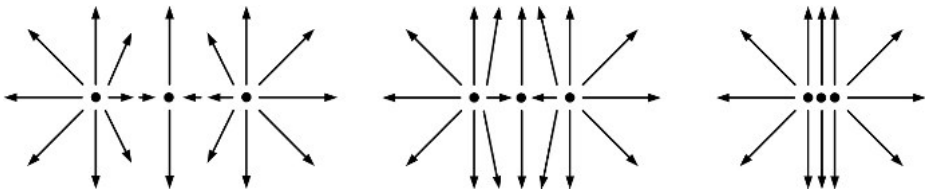

(b) *Large scale view for a node-saddle-node combination*

Figure 4.6: *The appearance of node-saddle-node combinations depending on their scale*

surface in which a node like flow can be observed (see Figure 4.7). Again it can either be a point of separation or attachment.

For the separating surface it can be said that this is the surface around which the vorticity that has been generated on the surface upstream of the saddle leaves the surface. This leads to the statement, made already by [34], that the existence of a saddle point of separation is a necessary condition for a global separation. But it is not sufficient. Regarding 4: As mentioned already by Tobak & Peake [34] the pattern after a perturbation is an important development to study. Changes in the pattern are especially interesting when singular points are added or differences in the topology appear. Such changes are called *structural bifurcation*. They can be divided into *transcritical and pitch fork bifurcation* (Figure 4.8) and can occur in three different ways:

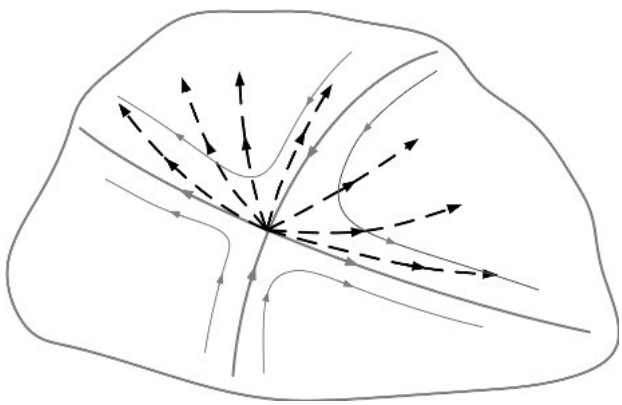

Figure 4.7: *Saddle point of separation and its development into the flow [36]*

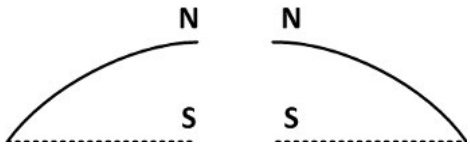

(a) *Transcritical and inverse transcritical*

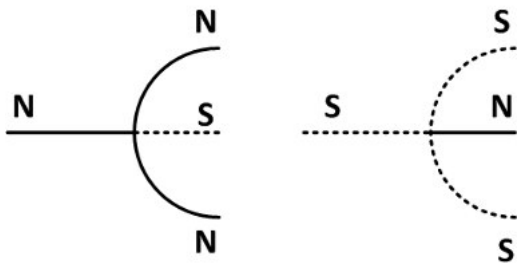

(b) *Pitch fork bifurcation*

Figure 4.8: *Types of bifurcation*

i) *new singular points appear, where none existed before*
In this case they have to occur in node-saddle combinations to fulfill the local summation rule. Either two points of attachment (or separation) or one of each are created. If the latter is the case, additionally an isolated singular point has to occur above the surface. This case belongs to a transcritical bifurcation which is illustrated in Figure 4.8a. On the left the development of a node-saddle pair is described, where no singular point existed before. An inverse transcritical bifurcation could also be possible, where, after a change of parameters, a node-saddle combination disappears.

ii) *a singular point splits into multiple singular points*
A bifurcation according to this description is called a pitchfork bifurcation and is shown in Figure 4.8b. Similar to the previous case the local summation rule has to be satisfied. That means a node has to change into a saddle and two nodes (left) and a saddle has to change into a node and two saddles (right).
All singular points can be of the same type (separation or attachment) as the original one or one of the new singular points is from the opposite types, while the others are of the type of the original one.

iii) *singular points on a singular line due to a symmetry breaking structural bifurcation*
After a small perturbation the singular line will most likely break up. In that case all combinations of saddles and nodes are possible as long they obey the summation rule and are distributed symmetrically along the singular line.

Classification of separation pattern

Chapman & Yates summarize in their work three basic types of separation, shown in Figure 4.9: Type I - bubble separation (Figure 4.9a), Type II - horn separation (Figure 4.9b) and crossflow separation (Figure 4.9c).

Type I separation - bubble separation. This type of separation starts at a saddle point. The separatrix divides the body in two regions. Fluid coming from the node point of attachment (stagnation point) cannot enter the region right of the saddle point. Further, this type has a singular point in the flow field, i.e. in the cross plane, close to the saddle-node pair. This is given due to the nature of the combination of the node of attachment combined with the saddle of separation.

Type II separation - horn type of separation. The so-called "horn-type" separation was first observed by Werle [35]. This type also emanates from a singular point - a focus.

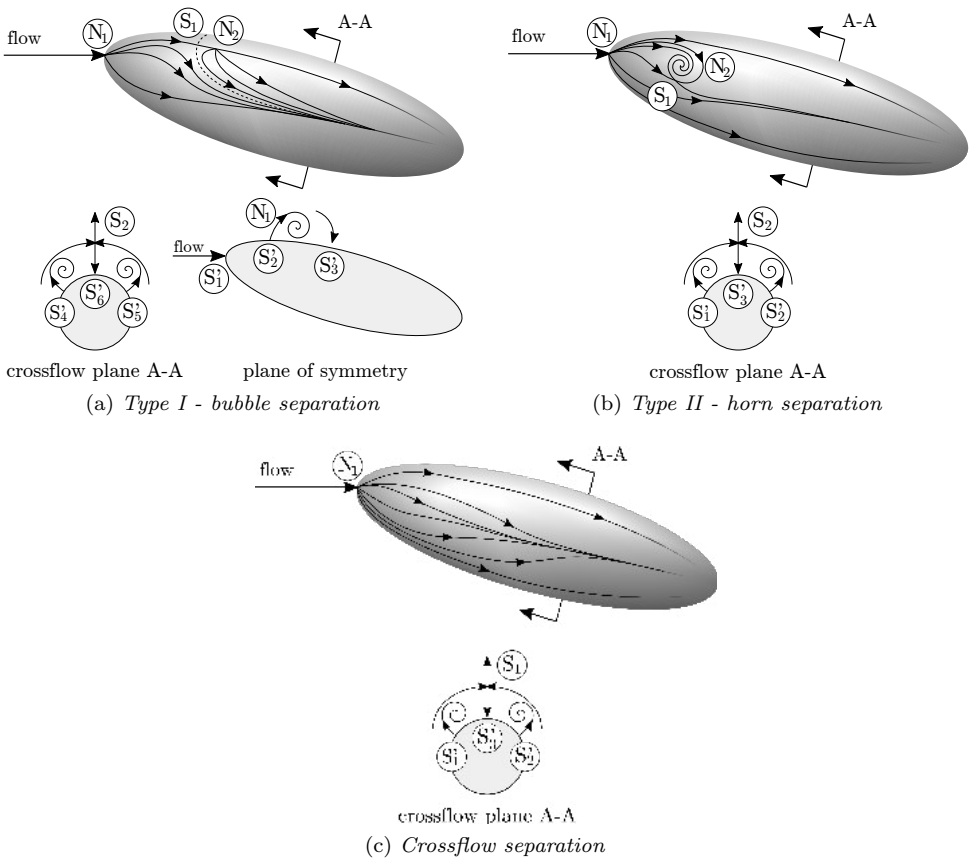

(a) *Type I - bubble separation*

(b) *Type II - horn separation*

(c) *Crossflow separation*

Figure 4.9: *Classification of separation pattern according to [36]*

Contrary to type I it has no singular point in the flow above the surface, as the saddle point of separation is combined with a node of separation. A further requirement is that this type has to result from a transcritical bifurcation.

Crossflow separation. Tobak & Peake called it local separation, others proposed open separation. All terms describe the same observation. The surface pattern shows a convergence of streamlines towards a separation line, where the flow leaves the surface as a vortex sheet, similar to Maskell's free vortex layer. It can be also said that vorticity leaves the surface where it is generated to form the vortex sheet. The main difference to the previous types is that there are no singular points which are locating the origin of this type of separation, hence it does not change the surface pattern in a topological sense, as there are no singular points added or vanished. In the work of Chapman & Yates the name crossflow separation was chosen as the topological characteristics, related to this type of separation, can only be observed in the cross plane (perpendicular to the undisturbed flow direction).

In their paper an example is shown, where converging streamlines do not lead to a crossflow separation. Hence, the following conclusion is given: "Although convergence of skin-friction lines onto a particular skin-friction line may be a necessary condition for separation, it is not a sufficient condition." [36] To the author of this thesis, this is an insufficiently investigated case as it is assumed that such an observation can only be made on a symmetry line.

4.3.5 Wu et al. 2000

Wu et al. [37] present a separation theory based on on-wall signatures of the flow and propose criteria for separation zones, separation lines and the initial location for an open separation zone and line. In their analysis the on-wall curvature of the vorticity lines plays the most important role.

The first criterion is a modification of Lighthill [33]. It states that in a separation zone a positive curvature of the vorticity lines has to be observed across some wall shear stress lines. Vorticity lines are always oriented perpendicular to the wall shear stress lines (Figure 4.10). Hence this criterion matches Lighthill's shear stress line convergence criterion. Within a (narrow) separation zone, the general criterion for separation zone and line can be described by the fact that the vorticity lines have a large on-wall curvature. The vorticity line curvature in this zone reaches a maximum at the separation line (criterion 2). This allows a separation line to start from a fixed as well as an ordinary point. Satisfying criterion one and two, the initial location of an open separation zone and separation line is defined.

4.3.6 Surana et al. 2006

Surana et.al [38] derive a theory of three dimensional flow separation based on non-linear dynamical system methods. In their work asymptotic conditions for separation lines as

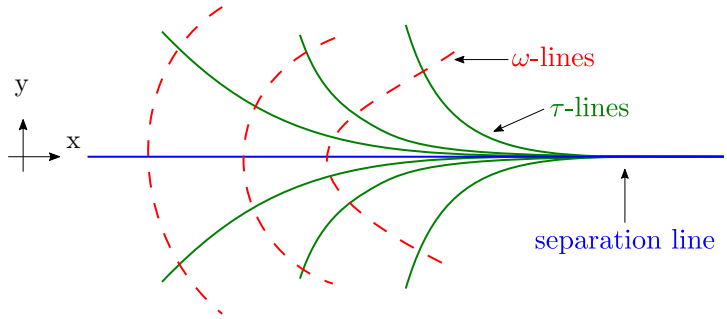

Figure 4.10: *Vorticity and shear stress lines across a separation line*

well as explicit formulae for separation angles are developed. These lead to the conclusion that only four types of locally unique separation lines can exist.

- (S1) saddle-focus connections
- (S2) saddle-node connections
- (S3) saddle limit cycle connections
- (S4) limit cycles

S1 and S2 correspond to the previously described horn and bubble separation. S3 and S4 are separation types which were not yet reported. In terms of open and closed separation, the first two belong to closed separation, while the latter two should be classified as open. Different from earlier open separation characterizations S3 and S4 admit unique separation lines and surfaces.
Requirements onto the separation profiles are

1. unique: no other separation profile or surface emanates from the same set of boundary points and no separation profiles or surfaces are admitted by nearby boundary points
2. bounded: they intersect the boundary in a bounded set
3. smooth: they are continuously differentiable
4. robust: they smoothly deform but survive under small perturbations

A separation line according to their definition must have a strong hyperbolicity and either connects singular points and limit cycles as described for S1 to S3 or be a limit cycle (S4). This implies that, the crossflow separation for instance described in Chapman & Yates [36], is not a separation in the understanding of Surana et.al. The main criticism is that a separation line has to be unique as stated in the requirements. A separation line identified from the view point of converging streamlines is no more distinguished than any other nearby segments, as all of them attract skin-friction lines, connect the same skin-friction zeros and repel off-wall fluid trajectories. Further, there is no unique separation surface emanating from the separation line candidate.

4.3.7 Summary of the classification concepts

The main classification concepts, used in the literature, are summarized in the following. For the later discussions, five types of separation are considered; the types described in Surana et. al [38] as well as the crossflow separation.

Maskel 1955

i) bubble separation	A closed region is built by a separation surface. Flow from the outside cannot enter this region (sketched in Figure 4.2).
ii) free vortex layer	A separation surface is formed and rolled up spirally. It consists of main flow fluid and flow from both sides of the separation surface can enter the separation region (Figure 4.2c).

Tobak & Peake 1982

i) global separation	After a change in parameters (e.g. Reynolds number) the pattern of singular points has changed (singular points disappear or new ones occur)
ii) local separation	After a change of parameters the singular point pattern remains (no new or vanishing singular points). Therefore the convergence of limiting streamlines is a local separation phenomenon.

Chapman & Yates 1991

i) Type I - bubble separation	Starts at a saddle point, whereby the separatrix divides the body in two regions. Outer flow cannot reach the region behind the separatrix (Figure 4.9a).
ii) Type II - horn separation	Emanates from a singular point. A foci of separation can be observed on the surface where the flow leaves the surface (Figure 4.9b).
iii) Crossflow separation	The surface pattern shows a convergence of limiting streamlines into a separation line, where the flow rolls up into a vortex sheet and leaves surface (sketched in Figure 4.9c).

Surana et.al 2006

i) saddle-focus separation	Corresponds to type II separation observed by Chapman & Yates [36] and shold be classified as a closed separation
ii) saddle-node separation	Corresponds to type I separation observed by Chapman & Yates [36] and should be classified as closed separtion
iii) saddle-limit cycle separation	This type was not yet reported before and should be classified as open separation. This pattern is characterized by a saddle point connected to a limit cycle.
iv) limit cycle	Similar to the previous type, this was not yet reported and should be classified as open separation. The pattern is characterized by a limit cycle not connected to any other singular point.

Chapter 5

Experimental Method

The experimental investigations were done on a Volvo S60 production car. For the tests the aerodynamic wind tunnel of Volvo Car Corporation in Gothenburg Sweden was used. More detailed specifications of the wind tunnel and the test vehicle are given in the following sections. Further the used measurement methods are described.

5.1 The Volvo full scale wind tunnel - PVT

All measurements are carried out in the full scale aerodynamic wind tunnel of Volvo Cars (**P**erson **V**agnar vind **T**unnel). In the following an overview of the technical specifications and the measuring system is given. Furthermore, it is explained how the force measurement system works and how a representative on-road condition can be simulated in the wind tunnel.

5.1.1 Technical specifications

The full scale aerodynamic wind tunnel at Volvo Car Corporation is a closed loop wind tunnel, Göttinger building type. It was built in the 1980s and was upgraded between 2006 and 2007. The test section, which is 6.6m wide and 4.1m tall ($A = 27.06\text{m}^2$) with slotted walls, is designed to range a full scale passenger car or a half scale truck. The free stream jet angularity is within $\pm 0.6°$ and the turbulence intensity is less than 0.1%. The uncertainties for the forces are determined throughout the whole balance system including the vehicle installation. The calculated values apply to the case that the car is removed from the balance and adjusted again. This leads to a coefficient uncertainty of $c_D = \pm 0.003$ for the drag and $c_L = \pm 0.004$ for the lift. The repeatability uncertainty of two measurements (without removing the car) is given in Table 5.1.

Table 5.1: *Repeatability uncertainties*

Δ drag	Δc_{D}	< 0.001
Δ lift front	Δc_{LF}	< 0.001
Δ lift rear	Δc_{LR}	< 0.005
tractive force WDU		$\pm$ 2N

To meet real word conditions and to increase the top speed, the wind tunnel was upgraded in 2006, where the main fan and its motor were changed and a moving ground system was installed. Furthermore a boundary layer control system was implemented to simulate on-road conditions. Detailed information about the operating mode and the relevance will be given in the subsequent sections. With the new fan, the power increased from 2.3 MW to 5 MW. Thereby, the maximum speed was increased up to 250 km/h. All detailed information about specification and the upgrade of the Volvo Car aerodynamic wind tunnel was described by Sternéus et. al. [39].

5.1.2 Moving ground system

The moving ground system improves the simulation of the real on-road conditions of a driven passenger car. With the moving ground there is no relative motion between ground and wind, so the wheels rotate with the wind speed of the incident flow. This affects the formation of the boundary layer and thereby the flow field around the vehicle. A detailed description concerning the influence of moving ground systems and wheel rotation on the aerodynamic drag is given in [40–44].

The moving ground system used in the PVT tunnel is a 5 belt rolling system, which is built up of one centre belt and four wheel drive units (WDU). It is built into a turntable to be able to carry out tests under yaw condition. The table has a diameter of 6.6 m and can be yawed $\pm 30°$. This allows a close to reality simulation without the need to prepare the car extensively. Moreover, individual control of the rotational speed for each wheel and the centre belt is possible.

5.1.3 Boundary layer control (BLC)

The main focus of using boundary layer control is to remove the oncoming boundary layer and to prevent it from growing. The boundary layer control systems consists of three different parts, which are used in parallel and shown in Figure 5.1. The first Boundary Layer Control (BLC) system is a boundary layer scoop, which is located near the leading edge of the test section. The scoop opening is 6.03 m wide and has a height of 0.075 m. It is controlled by a separate fan with a power of 250 kW. This fan is designed to remove a volume flow rate up to $30\,\mathrm{m}^3/\mathrm{s}$. The flow removed by the boundary layer scoop is re-injected at the wind tunnel roof, above the slotted walls.

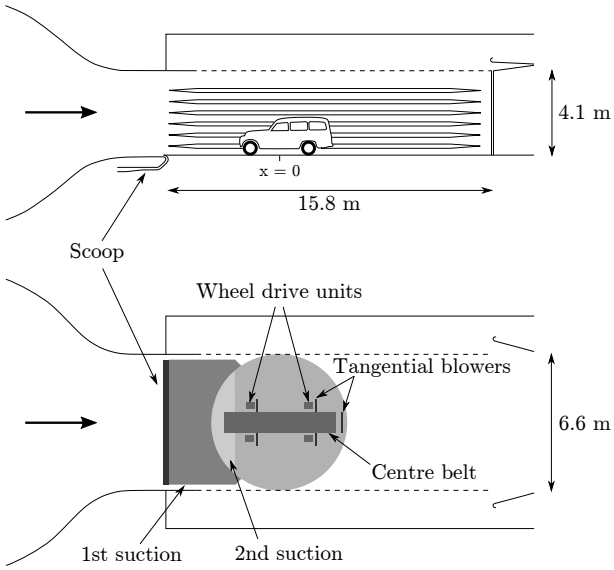

Figure 5.1: *Boundary layer control system [45]*

After the boundary layer scoop, two distributed suction systems follow (1st and 2nd). Perforated suction plates are used as part of the floor and the suction is controlled by one fan for each zone. The air from these two suction areas is reused to feed the following tangential blowing system; excess fluid is re-injected to the test section plenum behind the slotted walls. The first suction system is arranged directly after the boundary layer scoop, while the second starts at the turntable and reaches up to the front wheel drive units.

The third part is a tangential blowing system, which is installed behind each Wheel Drive Unit (WDU) and after the centre belt. The WDUs have to be moveable and adjustable for different wheel base lengths and wheel widths. Hence, a tangential blowing system is used to avoid the installation of a complex suction system. Furthermore, the apparent length of the belt can be extended by the use of this method and influence on the flow is smaller. Tangential blowing works with a high speed air jet, which is induced tangentially to the floor. As a result of the tangential blowing, energy is added to the flow, to prevent the boundary layer from growing. The height of the boundary layer is not reduced because the boundary layer is not removed but "refilled", contrary to the suction system. However, the displacement thickness is reduced. In addition, the rolling belts themselves reduce the development of a boundary layer.

5.2 Test object

The test vehicle is a S60 production car from Volvo Car Corporation with the specifications listed in Table 5.2. The vehicle is of notchback type and shown setup in the wind tunnel

Table 5.2: *Vehicle specifications*

vehicle geometry		wheel geometry	
model	Volvo S60, 2010	rim geometry	5 spoke rim
frontal area	2.27 m^2	rim width	7”
wheelbase (WB)	2.774 m	rim size	17”
length	4.63 m	tyre size	215/50R17
trim height front	0.675 m	tyre pressure front	2.5 bar
trim height rear	0.675 m	tyre pressure rear	2.5 bar

in Figure 5.2. Additionally the coordinate system is given. The x direction points downstream, the z direction points upwards and the y axis originates in the symmetry plane of the vehicle. Due to the frontal area of the vehicle in its relation to the wind tunnel cross section a blockage of 8 % occurs.

5.3 Pressure measurements

Two systems were available to take pressure measurements. One for time averaged measurements and one which also allows to obtain time resolved measurements. The time averaged system is a 8400 Data Acquisition unit from PSI pressure systems. The used pressure scanners are 64 port ESP Pressure scanners. These are differential pressure units with piezoresistive pressure sensors (one for each pressure port) with an accuracy of the full scale range of ±0.03%. To carry out the measurements, three ESP units with 64 ports can be used simultaneously. The pressure is read continuously with a frequency of 10 Hz. To get a stable value, the data recorded over 20 s (= 200 measurement values) is

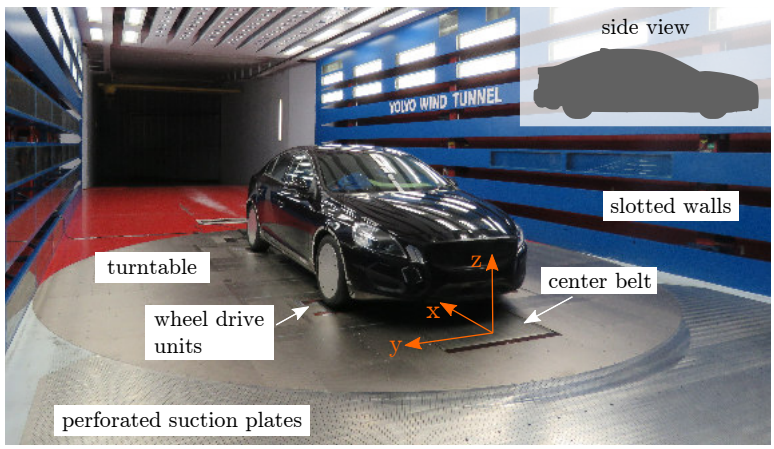

Figure 5.2: *S60 test object setup in the wind tunnel*

averaged by the pressure system. The reference pressures are taken at the tunnel inlet, after the nozzle contraction.

For the time resolved pressure measurements, unsteady pressure transducers (HCLA0025DB) from First Sensor-Sensor Techniques were used to acquire time resolve pressure data. The transducers measure a differential pressure, whereby the reference pressure was taken at the wind tunnel inlet after the nozzle contraction. The sensors were connected to the measurement location through drilled holes in the test object surface, using short tubes with a length less than 50 mm and a diameter of 1.5 mm. This setup ensures a smooth surface and no disturbances onto the near wall flow. The sensors have a range of ± 2500 Pa and an accuracy of ± 5 Pa. The sensitivity is about 0.000 799 9 V/Pa and the uncertainty is $5.2 \cdot 10^{-}7$ V/Pa. The tubing length between measurement location and data acquisition is within a range, where no transfer function correction is needed [46]. The pressure data is not corrected for wind tunnel blockage. Pressure measurements in the empty tunnel did not show any characteristic frequencies that can be attributed to the tunnel geometry and flow. At a sampling frequency of 1000 Hz, it was possible to take measurements for 15 sensors simultaneously. Data was recorded over 1 min (in some exceptions 10 min), while the frequency range of interest was below 100 Hz.

5.4 Paint visualizations

To visualize the surface streamlines, paint was used. A mixture of line oil, degreaser and titaniumoxid is attached to the surface. After starting the wind tunnel, the paint particles are dragged with the flow and leave the characteristic shear stress pattern on the surface. The mixture is very liquid, therefore it drops easily and it is hard to use this method for instance at the sides of the vehicle in order not to contaminate the moving belt system of the wind tunnel. Therefore paint visualizations are only available for the antenna region and the rear window.

5.5 Tuft visualizations

Another possibility to investigate the flow close to the surface is the usage of wool tufts. These are attached to the surface and react onto the near wall flow conditions. From the tuft orientation a qualitative picture of the near wall flow can be obtained. Further, areas of high unsteadiness can be identified depending on the tuft fluctuation.

To get out even more quantitative information, an advanced tuft method can be used. The main idea behind this method is to take a number of snapshots of the tuft movements. Approximately 1000 images turned out to be a sufficient number in order to get a good picture. The single snapshots are evaluated regarding the position of each tuft and its geometric orientation. The series of images provides in that way a set of data containing the tuft orientation in each snapshot. Out of this data set it is then possible to calculate a time averaged limiting streamline pattern as well as the information about the tuft

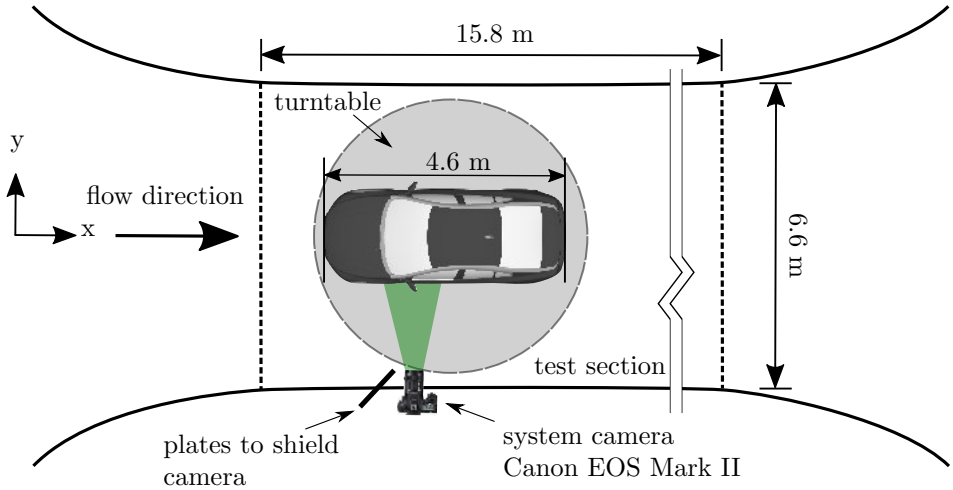

Figure 5.3: *Experimental setup of the tuft image acquisition at the side of the vehicle [2]*

angle fluctuation. Detailed descriptions about the method and its applications can be found in [2, 6, 9, 47, 48].

For the image acquisition a standard system camera is sufficient. For the experiments in this work a Canon EOS 5D Mark II with different lenses was used to acquire the images. The images were not taken with an equidistant time step. Figure 5.3 shows the experimental setup for the image acquisition on the side of the vehicle. A similar setup was used to record the images from a top view, where the camera was mounted in the ceiling of the wind tunnel. The exposure time was adjusted in order to get sharp images of the tufts (approximately 1/800 s). Regions with high tuft fluctuation require hence a shorter exposure time than areas with attached flow.

Chapter 6

Numerical Method

The numerical simulations were performed on a virtual model, based on the physical full scale vehicle. Details about the geometry and the numerical approach are given in the following sections. For the pre-processing the software Ansa v.14 was used, followed by the wrapping, meshing, solving and post processing, which was done in StarCCM+ v.12.04.

6.1 Computational domain and geometry specification

The computational domain, representing the wind tunnel, was 47 m long, 9.5 m wide and had a height of 10 m. The model was positioned 16 m after the inlet. Figure 6.1 shows the tunnel domain and the location of the test object. The boundary conditions were a velocity inlet and a pressure outlet. The road condition was simulated by a moving

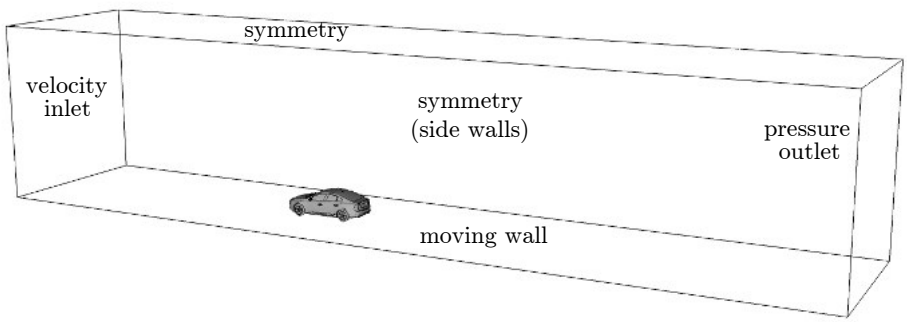

Figure 6.1: *Numerical wind tunnel*

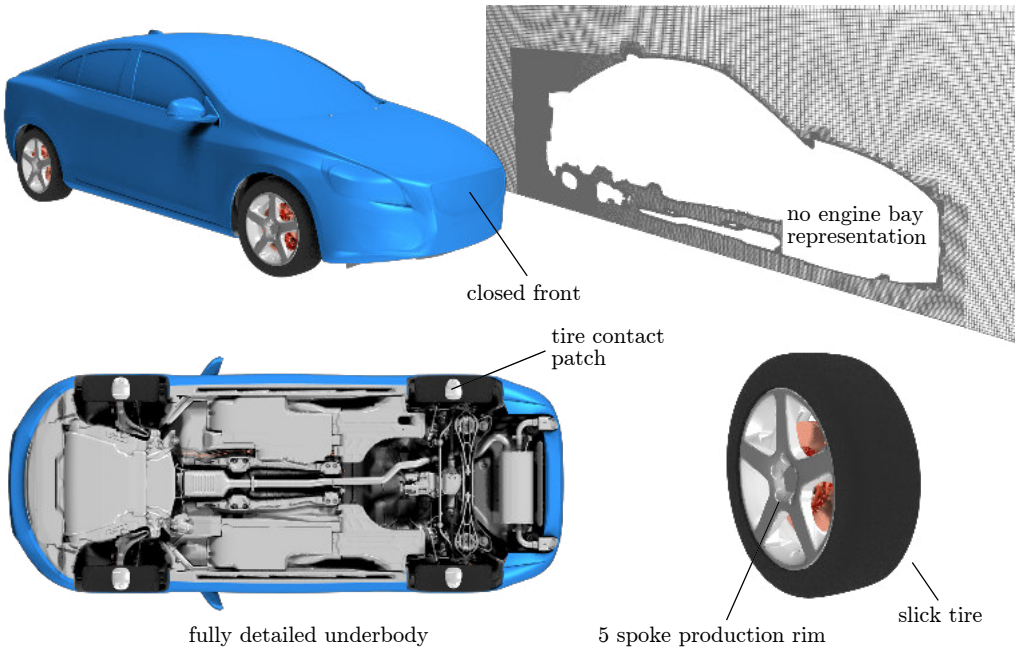

Figure 6.2: *Virtual vehicle model*

wall condition (wall velocity = 100 km/h). The numerical model is a Volvo S60 full scale passenger car of sedan type, shown in Figure 6.2. To reduce complexity and case size, a closed front model was used, which means that the engine bay was shielded off and was not a part of the simulation. The underbody geometry was fully detailed. The rim geometry was according to a five spoke production rim. The tires were slicks, morphed around the contact patch to represent the load.

6.2 Mesh specifications

The volume mesh was of hexahedral type with prism layers on the ground and the vehicle surface. The surface cell sizes were between 1 mm and 10 mm. The number and height of prism layers were chosen depending on the desired boundary layer resolution. On the vehicle exterior, it was required to resolve the boundary layer which required y^+ values below one. Therefore, 12 prism layers were built, with a near wall thickness of 0.01 mm for the first cell. The total prism layer height was 7 mm which resulted in a growth rate of 1.6. The wall y^+ distribution on the vehicle body is shown in Figure 6.3.

Around the car four refinement boxes were used to increase the growth of the cell sizes step wise, reaching a target cell size on the wind tunnel walls of 320 mm. The mesh refinement zones are shown in Figure 6.4. The first level refined the underbody and the near wake with target sizes of 10 mm. Level two increased the cells to 20 mm, level three

to 40 mm and the last level built cells of 80 mm. The mesh setup lead to a total volume mesh size of 82 million cells.

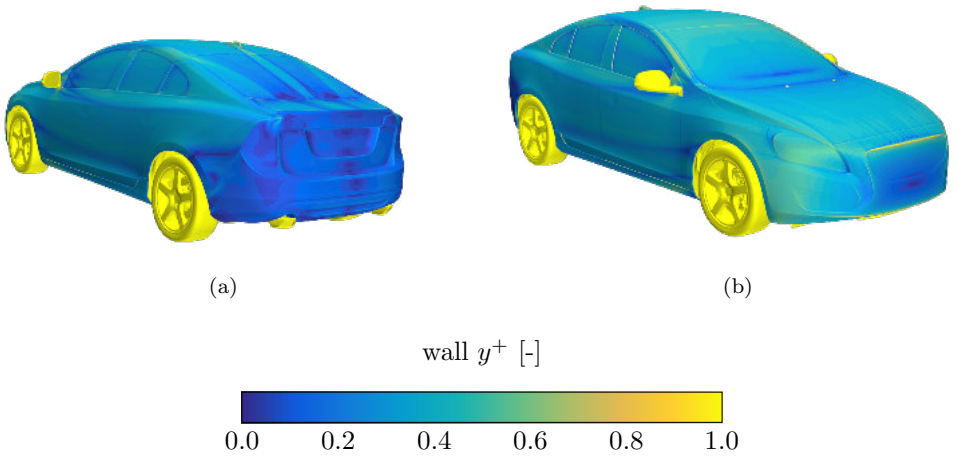

Figure 6.3: *Wall y^+ distribution on the vehicle body*

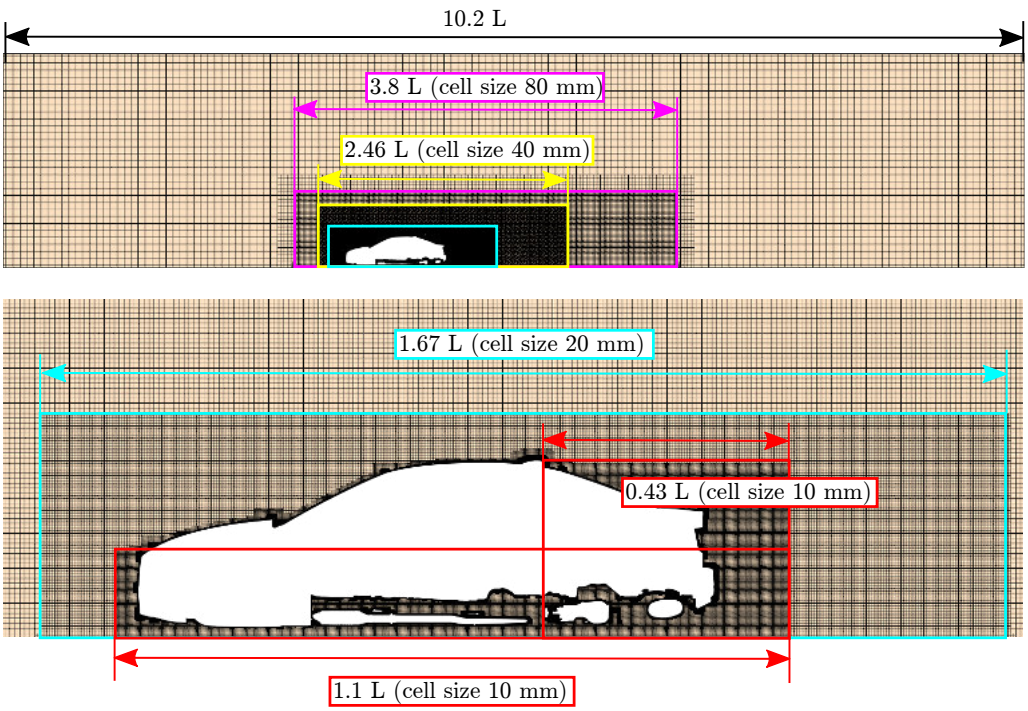

Figure 6.4: *Mesh refinement zones*

6.3 Solver specifications

The simulations were performed with a steady state RANS setup for incompressible flows. The turbulence model used was the $k-\omega$ SST. The software allows to handle different wall distances, based on the calculated y^+ values with the so-called *all y^+ treatment* function. This implementation is a hybrid which attempts to combine meshes with low and high y^+ ranges and produces even reasonable results in the area of intermediate meshes of $1 < y^+ < 30$.

The inlet velocity, the moving ground velocity and the wheel rotation were set to represent a driving condition of 100 km/h, which corresponds to a Reynolds number of $\mathrm{Re} = 8.4 \cdot 10^6$ based on a vehicle length of $L = 4.63\,\mathrm{m}$. The direction of the inlet velocity was zero degree yaw which was normal to the inlet. The wheel rotation was modelled with the Multiple Refrence Frame (MRF) approach for the volume within the spokes and with a moving wall condition on the tires.

A coupled implicit solver with a 2nd order discretization scheme was used, which solves the equations of conservation simultaneously as a vector of equations. The Courant number for the coupled implicit steady state solver in Star CCM+ controls the local pseudo-time-step size and affects the convergence speeds. Its value was ramped for the first 200 iterations, before it was set to a constant value of 50. The variable gradients are computed using the *Hybrid Gauss Least Square Method*.

The convergence was determined by the residuals of the dependent variables and the dimensionless drag force coefficient, c_D. The criterion was set to reach residuals below 0.001 and a c_D within ± 0.001 of the absolute c_D over the last 1000 iterations.

6.4 Mesh investigation

For the analysis of the near wall topology it is necessary to secure a mesh independent limiting streamline pattern. Hence, the resolution of the boundary layer is a determining parameter. Figure 2.2 shows how the limiting streamline pattern changes plotting the velocity components at different distances z from the surface. The importance of the boundary layer resolution is shown in Figure 6.5, where the wall shear stress lines on the exterior and the surface coloured by the x-vorticity are presented. Along the A-pillar, significant changes can be observed with different y^+ values. For a high y^+ resolution (Figure 6.5a) the A-pillar curvature has a positive surface vorticity and the wall shear stress lines do not show any characteristic development. Refining the boundary layer resolution (Figure 6.5b) shows that a change in x-vorticity is created over the pillar curvature. Additionally, the wall shear stress lines are converging along the A-pillar, exactly where the change in vorticity can be observed. An even finer resolution of $y^+ < 1$ (Figure 6.5c) does not change the pattern. The drag coefficient for the three different cases did not change significantly ($\Delta c_{\mathrm{D,max}} = 0.002$).

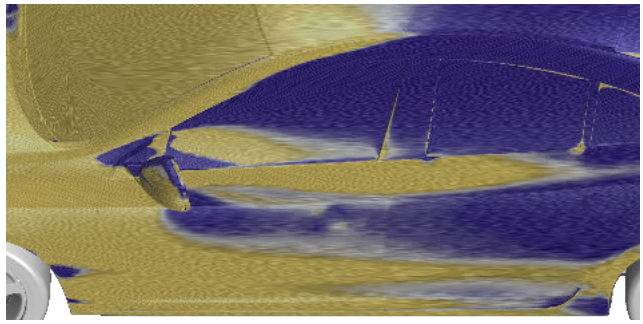

(a) $y^+ > 30$

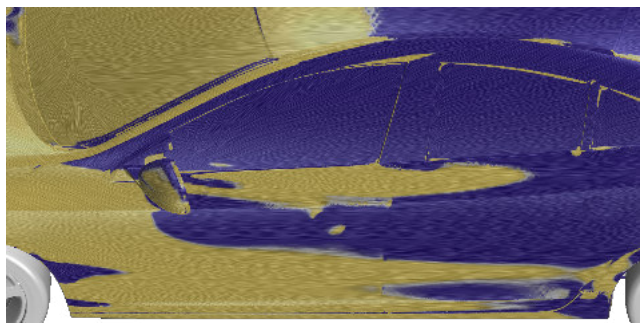

(b) $y^+ \approx 5$

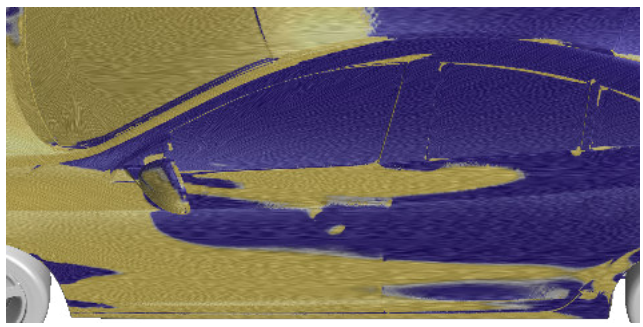

(c) $y^+ < 1$

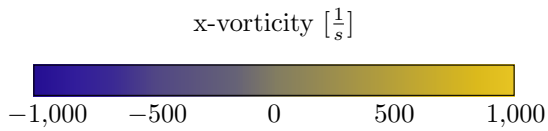

Figure 6.5: *x-vorticity distribution with limiting streamlines for three different mesh configurations*

Chapter 7

Identification of Separation

Based on the types of separation introduced in Section 4, potential flow separation regions are identified on the exterior of a passenger car, studying their flow topology. Different areas on the vehicle are discussed; starting with the flow around the antenna and over the rear window, before discussing the A-pillar region, the flow downstream of the front wheelhouse and on the base.

7.1 Surface flow pattern around the antenna

In the following the flow topology and different surface parameters around the antenna are analysed. Figure 7.1 shows the investigated area. The flow around the antenna is in the manner of flow topology an interesting area, but has not yet been investigated in literature.

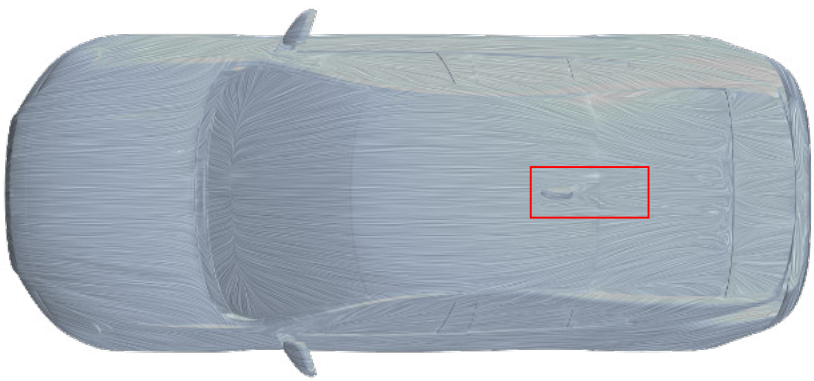

Figure 7.1: *Area of investigation behind the antenna*

However, the flow around surface mounted obstacles is reported for different geometries. The vehicle antenna represents a symmetric 3D body connected to an almost flat wall, without any perturbations due to flow interactions resulting from other phenomena. Therefore it is possible to study the flow topology and how it compares with phenomena observed for other geometries. Based on the topology, presumed separation patterns are identified. Further, the correlation of the limiting streamline pattern with different surface parameters will be investigated. Before the antenna geometry, and its flow pattern are studied, a short review on junction flows is given.

7.1.1 Review on junction flows

The flow topology of 3D bodies connected to a wall is described in many different publications and textbooks, as for instance in [16, 24, 49–51]. The flow approaching the obstacle has to split, to go around the geometry (Figure 7.2). In front of the body the flow will stagnate and the pressure in this are will increase. Close to the body-wall intersection this pressure increase is also transmitted to the ground. As a result the boundary layer in front of the body separates and rolls up into a horseshoe vortex, as shown in Figure 7.2a. Underneath this primary horseshoe vortex, secondary and even more vortices can be created (sketched in Figure 7.2b). The rotation of the primary vortex matches the rotation of the approaching boundary layer, while smaller secondary vortices rotate with opposite sign, to preserve streamline topology [51].

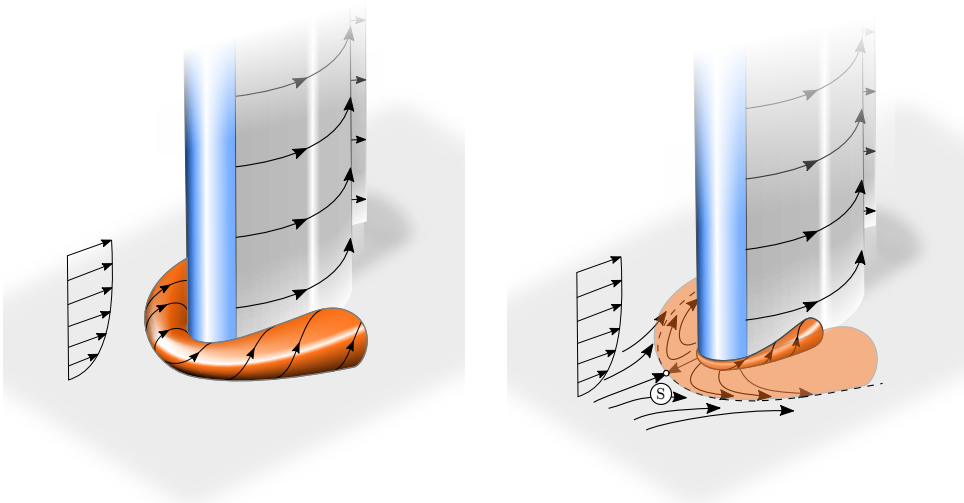

(a) *occurring primary horseshoe vortex*

(b) *secondary horseshoe vortex and topological surface pattern*

Figure 7.2: *Schematic flow around a cylinder mounted to the ground*

The topological pattern created on the ground directly in front of the obstacle is also shown in Figure 7.2b. The separating boundary layer creates the stagnation saddle (Ⓢ), from which two separatrices are emanating and go around the geometry. Along this separatrices the flow to the left and right of the separating vortex layer converges. A similar topological pattern is also observed for other geometries connected to a wall, for instance wing profiles or cubes [16, 24, 49–51].

7.1.2 Flow topology

The limiting streamline pattern around the antenna shows several critical points and bifurcation lines. Figure 7.3 shows the wall shear stress pattern around the antenna, obtained from Computational Fluid Dynamics (CFD) (Figure 7.3a) and from paint visualisations (Figure 7.3b). Red lines show selected wall shear stress lines to allow a better identification of the pattern. The results show the very good agreement of the two methods used. In both images a saddle point S_S in front of the antenna nose can

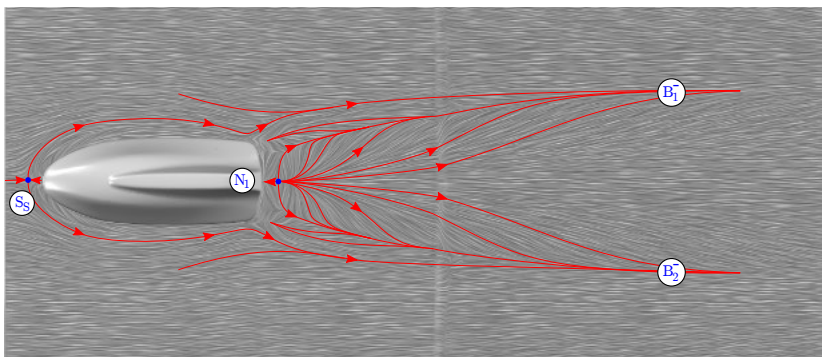

(a) *CFD*

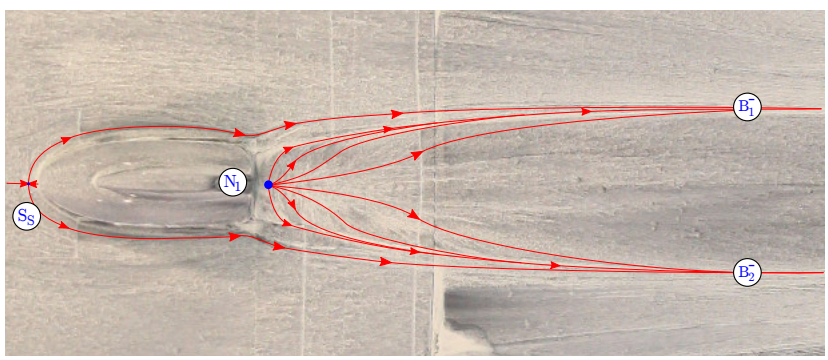

(b) *experiment*

Figure 7.3: *Numerical and experimental limiting streamline pattern around the antenna - top view*

be detected which splits the flow to go around the antenna geometry. Such a pattern is characteristic for the flow around 3D bodies connected to a wall and is also observed around generic bodies, as described in the previous Section 7.1.1. Behind the antenna two negative bifurcation lines, B_1^- and B_2^-, can be found. These are potential convergence lines, which could lead to a cross flow separation (CFS). From the centreline streamlines diverge to the sides and converge towards the wall shear stress lines B_1^- and B_2^-. Therefore the centreline is a positive bifurcation line. The inner limiting streamlines emanate from a node point of attachment (N_1), created by the reattachment of the antenna wake.

The pattern on the antenna shows further characteristics (Figure 7.4a and 7.4b). The stagnation saddle was already shown in Figure 7.3. On the antenna nose a stagnation point N_S can be found. This is where the oncoming flow hits the antenna surface and attaches. Starting from node point N_S a positive bifurcation line B_1^+ emanates from which the limiting streamlines diverge.

On the antenna base several singular points can be identified, as sketched in Figure 7.4b. The pattern on and around the antenna is symmetric. To identify all the characteristics, an enlarged view is shown in Figure 7.4c together with the experimental result (Figure 7.4d). Comparing the pattern obtained from CFD and experiment, it can be seen that the simulation shows finer details compared to the paint visualisation. On the antenna base the experiment shows a focus on the right side. The simulation does not indicate a focus but shows a node point of separation in this area. The saddle point S_7 in Figure 7.4c is not clearly represented in the paint picture; however due to the flow directions identified, a saddle point is needed to construct the observed topology. Hence, the sketched saddle point S_1 in Figure 7.4d can be expected. S_1 in the experiment seems to be located closer to the vehicle roof than the corresponding point S_7 in CFD. Over the antenna top the identified bifurcation line ends in the saddle point S_6. This singular point cannot be identified from the experiment.

In the enlarged view (Figure 7.4c) the limiting streamline pattern on the left hand side is highlighted by representations of selected red wall shear stress lines. As the pattern is symmetric, correspondents of the shown singular points are appearing on the right hand side as well. As already mentioned, the bifurcation line B_1^+ ends in the saddle point S_6, which is followed by the node point N_6. This combination shows that the surface flow is directed upstream within these two points. This leads to the assumption that a small separation takes place which would, according to Maskell [24] and Chapman & Yates [36], be of bubble type with N_6 as the node of attachment. Following the flow from N_6, the wall shear stress line ends in the saddle point S_7 which is created at the antenna base. The line between N_6 and S_7 is again a positive bifurcation line, as limiting streamlines are diverging. Further bifurcation lines are found on the rounded edges at the rear. Between S_6 and N_5 wall shear stress lines are converging. Directly next to this negative bifurcation line an almost parallel, but shorter positive bifurcation line exits, to which another convergence line is located. All areas where negative bifurcation lines are observed, are potential candidates for a CFS.

On the lower rear end edge, where the antenna intersects with the roof, the highest density of singular points can be detected. The wall shear stress lines around node N_5

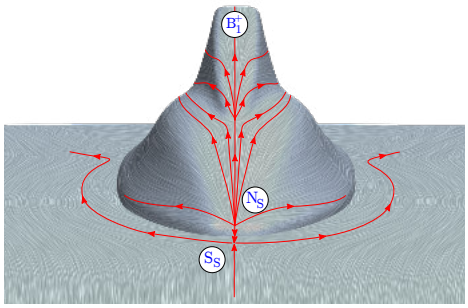

(a) *front view - CFD*

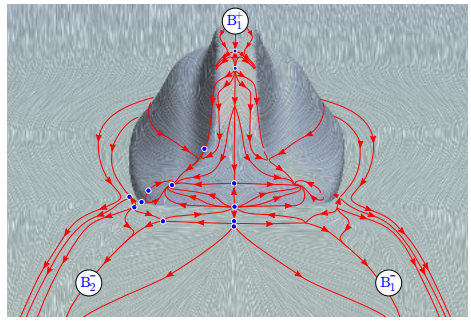

(b) *rear view - CFD*

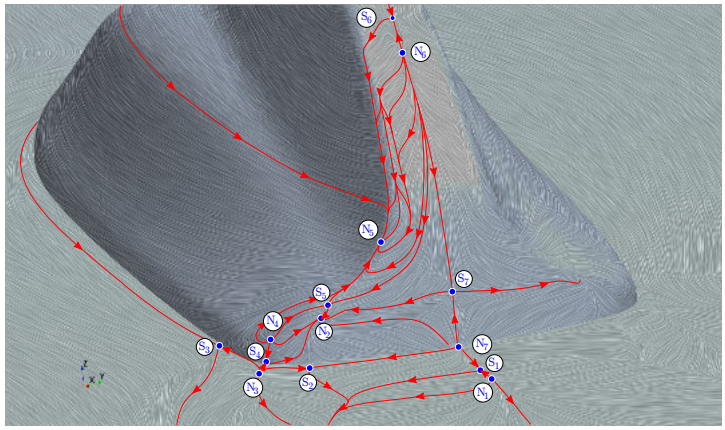

(c) *rear view enlarged - CFD*

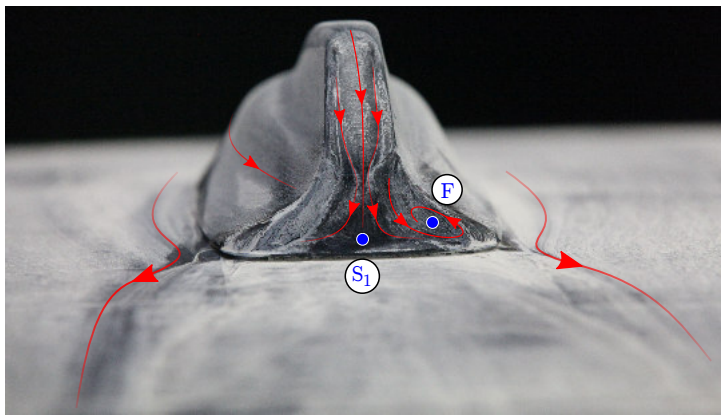

(d) *rear view - experiment*

Figure 7.4: *Detailed limiting streamline pattern around the antenna - front and rear view*

are directed towards N_5. Hence it is a node point of separation, alike node N_2. In N_1, N_3, N_4 and N_7 the limiting streamlines are pointing away, which mark node points of attachment. The node-saddle combination S_1-N_1 is similar to S_6-N_6 and indicates also the existence of a small bubble.

In Section 4.3.3 topological rules were defined on how many nodes and saddle points are created for different cases. One rule concerns the number of singular points for a 3D body connected to a wall. For the antenna connected to the roof this test can be made. The rule states that the number of nodes and saddles have to be the same. Around the antenna 12 saddle points and 12 node points are identified (including the symmetric correspondents), hence the rule is satisfied.

It might be that saddles and nodes lie very close to each other. This issue of scale was also discussed by Chapman & Yates [36] and it was shown that a merge of singular points is not a problem for the overall topological discussion and the application of topological rules (see also Section 4.3.4). In Figure 7.4c $N1$, S_1 and N_7 lie very close to each other. If these three points would merge together due to a larger scale, the large-scale appearance would be a node point of attachment. This effect could be seen in Figure 7.3, where only a node point of attachment (N_1) was identified instead of a node-saddle-node combination.

7.1.3 Surface properties

Besides the limiting streamline pattern the development of different surface parameters is of interest. The wall shear stress magnitude, the surface pressure and the surface vorticity are selected to be analysed in more detail. It shall be investigated if the different distributions show a characteristic behaviour in the separation areas and if correlations among them can be found.

Figure 7.5 shows the wall shear stress lines and the surface coloured by the wall shear stress magnitude from the top view. In front of the antenna nose the saddle S_S is created and splits the flow. In this singular point the wall shear stress is lower than around it. A similar observation can be made for all other identified singular points. However, a low wall shear stress is not limited to these critical points. Along the negative bifurcation lines B_1^- and B_2^- downstream of the antenna, the wall shear stress is low as well. Further areas with a low wall shear stress are found along the rounded rear end edges, where additional negative bifurcation lines appear. In all singular points, the wall shear stress reaches zero; however, the wall shear stress does not necessarily reach zero in areas of CFS separation. This is one main observation in 3D separation contrary to the 2D case where one necessary condition for the separation point is zero wall shear stress (see Section 4.1).

The surface coloured by the surface pressure is shown in Figure 7.6. In front of the antenna nose a high pressure is created due to the stagnation of the oncoming flow. Likewise a higher pressure is created along the points S_7 to N_1 behind the antenna and at the rear end corners around N_3 to N_4. Along the bifurcation lines B_1^- and B_2^- lower pressure regions can be observed. These extend downstream next to the bifurcation

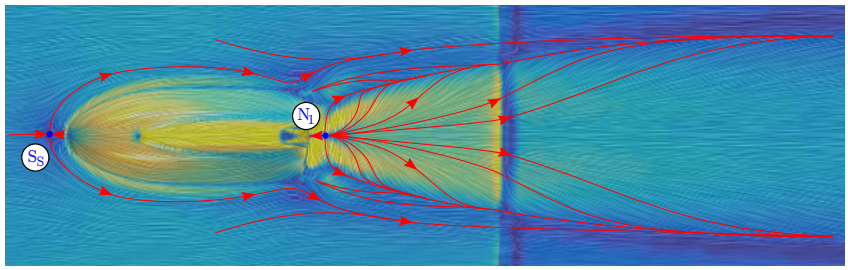

(a)

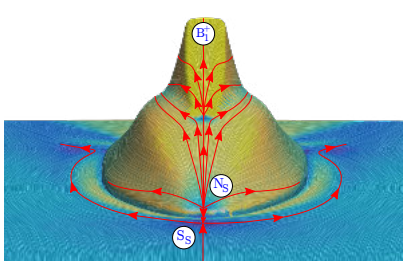

(b) *front view*

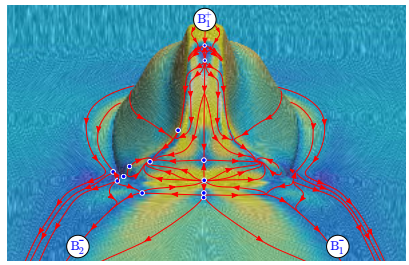

(c) *rear view*

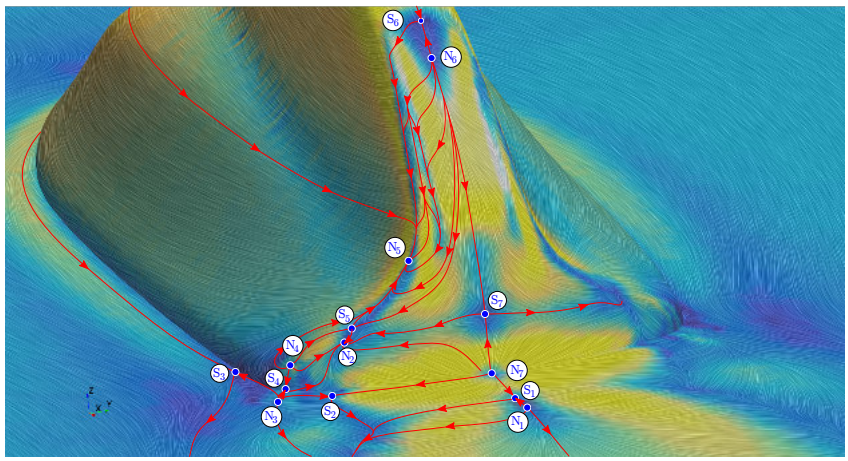

(d) *enlarged rear angle view*

wall shear stress $[Pa]$

Figure 7.5: *Limiting streamline pattern around the antenna; surface coloured by wall shear stress magnitude*

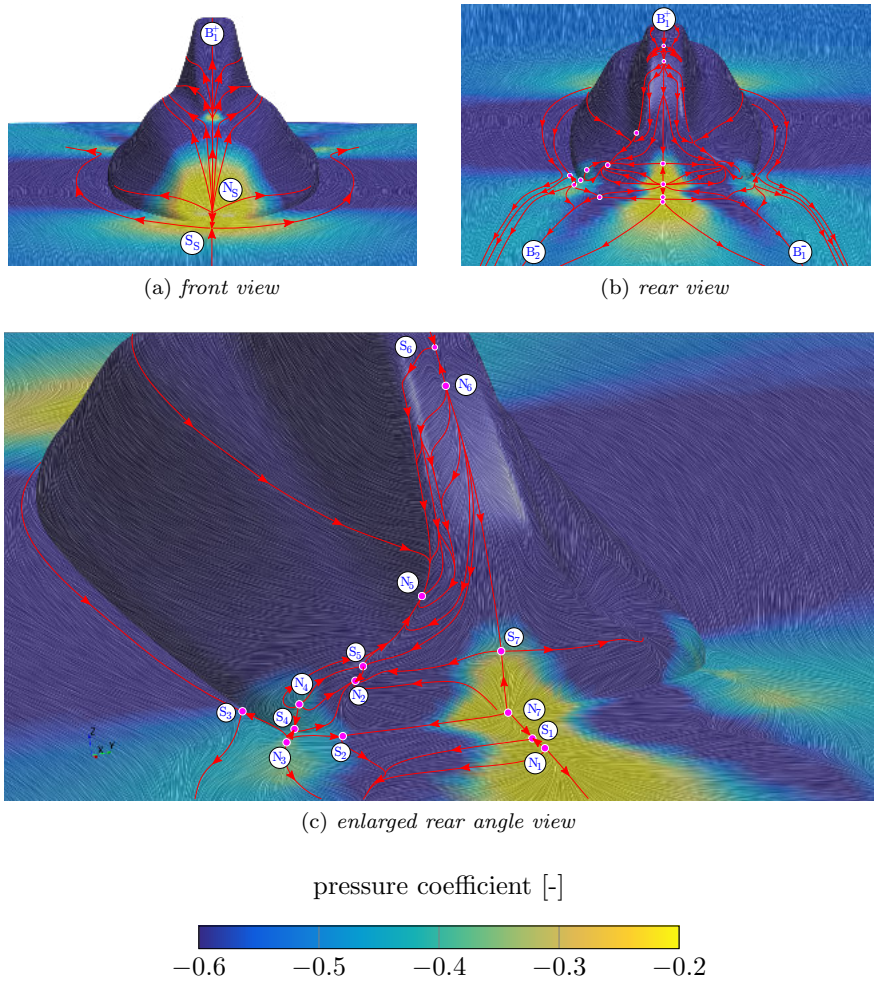

(a) *front view*

(b) *rear view*

(c) *enlarged rear angle view*

Figure 7.6: *Limiting streamline pattern around the antenna; surface coloured by pressure coefficient*

lines. According to theory, streamlines are dragged towards the lower pressure, hence it is expected to observe the lowest pressure underneath the convergence lines. The transverse pressure gradients are very weak which makes it difficult to identify the pressure minima. Additionally it has to be considered that apart from the pressure forces, viscous forces are acting, which drag the flow downstream over the rear window. The qualitative analysis shows that the lower pressure legs are created to the right and left of the bifurcation lines B_2^- and B_1^-. Compared to the wall shear stress distribution it seems to be difficult to generally correlate the occurrence of singular points with a pressure level, however the node points of attachment seem to show a higher pressure level than the surrounding.

This observation holds for all the attachment nodes apart from N_6. It has also to be noted that the pressure gradients on the surface are quite weak, which makes the appearance of "high" pressure levels very sensitive to the chosen colour range. Changing for instance the range to $[-0.1; 0.1]$ (not shown here) the node points around the corner edge would not appear any longer as high pressure spots, while the stagnation nodes in front (N_S) and behind (N_7 and N_1) are still areas of high pressure.

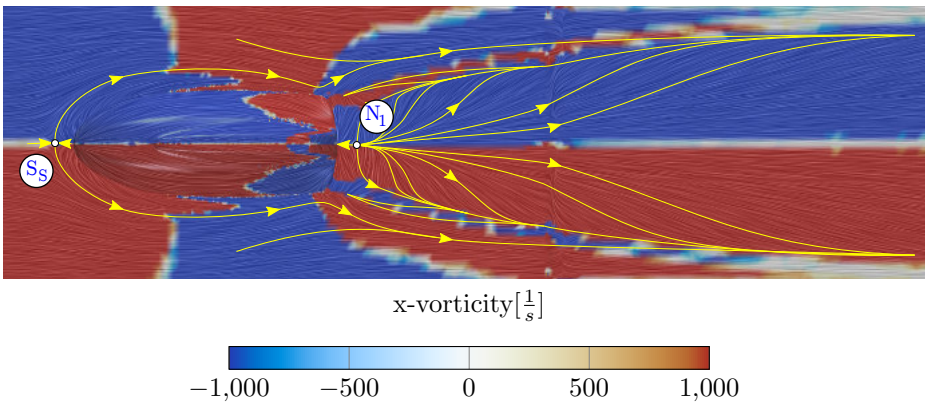

Figure 7.7: *Limiting streamline pattern around the antenna; surface coloured by x-vorticity*

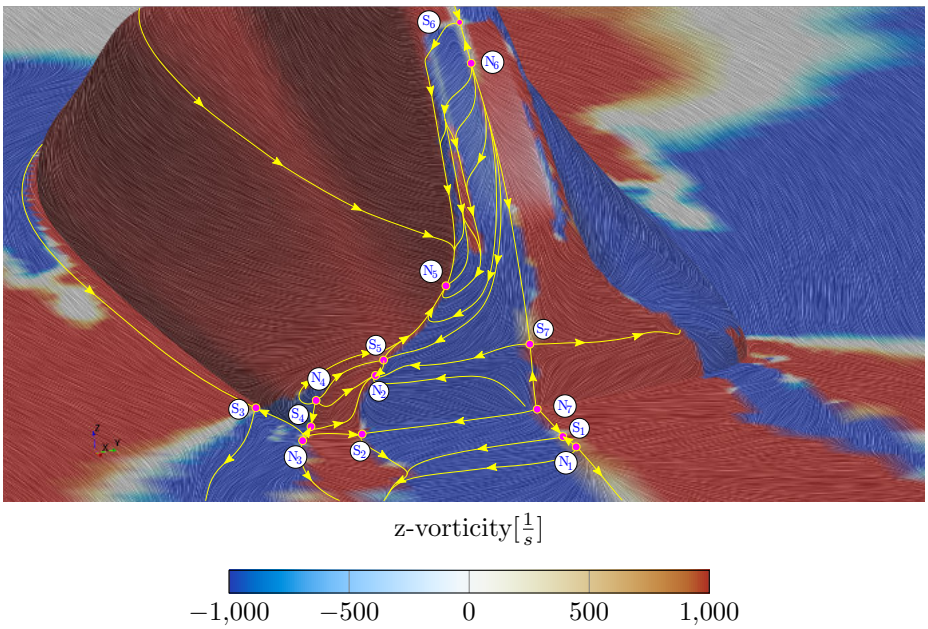

Figure 7.8: *Detailed limiting streamline pattern on the antenna rear end; surface coloured by z-vorticity*

Regarding the surface vorticity, the distribution of single components is considered in order to be able to get information about the orientation of developing vortices and their sense of rotation. Therefore it is for instance advantageous to investigate the x-vorticity (direction of the main flow) when longitudinal structures are conjectured while the y component can give insight into the development of transverse structures (y and z direction). The distribution of the x component of surface vorticity is shown in Figure 7.7. Of interest in this figure is the area downstream of the antenna. At the centreline a jump in the sign of x-vorticity can be seen. Vorticity lines are always perpendicular to wall shear stress lines. Along the centreline, which is a positive bifurcation line, the vorticity lines have an apex at which the directions of the slope of the vorticity lines change, which results in the observed change in sign of x-vorticity. Along the centreline, the x-vorticity is zero; however, the gradients are very large, which appear in a jump of the x-vorticity values. Along the bifurcation lines B_1^- and B_2^- another jump in sign can be observed. These convergence lines indicate the development of longitudinal vortices due to a CFS, hence along the bifurcation line a vortex sheet has to leave the surface. Where and how that happens will be discussed in a following chapter (Chapter 8.1) when the development of separation structures into the flow is discussed in more detail. Between S_6 and N_5 another negative bifurcation line was detected as well as one parallel to it and also between S_5 and N_5 the limiting streamlines are converging on the connecting line. Figure 7.8 shows the antenna rear end coloured by z-vorticity. Along the described bifurcation lines a jump in z-vorticity can be observed, which is presumed to cause transverse vortices.

7.2 Surface flow pattern over the rear window

The flow topology over the rear end geometry is an area which was already in the focus of many other researchers. Still, the exact mechanisms behind the created patterns are not yet fully understood. Before analysing the limiting streamline pattern and the surface properties of the studied vehicle model, a brief overview of some investigations found in the literature is given.

7.2.1 Review on the rear end flow topology of vehicle geometries

In literature, several investigations are presented, which study the wall shear stress pattern behind different rear end geometries. The concept of limiting streamlines and singular points was first introduced by Chometon [52]. In his work he used these concepts together with total pressure tomography to reconstruct the flow structure on a RENAULT 21 scale model and an AEROPLUS test model.

Jenkins [53] investigated a Ford C1 16% scale model regarding the occurring flow structures and separation phenomena. He found characteristic features which not necessarily match with the general known structures. The separation was dominated by two foci emanating from the decklid behind the backlight, which then extend downstream towards the centre of the decklid.

In 2001, Gilhome et.al. [54] investigated two types of notchback vehicles; a Ford Falcon and an AU Falcon in full scale. The surface flow pattern was analysed by means of paint visualization, smoke and (unsteady) surface pressure measurements and the concept of critical points was used to characterize the pattern and to connect it to separation and attachment phenomena. A main finding was the occurrence of the so-called hairpin vortex, which was shown with injected smoke. The surface topology showed in both cases the occurrence of two symmetrically distributed foci on the rear window and two symmetrically distributed node points of attachment on the trunk. In the case of the AU Falcon the foci were located left and right of the centreline at the lower rear window edge. For the EF Falcon the foci were found further upstream in the upper half of the rear window.

An investigation using near wall Particle Image Velocimetry (PIV) was done by Depardon et.al. [55]. They investigated the surface and wake pattern of 1/4 Citroen C4 scale models with different rear end configurations - three straight slant configurations and a rounded rear end geometry. In their investigation two symmetrically distributed foci were found, which were located at the upper edge of the rear end slant. They further found that the topological pattern on the surface did not show any Reynolds number dependency. A comparison of the 10° and 41° slant configuration showed different positions of occurring singular points, but the same number and type; similar to a square back pattern. They conclude from that, that the wake structures for these two configurations should also have an identical pattern. The 30° slant and rounded configuration showed a surface pattern, observed at fastback geometries.

For some notchback configurations an asymmetric flow over the rear window could be observed, for instance in [56, 57].Gaylard et.al. [56] investigated this phenomenon in more detail. By analysing the flow pattern and occurring singular points, similar structures could be observed. Occurring singular points were distributed differently, but seemed to be the same for the symmetric and asymmetric flow pattern. They therefore assume that this asymmetry is a degraded case of the symmetric flow pattern.

A more detailed study regarding the connection between flow asymmetry and the notchback geometry was done by Sims-Williams et al. [58] on generic vehicle models. It was found that the flow pattern can be characterized as reattaching asymmetric, reattaching symmetric or fully separated, depended on the notch depth and the effective backlight angle. A direct comparison of the rear end pattern was done by Wieser et al. [57] using the DrivAer model. Their investigation match the finding of a asymmetric pattern for the notchback geometry and asymmetric pattern for the fastback, where the two foci were found on the lower edge of the rear window; close to the centreline.

All investigations showed how singular points are used to characterize the flow in order to be able to understand the flow structures and the geometrical influence. However, it is still unclear how the different patterns are formed. Comparisons with the surface pressure were made in some investigations, but the results are still not satisfying regarding the driving forces. Though, it could be seen that main features are present in all vehicle shapes. At least two nodes could be found as well as two foci. The nodes appear on the trunk or on the vehicle base, while the foci are distributed on the rear screen.

7.2.2 Flow topology

Figure 7.9a shows the wall shear stress pattern over the rear window. The pattern is symmetric respective to the centreline, therefore the singular points are only labelled for the right hand side. It can be seen that the critical points occur mostly at the lower window area. The node N_1 appeared already in the previous section. From this node of attachment most streamlines end in the focus points F_1 and its symmetric respective on the left side of the centreline. The bifurcation line B_1^- created behind the antenna ends in the saddle S_2, where the flow splits up and creates the two counter rotating foci F_1 and F_2. From the upper right and left window corner a positive bifurcation line emanates. The limiting streamlines diverging from this line end in the Focus F_4, the saddle point S_5 and the focus F_5. The enlarged view in Figure 7.9b shows that another saddle point (S_4) is created between the foci F_3 and F_4. The upstream flow emanates as well from the bifurcation line, which starts in the upper right corner. Contrary to the first focus pair, F_3 and F_4 have the same sense of rotation.

Comparing this pattern with the wall shear stress map obtained from experiment (Figure 7.9c), shows an overall good agreement. A main difference occurs in the created foci pairs. It can be seen that the saddle points S_1 and S_5 correspond to the findings from CFD as well as the occurrence of N_1 and F_5. The experiment shows that two counter rotating foci pairs are created from the saddle point S_2 at the lower window edge (F_1 and F_2). The separatrix ending in the saddle point S_2 emanates from an upstream flow coming over the vehicle roof. The limiting streamline emanating from the node point N_1, ends in the saddle point S_3. This is another significant difference compared to the CFD result. Looking back into the CFD pattern (Figure 7.9a) shows that the limiting streamline emanating from N_1 ends in the saddle point S_2, creating the counter rotating foci F_1 and F_2. A separatrix ending in a saddle point, as it was observed in the experiment can be found in CFD as well. This would be the line coming over the vehicle roof and ending in S_3.

A reason for these discrepancies could be differences in the geometry representation. While the CFD model is a stiff water tight model, meaning that all gaps are closed and the surface cannot deform, the real car has a rubber lip in the edge between lower rear window and trunk. Hence it might be that the stagnation of flow in S_1 is higher in CFD compared to the experiment. Therefore the flow is stronger pushed away to the left and right. As from S_5 flow is directed towards the centreline, the two flows merge and create S_3. The created foci in the CFD pattern is the result of the different flow directions balancing out.

Figure 7.10 shows the limiting streamline pattern obtained from tuft visualisation overlaid with the pattern from the paint visualisation. It can be seen that both methods show very good agreement. The location of the foci structures and their size are well replicated with the tuft method. Also the sense of rotation can be identified. Following the limiting streamlines emanating from the window corners the in-wash towards the centreline can be observed. Towards the lower window edge the limiting streamlines diverge. Over the trunk two convergence lines can be found, as well as a divergence line along the centreline. The

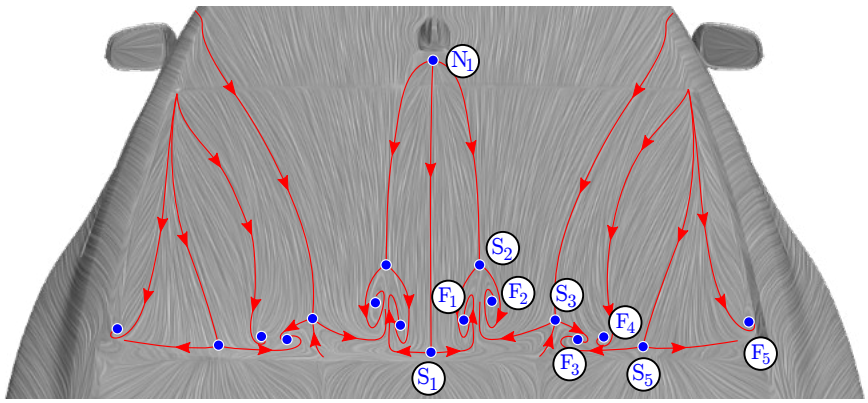

(a) *CFD*

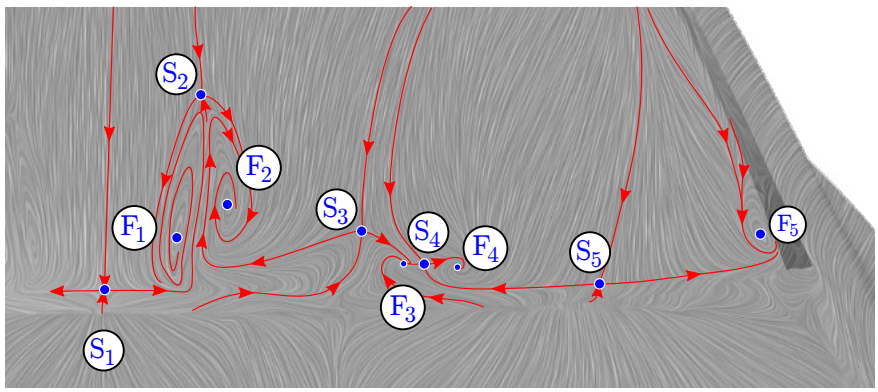

(b) *CFD enlarged*

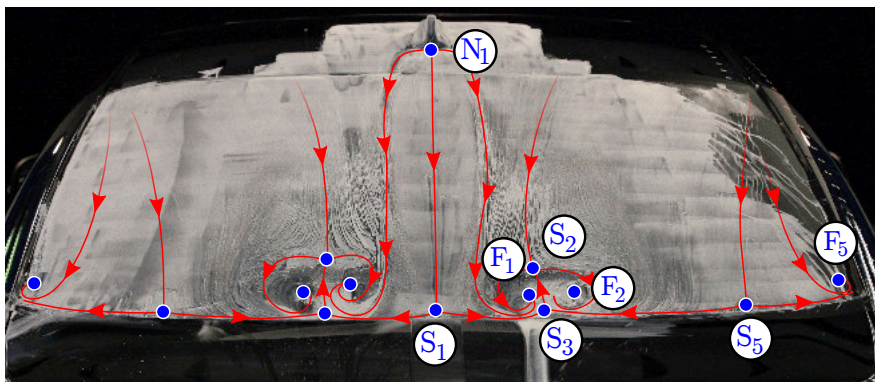

(c) *experiment*

Figure 7.9: *Limiting streamline pattern over the rear window*

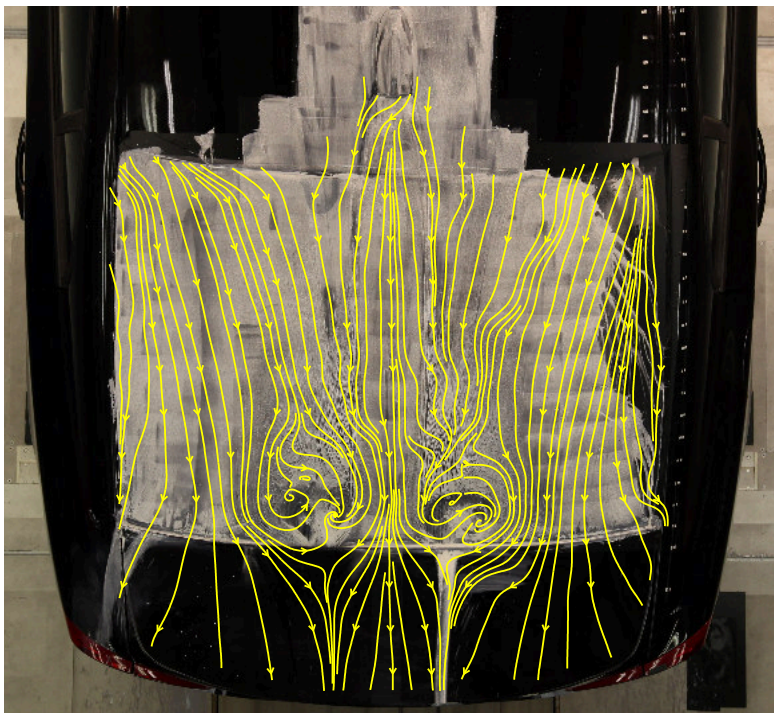

Figure 7.10: *Limiting streamline pattern over the rear window, calculated using the tuft visualisation method*

convergence lines seem to emanate from a saddle point closing the two foci structures left and right of the centreline. Paint dropping over the trunk edge confirms this development.

Small differences can be found downstream of the antenna. Directly behind the antenna base the tuft pattern shows a left shift of the flow. This is triggered by one tuft. It was intended to locate one tuft in the centreline, however it seems that it was located slightly off the centreline, which led to an overall orientation to the left. As there was no other tuft placed in this area the averaged pattern is biased by this effect. Critical points not captured by the tufts are the saddle points in the stagnation area at the lower window edge. This is caused by the coarse grid of the tuft distribution and the fact that the tufts do not take the interruption due to the trunk edge into account.

According to the mapping done by Sims-Williams et al. [58], the S60 with its rear end angle and notch depth, would fall into the group of reattaching asymmetric flow patterns, but lying very close to the symmetric border. The flow topology shows a symmetric pattern, which is expected for fastback geometries as the DrivAer. Although the used Volvo geometry falls into a notchback shape, its curvature and trunk depth are very close to the one of a fastback geometry, which can explain the observation of a symmetric pattern.

7.2.3 Surface properties

As it was done already for the antenna, the surface properties over the rear window are analysed and potential correlations between the topology and surface properties are discussed. Figure 7.11 shows the wall shear stress pattern over the rear window, with the surface coloured by the wall shear stress magnitude. Along the bifurcation lines emanating from N_1 a low wall shear stress can be observed, reaching all the way to S_2. Likewise, negative bifurcation lines can be found over the trunk, along which the wall shear stress shows low values. In the area of singular points the wall shear stress is also low and has to reach zero. The same observation was also made for the flow around the antenna. As the singular points are located very close to each other and the wall shear stress magnitude is lower, compared to the area around the antenna, it is not possible to identify their position only by looking at the wall shear stress distribution.

Figure 7.12 shows the pressure distribution over the rear window. The area is characterized by an overall pressure recovery. Neither the bifurcation lines nor the singular points can be connected to characteristic pattern in the pressure distribution. Merely the saddle points in the stagnation areas at the lower window edge, are identifiable as high pressure spots.

Comparing the pressure distribution calculated by CFD with the experimental distribution shown in Figure 7.13 shows a qualitatively good agreement. The pressure measurements were taken only on the right hand side and its distribution is mirrored. The black

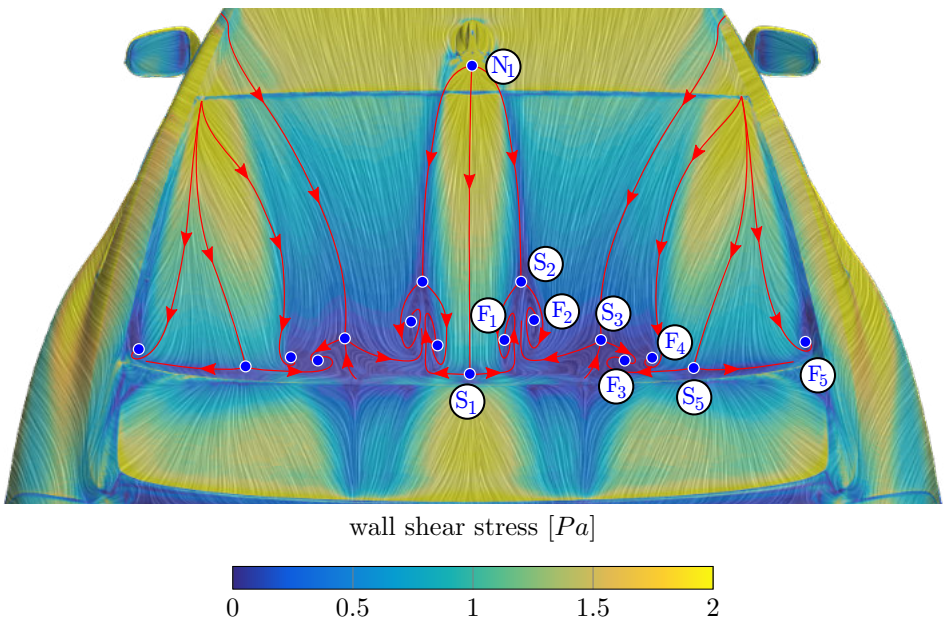

Figure 7.11: *Limiting streamline pattern over the rear window; surface coloured by wall shear stress magnitude*

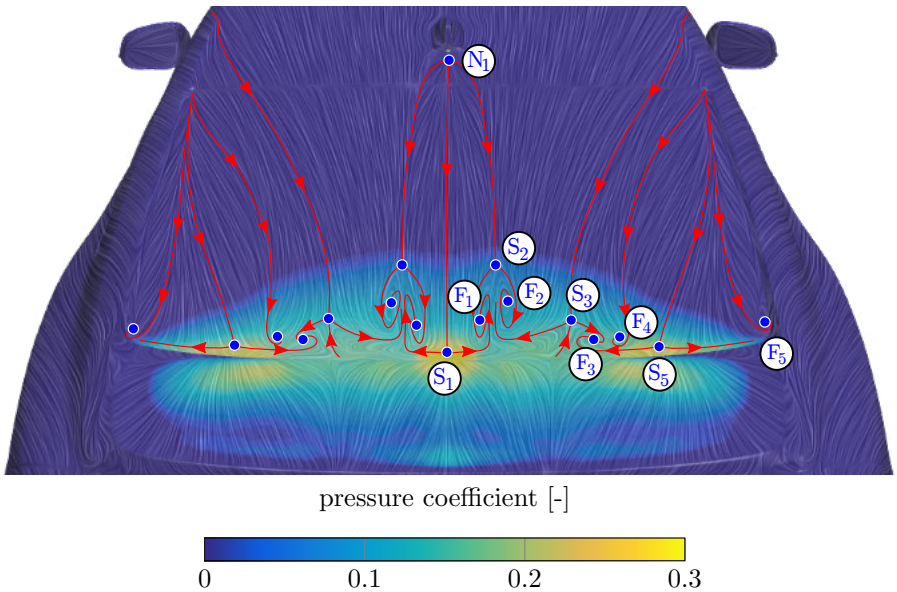

Figure 7.12: *Limiting streamline pattern over the rear window; surface coloured by pressure coefficient*

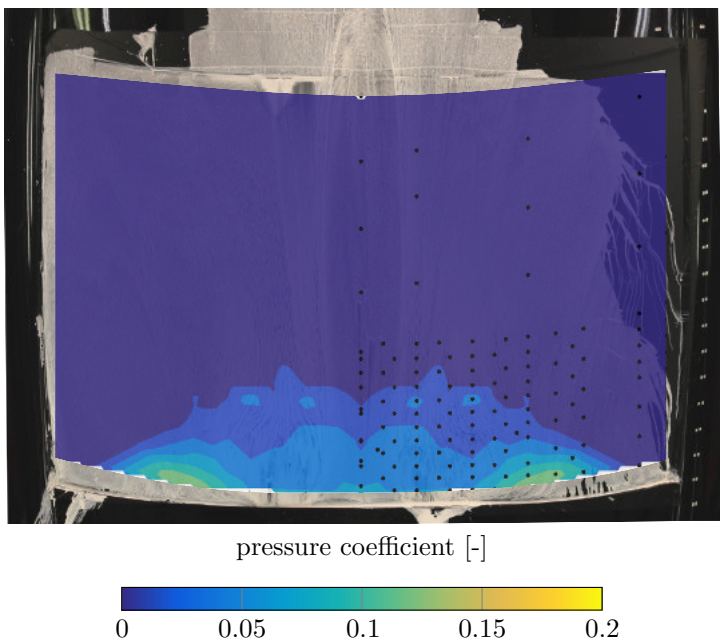

Figure 7.13: *Surface pressure distribution over the rear window; experimental result*

dots show the location of the measurement points, however, due to the rear window curvature distortion effects have to be considered. The pressure spots observed at the lower window edge show lower pressure values compared to CFD. However, as it was already hypothesized in the comparison of the limiting streamline pattern, the pressure distributions also lead to the conclusion that the stagnation at lower rear window is higher in CFD compared to the experiment.

For the flow over the rear window the x component is shown in Figure 7.14 and the distribution shows several changes in the sign of x-vorticity. The node point N_1 was already mentioned in connection the the flow behind the antenna. From this point two limiting streamlines emanate which end in the top saddle points of the rear window foci. Across these lines also the x-vorticity changes sign, as it does across the centreline. As the vorticity changes its sign abruptly, it also means that a bifurcation line occurs. Along the edge, where the window connects to the C-pillar a distinct jump can be observed as well, followed by another switch across the positive bifurcation line starting at the upper window corners. Further in the area where the foci occur, the x-vorticity changes significantly. In general it can be said that in all areas where the switch in x-vorticity occurs together with a negative bifurcation line, a vortex development can be expected. The y and z components are not shown here, as they do not give any further insight.

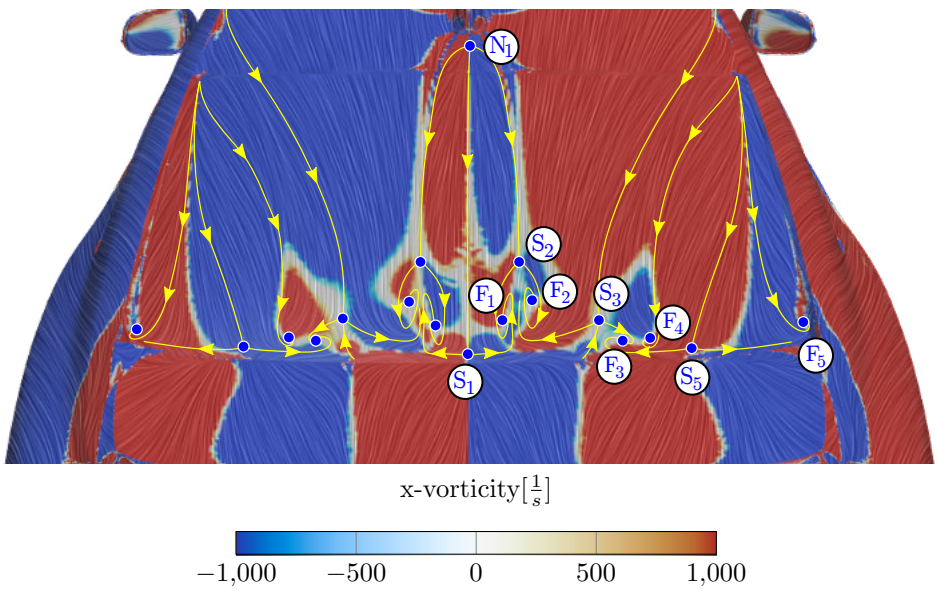

Figure 7.14: *Limiting streamline pattern over the rear window; surface coloured by x-vorticity*

7.2.4 Unsteady aspects of the near wall flow over the rear window

To investigate the unsteady behaviour of the flow over the rear window, the visualisation method as described in section 5.5 is used. A detailed description of the setup used to obtain the following results can also be found in [6].

As the tuft pattern was obtained by averaging a series of snapshots, this method allows to get some insight into the unsteady behaviour in the investigated area. From the tuft movement an orientation angle can be determined in each snapshot. The standard deviation of the tuft orientation angle measures how much each single tuft deviates from the (local) mean flow direction and can be shown in the distribution of the standard deviation as presented in Figure 7.15. The colour range shows deviations between 0° and 80°. The overall flow over the rear window is attached without significant fluctuations.

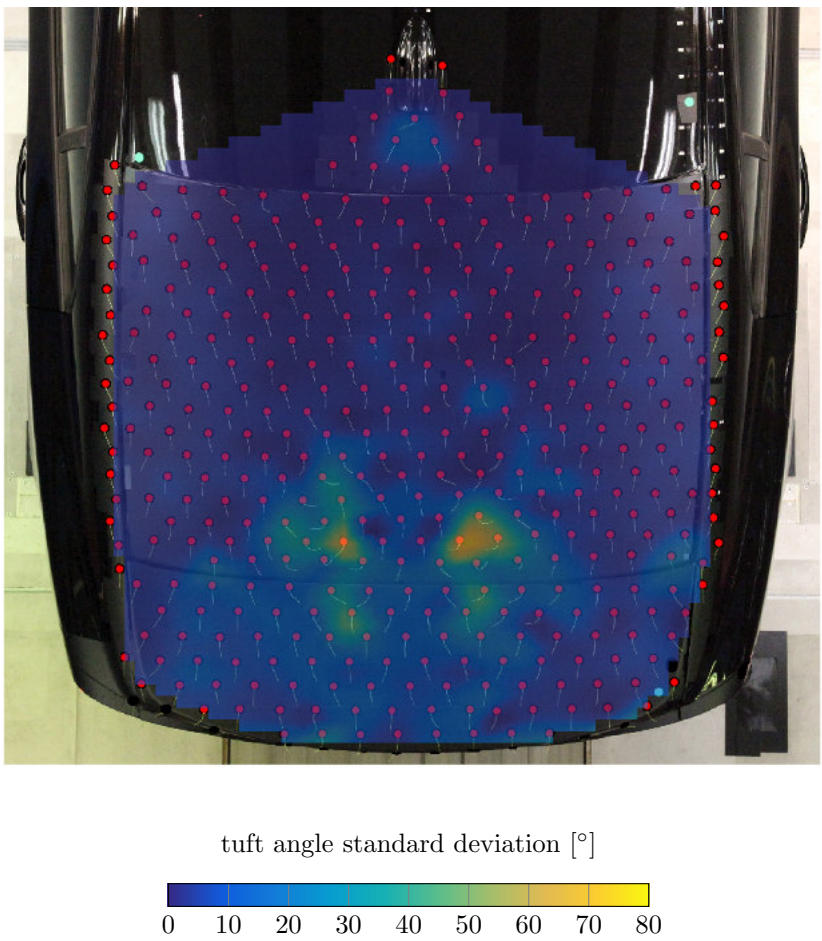

Figure 7.15: *Standard deviation of the tuft orientation*

Only where the foci structures are observed, a higher level of fluctuations is observed. This must be due to separations in these areas. Over the trunk the flow seems to reattach, resulting in weak fluctuations on the boot lid.

Looking back to Figure 8.8, the crossplanes showed vortices emanating from the foci structures next to the centreline, as well as two C-pillar vortices created at the lower window side edges and the A-pillar vortices. The tuft standard deviation shows only evidence of the foci structures next to the centreline. Fluctuations due to the A-pillar vortices cannot be observed. However especially in the upper window area they lie close to the surface, hence it is expected to see possible occurring fluctuations. As this is not the case, it is assumed that the A-pillar vortex forms a stable structure, most probably stabilized by the bulk flow over and around the car.

7.3 Surface flow pattern along the A-pillar

The investigated area can be seen in Figure 7.16a. The A-pillar as an inclined edge is a potential area for a longitudinal vortex development. Like in the previous sections, a short review on generic A-pillar flows is given, before the topology and the surface properties are investigated.

7.3.1 Review on generic A-pillar flows

The aerodynamic design of A-pillars was already of interest in a work by Janssen & Hucho from 1974 [59]. They discussed its design aspects regarding their contribution to drag, noise and contamination. All the attributes aim for an attached flow in order to reduce drag, the noise level and the amount of side window contamination. More detailed investigations of the created vortex along a generic A-pillar model were done by [60–64]. Laser Doppler Velocimetry (LDV), Particle Image Velocimetry (PIV) and unsteady pressure measurements were used to analyse the dynamics and topology, as well as its interaction with the side wall. The generic models used had sharp edges, also along the inclined edges.

It was found that a primary and a secondary vortex were created along the inclined model edge, with counter rotating sense of rotation. Levy & Brancher [62] explain that the primary vortex is created as the flow folds around the A-pillar edge. The created vortex is pushed to the side wall due to free stream flow passing by the sides. As a result, a pressure gradient is generated by this vortex, which causes the creation of the secondary vortex, as the wall boundary layer separates. The occurrence of the primary and secondary vortex was also visualized in experiments carried out by Howel et al. [61].

In a later work Levy & Brancher [63] also investigated the vortex circulation and size. It was found that the circulation of the primary vortex increases along the A-pillar edge, while the circulation of the secondary vortex does not change significantly. This increase in circulation occurs, although the vorticity maximum decreases. Further it was observed

that the centre of the primary vortex moved away from the wall as it developed along the A-pillar, while the secondary one remained close to the side wall. The influence of geometry was also investigated using a second model, where the sharp A-pillar edge was rounded with a radius of 40 mm. It was found that the new topology differed completely from the initial one, as no dominant vortex structure could be found. Instead, the dynamics were similar to the ones of a shear layer, subjected to a Kelvin-Helmholtz instabilities.

7.3.2 Flow topology

CFS is characterized by converging streamlines towards a common line [33, 36, 37]. These do not start from singular points, which makes it difficult to define their origin based on the limiting streamline pattern. Over the exterior of a passenger car, several potential regions for CFS can be identified as could be seen in the previous sections. The most obvious one is found on the A-pillar. Figure 7.16 shows its surface pattern and an enlargement of the A-pillar region.

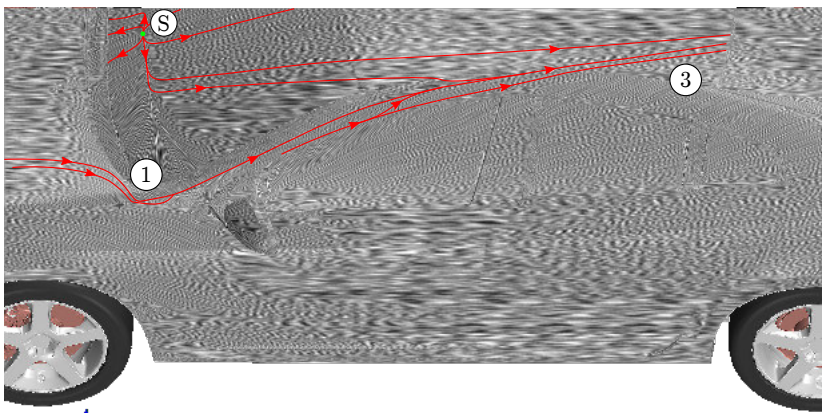

(a)

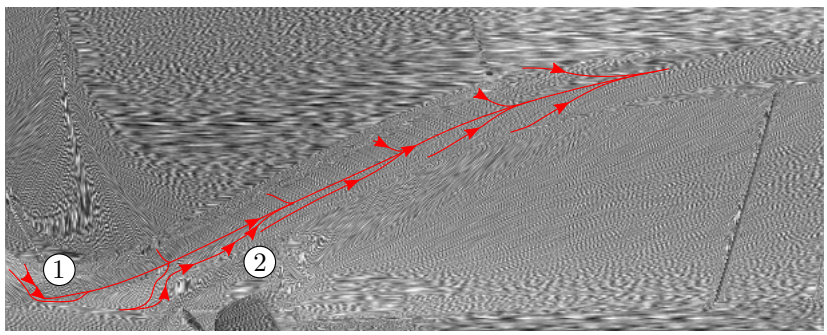

(b)

Figure 7.16: *Limiting streamline pattern along the A-pillar*

In region ① the wall shear stress lines start to converge towards a common line. The shown limiting streamlines result from flow over the hood which changes its direction almost 90° to follow the A-post. Along the entire A-pillar a negative bifurcation line can be detected towards which the limiting streamlines converge. Reaching the roof of the car, the convergence radius increases until the limiting streamlines do not indicate any longer a crossflow separation, as seen in region ③. The flow in this area emanates from the windscreen stagnation point Ⓢ (saddle point) and from the flow around the side of the car. On the A-pillar itself no singular points occur.

7.3.3 Surface properties

The A-pillar region and its surface pattern, coloured by wall shear stress magnitude is shown in Figure 7.17. The distribution shows the development of a significant gradient in wall shear stress along the bifurcation line, starting around ②. Contrary to previous observations, the bifurcation line does not lie in a low wall shear stress valley. Along the A-pillar the wall shear stress drops rapidly from high to low along the bifurcation line.

The pressure distribution is shown in Figure 7.18. In the middle A-pillar region the pressure is low compared to the surrounding regions. However it is difficult to connected the pressure distribution clearly to the start of the bifurcation line. In region ① the pressure gradients are very weak and it is hard to determine where the limiting streamlines start to converge. Passing by region ② the pressure decreases and it can be adumbrated that the pressure gradients marks the location of the bifurcation line. Reaching the car roof the pressure increases again and gradients across the bifurcation line cannot be detected.

As a longitudinal vortex development is expected, the x-component of the surface vorticity

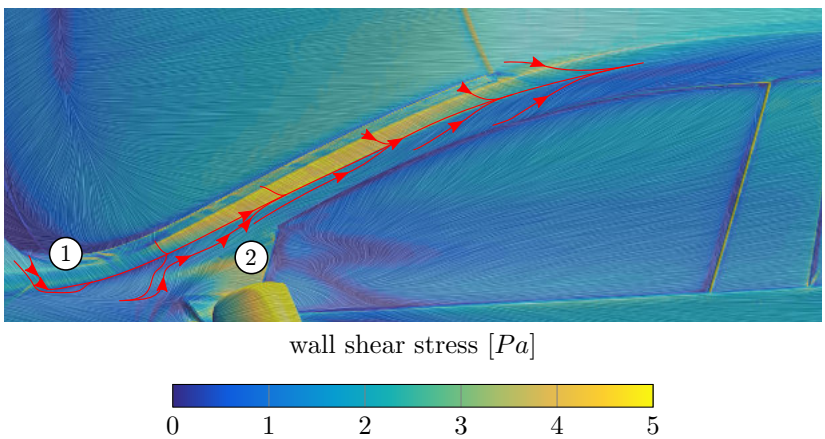

Figure 7.17: *Limiting streamline pattern along the A-pillar; surface coloured by wall shear stress magnitude*

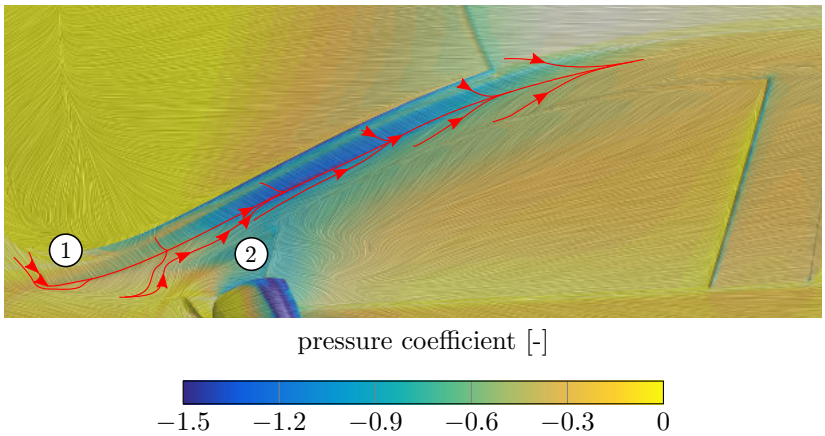

Figure 7.18: *Limiting streamline pattern along the A-pillar; surface coloured by pressure coefficient*

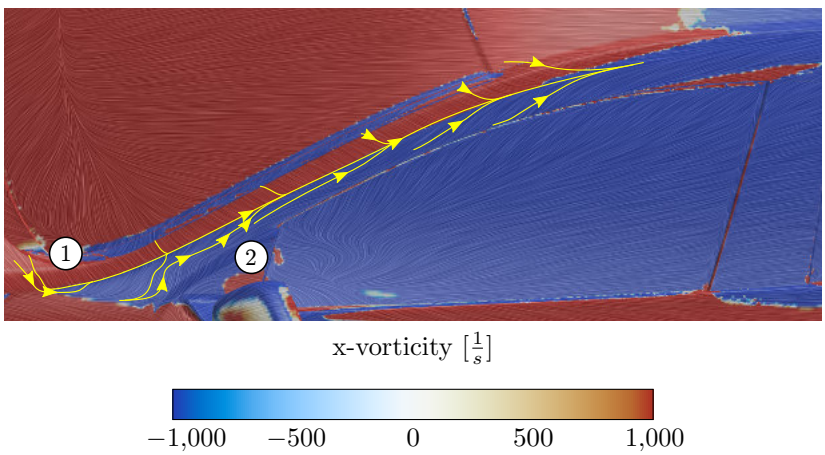

Figure 7.19: *Limiting streamline pattern along the A-pillar; surface coloured by x-vorticity*

is shown in Figure 7.19. The blue areas correspond to negative and the red ones to positive values. The x-vorticity distribution shows that across the convergence line the x-vorticity changes its sign with a very steep gradient. This quick change can be explained, looking at the vorticity lines and the wall shear stress lines as done by Wu [37] (see also section 4.3.5) and as it was explained for the flow behind the antenna (see also Figure 9.11a). Due to the steep gradient in x-vorticity the beginning of the limiting streamline convergence can be estimated more precisely compared to the wall shear stress or the pressure distribution. All along the bifurcation line a clear change in sign can be observed. The x-vorticity is therefore the most precise parameter to visualize the limiting streamlines convergence in longitudinal direction.

Apart from the bifurcation line along the A-pillar, Figure 7.19 shows distinct changes of

x-vorticity between the front screen and the A-pillar, which also include the development of bifurcation lines. In this area a further separation has to occur. However, this is not developing into a large scale structure and is therefore not investigated in more detail.

7.4 Surface flow downstream of the front wheelhouse

Moving to a fourth region, the flow downstream of the front wheelhouse is investigated. In this region the flow is characterized by many different interactions due to the wheel rotation and its created wheel wake, as well as the interaction with the vehicle exterior.

7.4.1 Flow topology

The limiting streamline pattern obtained from CFD and experiment is shown in Figure 7.20. The experimental pattern is obtained by the tuft method. The usage of paint causes a high level of contamination, which could damage the moving ground system; therefore the method described in Section 5.5 is used.

In CFD (Figure 7.20a) the pattern shows a saddle point, which is closing two recirculation areas. The upper one creates the focus point F_1. For the lower one, no focus point can be found on the surface, though the limiting streamlines show a recirculation. It seems that the source of this focus lies on the wheelhouse edge. The overall flow direction shows a slight down-wash, which seems to be stronger below the separatrix line. Further downstream of the wheel arch, the limiting streamlines are redirected horizontally which corresponds to the undisturbed flow direction.

The pattern obtained from experiments (Figure 7.20b) looks different compared to CFD. First of all it attracts attention that there is no recirculation observed nor the development of a focus. However it seems that the flow was about to create a recirculation as it was predicted by CFD. Along the upper wheelhouse edge a strong down-bend can be seen, which changes direction almost 90°. It seems that the expected saddle point as it was observed in CFD is located at the edge of the wheel arch. Hence it seems that the predicted CFD pattern is shifted upstream in the experimental results. The overall flow direction shows a down-wash, similarly as in CFD, with a redirection to a horizontal flow further downstream. The main changes in the observed pattern is attributed to the highly unsteady effects in this area and the wheel rotation, which are most probably not well predicted with the chosen steady state and MRF approach.

However, both pattern indicate a strong down-wash of the near wall flow along the upper wheel arch edge and the realignment with the undisturbed flow direction downstream of the wheelhouse. Although the two topological patterns show differences, both indicate a separation along the wheelhouse edge. CFD indicates a separation from the recirculation area closed by the saddle point S. From the experiment separation along the edge is expected. This conclusion is based on the observation that the limiting streamline pattern does not show any characteristic singular points, nor a convergence line where the flow

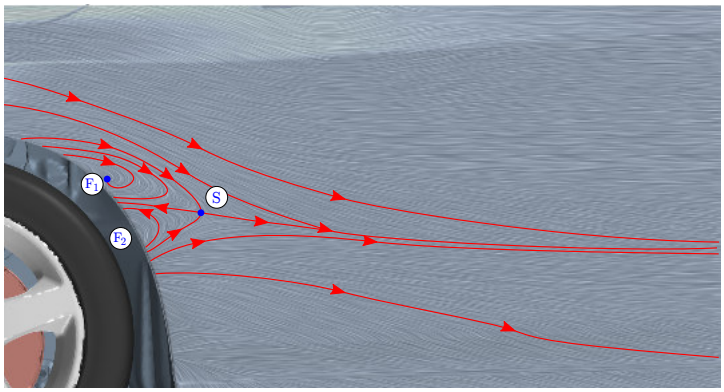

(a) *CFD*

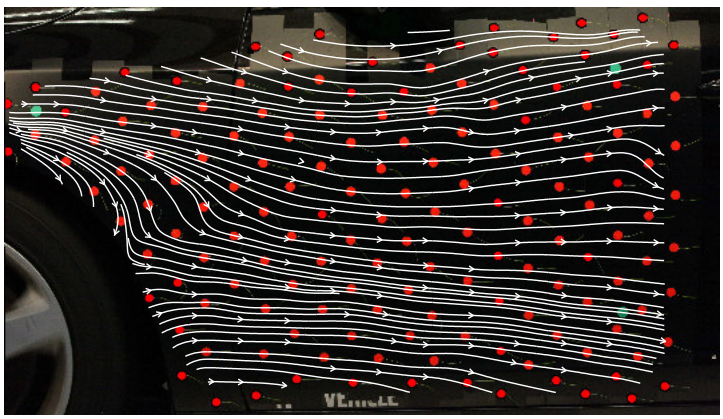

(b) *experiment*

Figure 7.20: *Limiting streamline pattern downstream of the front left wheel*

could leave the surface. Along the lower wheelhouse edge neither of the two methods show a characteristic separation pattern. It is though assumed that flow separates at the edge of the wheelhouse.

7.4.2 Surface properties

Figure 7.21 shows the measured and calculated surface pressure distribution on the side of the vehicle, downstream of the front left wheelhouse. For the numerical result, the area is highlighted in which the pressure sensors are distributed for the experimental setup. The measurements in Figure 7.21a, show that a lower pressure is observed around the wheelhouse edge compared to the region further downstream. This low pressure region is created due to the separated flow. The lower pressure in the upper region results in a suction which causes the limiting streamlines to bend down. Further downstream

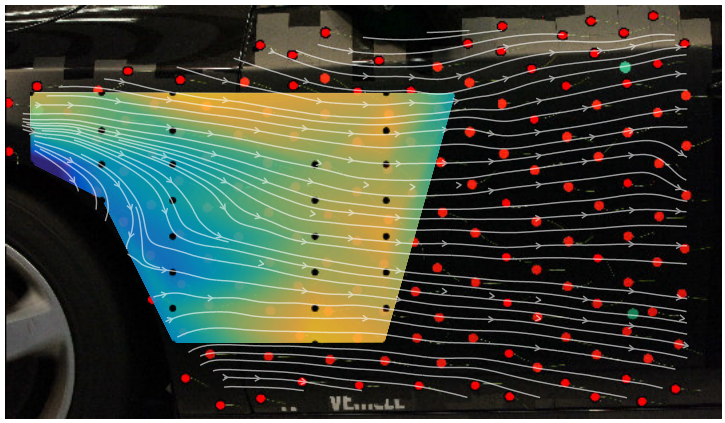

(a) *experiment*

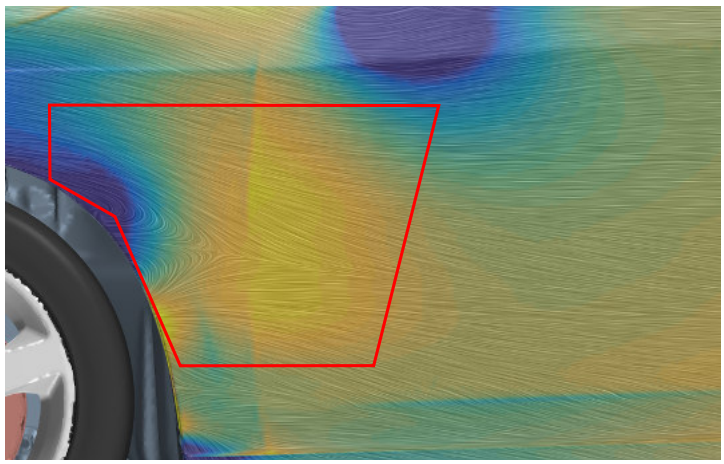

(b) *CFD*

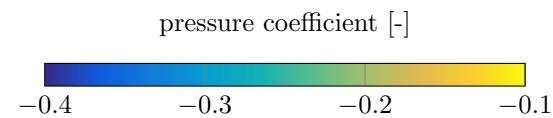

Figure 7.21: *Experimental and numerical limiting streamline pattern downstream of the front wheelhouse; surface coloured by surface pressure*

the pressure force decreases and its influence becomes weaker, until the viscous forces dragging the flow downstream dominate.

The numerical results shows significant differences compared to the experiment. Although a low pressure is created along the upper wheel arch region, further down at the edge a high pressure spot is observed (below the lower recirculation). This is mainly attributed

to the simulation method, using the steady-state MRF approach. The spoke position in this method is not rotating, which can cause significant differences in the resulting flow development.

The area downstream of the front wheel arch showed significant differences in the results, which are assumed to be caused by the chosen simulation method. Although the method showed very good agreements in the previous sections, it is problematic to analyse regions characterized by high unsteadiness and wheel rotation interactions.

7.4.3 Unsteady aspects of the near wall flow behind the front wheel arch

Another interesting region is the area downstream of the wheels. In this investigation the flow downstream of the front left wheel is analysed. The flow in this region is determined by the wheel wake flow and its interaction with the flow around the vehicle as well as the underbody flow. For the investigation the tuft method and unsteady surface pressure measurements were used.

Results from the tuft method

The time averaged limiting streamline pattern was already shown in Section 7.4, Figure 7.20b. The standard deviation of the tuft angles is shown in Figure 7.22.

The tuft angle standard deviation shows high fluctuations around tuft A. On the upper

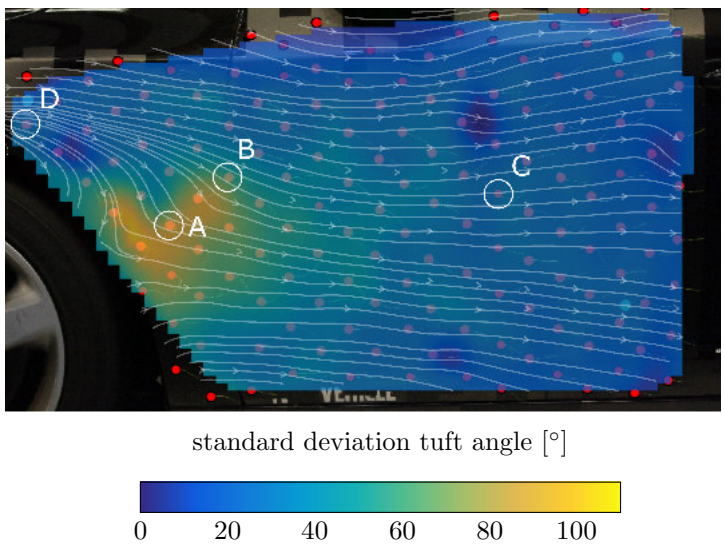

Figure 7.22: *Distribution of the standard deviation of the tuft angle*

wheelhouse edge, where tuft C is located the fluctuations are very small, but still present; similar to the downstream region where also tuft D is located. However, it shall be noted that the whole area of investigation shows tuft fluctuations. Contrary to the flow over the rear window, the tufts are constantly moving along the whole side. This observation is surprising as it was expected to observe a separation region along the wheelhouse edge and slightly downstream of the wheelhouse, followed by an attached flow with a mean flow direction parallel to the undisturbed flow.

The area of large tuft movements is located where the limiting streamlines coming from the upper wheelhouse show a strong bend and change their direction. It is assumed that in this area different flow effects interact, which cause the high tuft angle standard deviations. The flow in the upper part is coming over the hood and from the upper wheelhouse edge. The strong down-bend indicates a force acting on the limiting streamlines, which causes a change in direction. It is expected that along the wheelhouse an edge separation occurs which is overlaid by the wake created due to the wheel rotation. The distribution of the tuft angle standard deviation indicates that flow with two different directions meet in the area around tuft A, resulting in the large deviations.

Results from the time resolved surface pressure measurements

To increase the insight into the unsteadiness in this region, time resolved pressure measurements are taken. The grid of the measurement locations is shown in Figure 7.23. Similar to the tuft movements, it is possible to calculate the standard deviation of the surface pressure coefficient. The distribution is shown in Figure 7.24. Compared to the tuft angle standard deviation, the areas of high fluctuations are located differently. From the upper wheelhouse a region of high fluctuations extends downstream in the shape of a spike. Also around the lower wheelhouse edge an increased fluctuation level can be observed.

Areas with high pressure fluctuations on the surface indicate the location of separation

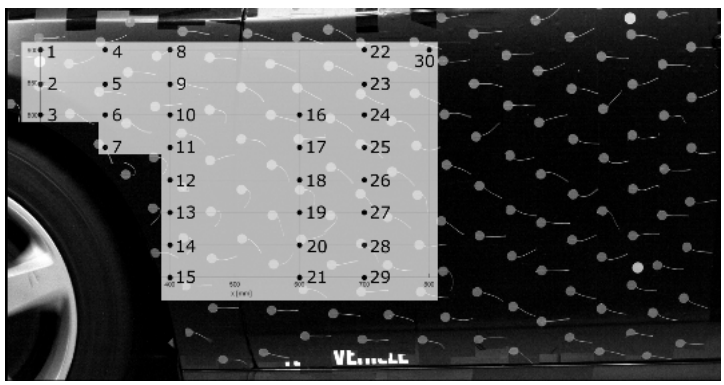

Figure 7.23: *Pressure sensor distribution and identification downstream of the front wheel*

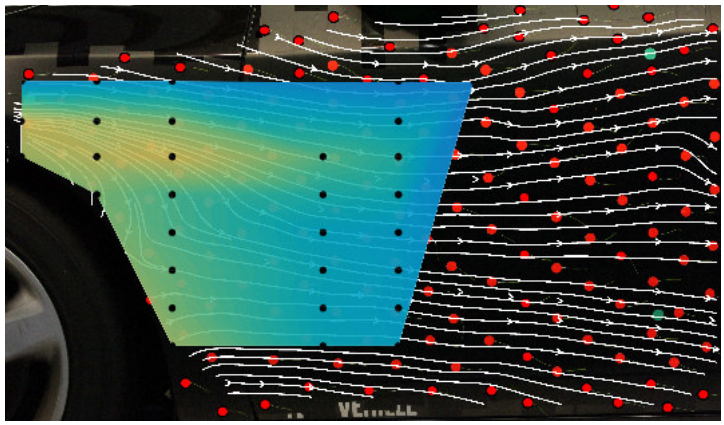

Figure 7.24: *Distribution of the standard deviation of the pressure coefficient*

and/or reattachment zones. For the observed flow situation it can be concluded that a flow structure develops from the upper wheelhouse edge. This structure impinges the vehicle surface in the area where the high pressure fluctuations are observed. The fluctuations along the lower wheelhouse edge are attributed to the reattachment of the flow separating at the wheelhouse edge.

To identify coherent structures and to be able to estimate their propagation direction and velocity, the cross correlations between individual pressure signals are analysed. Figure 7.25 shows the cross correlation matrix respective sensor S2 and sensor S15.

In general it can be seen that the signals of the upper sensors are correlated with each other as well as the signals of the lower sensors. This division shows that two different flow events are observed. One which takes place in the upper half and one which occurs at lower part. From Figure 7.25a it can also be seen that the highest correlations occur in downstream direction, which means that the propagation of the observed phenomena is in downstream direction, corresponding to the main flow direction. Looking at the specific signals between S6 and S11 (presented in Figure 7.26) shows that the signals correlate. This shows that the propagation of the phenomena is not only in horizontal direction, but also with a slight down wash. This flow propagation is also indicated by the path of the limiting streamlines. Additionally, the signal between S6 and S10 is shown which shows the highest correlation and propagation in main flow direction as well as the correlation signal between S6 and S12. The latter shows that the two signals do not correlate, which means that they do not have similarities. This was also indicated by the correlation coefficient distribution in Figure 7.25. Based on the time delay of the correlation maximum, a propagation speed of approximately 17 m/s can be estimated (cf. undisturbed velocity u_∞ =27.78 m/s). Looking back to Figure 7.22 it can be seen that

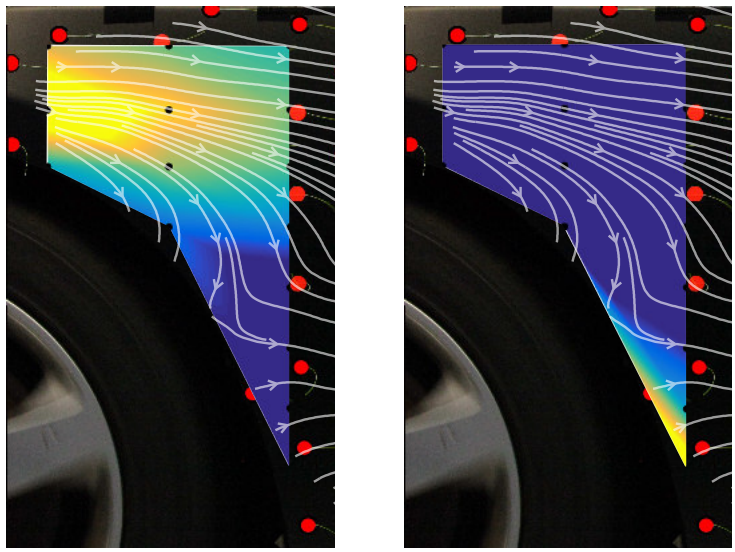

(a) *correlation respective sensor S2* (b) *correlation respective sensor S15*

Figure 7.25: *Cross correlation matrix respective sensor S2 and sensor S15*

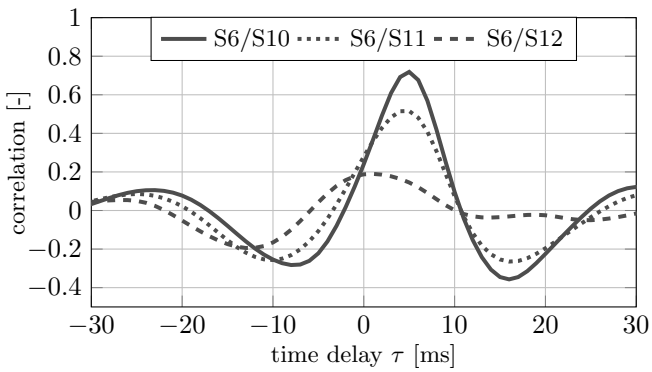

Figure 7.26: *Cross correlation between sensor S6/S10, S6/S11 and S6/S12*

the high tuft angle standard deviations occur exactly, where the cross correlation signals indicate the merge of the two observed flow phenomena. This is understandable, since in this area the two different flow events interact, causing disturbances in the flow directions of the near wall flow.

7.5 Surface flow on the vehicle base

As a last area the pattern on the vehicle base shall be analysed. As behind the base, the vehicle wake is created, which determines the base contamination and has an important contribution to the overall drag, it is of interest to understand how the different structures created upstream merge with those created downstream of the base.

7.5.1 Review on wake flow structures behind passenger vehicles

Famous cited works on the wake structure of vehicles are the studies performed by Ahmed [65–67]. In his works the wake flows behind the typical vehicle rear end shapes, notchback, estate and fastback, are studied. Behind the vehicle base, a recirculation zone is created, similar to the one presented in Figure 7.27, where the 2D streamlines in the symmetry plane are shown. In the pattern, two foci structures can be identified. These rotate in opposite directions and build the recirculation zone, which is closed by a saddle point.

Further, the literature reports the observation of large vortex structures, similar to the trailing vortices of wings, that dominate the picture in crossplanes through the far wake. In the work of Ahmed [66] three different generic vehicle models were investigated; a notchback, a fastback and an estate model. It was found that the notchback and fastback shape create two counter rotating trailing vortices with an down-wash in the centreline. For the estate model, two counter rotating trailing vortices with a up-wash in the centreline were found. These flow situations are is also described in [23]. The reason of the different sense of rotation for the estate model is attributed to the A-pillar vortex flow which is stated to be dominating, while for the fastback and notchback the development of the trailing vortices are attributed to the C-pillar vortices development. Similar results are also found for the wake of an Ahmed body (for instance [68]) and also realistic passenger cars show these trailing vortices e.g. [7, 8, 69]. Mostly, studies attribute the creation of the trailing vortices to inclined edge of the C-pillar. It is postulated, that due to the inclination, a free vortex layer is created, that develops into into the far wake. The surface

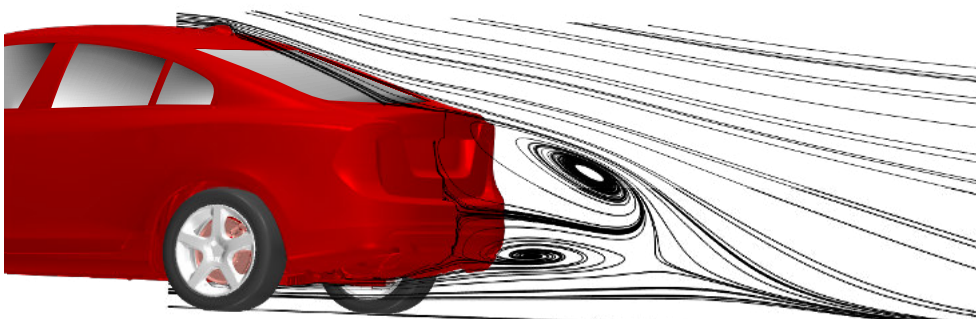

Figure 7.27: *2D streamlines in the symmetry plane through the wake*

flow is mostly investigated in connection with the flow over the rear end as has already been presented in Section 7.2.1.

7.5.2 Flow topology

The surface topology for the vehicle base shows several saddle and node points; these are partly of very small scale and therefore merge together in the large scale view. Figure 7.28 shows a number of saddle and node points along the centreline (N_1, S_1, N_2, S_2 and N_3). All three node points are attachment points, as the flow is directed away. The overall flow direction of the near wall flow is away from the centre. On the left side the two foci F_1 and F_2 are present (respective ones appear also on the right side), which are rotating in opposite direction. As they seem to be created by the near flow emanating at the vehicle base centre it is assumed, that these are created when the flows coming from upstream along the vehicle side and from the vehicle base meet. Another node point N_4 can be found on the upper corner of the vehicle base. As the flow is pointing towards the node, this is a node point of separation. Between F_2 and N_4 a further saddle point occurs. The connecting line between these two points is a negative bifurcation line along which the flow separates. In between the centreline and the described points on the outer edge, some other smaller singular points can be found, which are created by steps and gaps of the base geometry, but are almost not visible in the large scale view.

Figure 7.27 shows the 2D streamlines in the symmetry plane, with the characteristic foci structures. It shows that the flow at the upper trunk edge separates two regions. The flow above the recirculation and the flow in the recirculation area. At the vehicle base, the recirculating flow attaches and creates the attachment points N_1 to N_3. As soon the flow attaches to the base, it is distributed away from the centreline as described above. The near wake can hence be interpreted as a bubble type separation. As the flow over

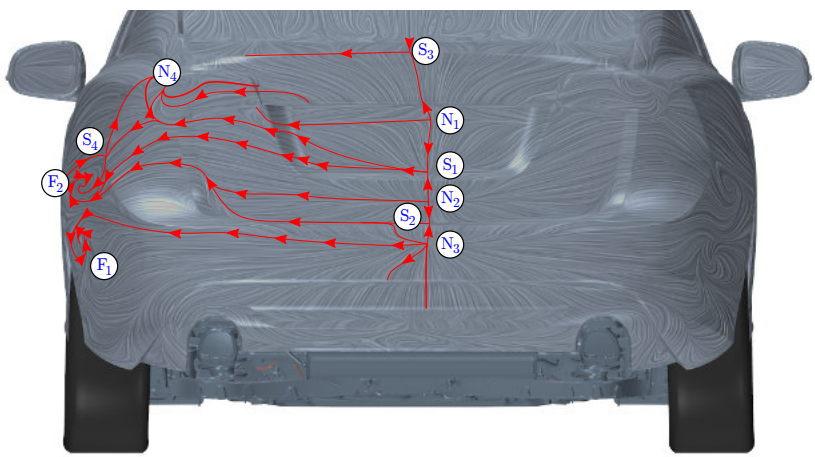

Figure 7.28: *Limiting streamline pattern on the vehicle base*

the trunk is separated from the recirculation region, a separation line in form of a CFS has to occur left and right of the centreline, emanating from saddle point S_3.

7.5.3 Surface properties

The following Figure 7.29 shows the base coloured by wall shear stress magnitude. The wall shear stress is low all over the base area, however around node N_4 a high wall shear stress spot can be observed, which is crossed by a line of low wall shear stress. Along this line the limiting streamlines converge to enter the node N_4. On the sides, the wall shear stress is clearly lower, where the foci pairs are observed, while they are zero in the singular points. This observation was also made for locations of the foci on the rear window.

At the edge between trunk and vehicle base the wall shear stress changes rapidly. This jump occurs exactly along the convergence line, where the flow separates from the surface, creating a separation surface between the recirculation region and the flow over the trunk. Another distinct jump can be observed at the edge between F_2 and N_4. Again, along this edge the limiting streamlines converge and result in a CFS. Figures 7.30b and 7.30c show an enlarged view of the trunk-base edge and the side-base edge. It is shown that along the steep gradients the limiting streamlines converge.

This shows that an edge separation results from a CFS. The separation line is difficult to see from the limiting streamline pattern as the limiting streamlines converge in a very narrow area. However, the wall shear stress magnitude distribution shows a clear

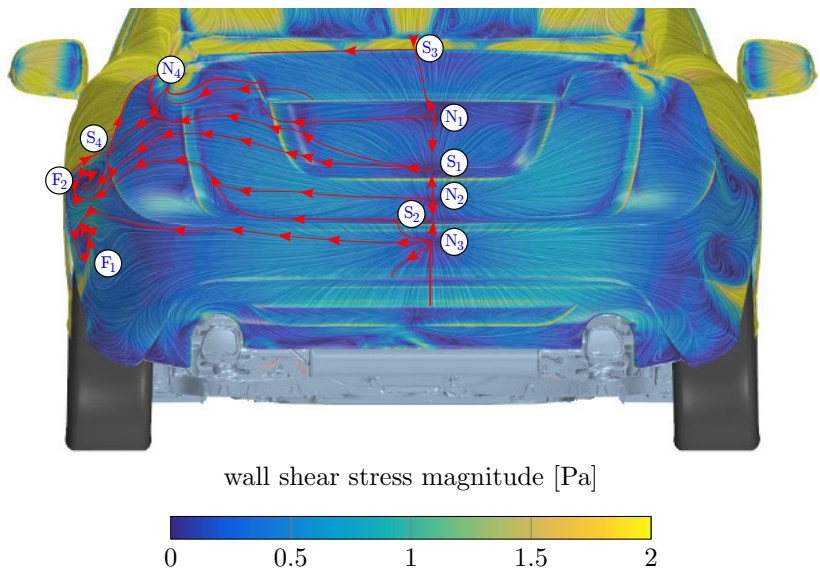

Figure 7.29: *Limiting streamline pattern on the vehicle base; surface coloured by wall shear stress magnitude*

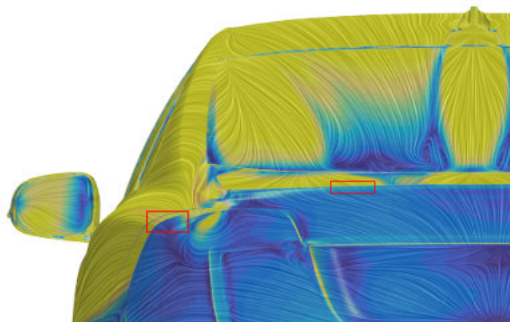

(a) *location on the vehicle base, where the CFS separation is enlarged*

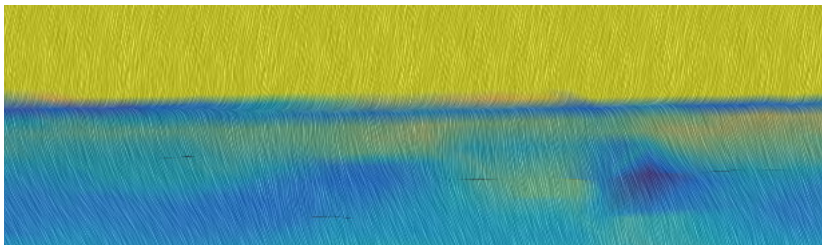

(b) *edge between trunk and base*

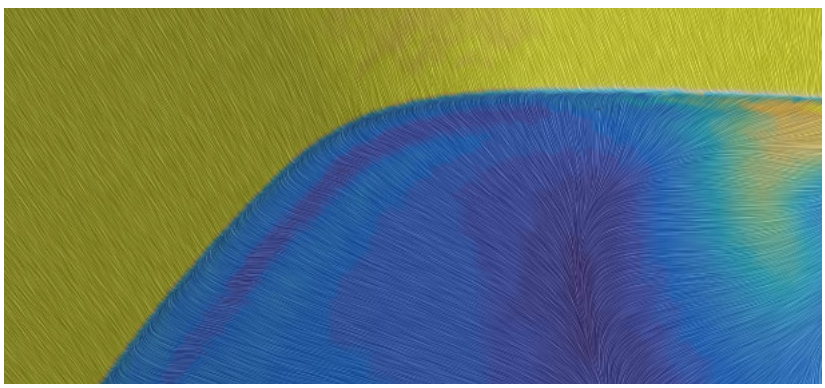

(c) *edge between side and base*

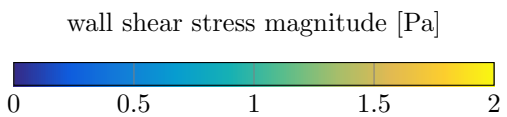

Figure 7.30: *Limiting streamline pattern on the edges between trunk and vehicle base as well as side and vehicle base; surface coloured by wall shear stress magnitude*

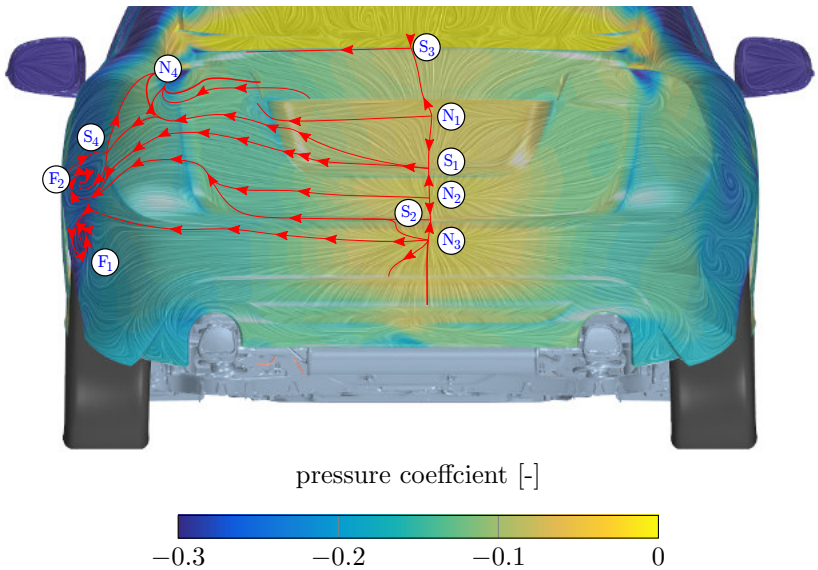

Figure 7.31: *Limiting streamline pattern on the vehicle base; surface coloured by pressure coefficient*

change in magnitude which allows an easier identification. A similar jump can be seen in the vorticity magnitude (not shown here) as the wall shear stress and the vorticity are proportional.

To reduce the vehicles' drag it is desired to have a high pressure all over the vehicle base. The highest pressure is observed in the centre of the base (see Figure 7.31), along the node - saddle connections N_1 to N_3. In this area the flow reattaches, before it distributes over the base surface. Towards the sides the pressure decreases. Significant in Figure 7.31 is the pressure minimum around node N_4, where the flow detaches. Also around the foci pairs, the pressure is lower compared to the centre pressure, however the area shows an overall lower pressure and there are no clear indications that the foci cause a pressure minimum. According to the presented limiting streamline pattern and the surface properties, it can be concluded that the foci on the sides as well as the node point N_4 are the sources for flow leaving the surface. Following the the limiting streamlines and their directions it can be seen, that N_4 swirls in negative (clockwise looking from behind) direction. Hence, it is expected to observe a developing structure, with a negative sense of rotation. F_1 would therefore lead to a positive rotating structure and F_2 in a negative one as well. In the following Chapter 8.5, the flow field behind the base is analysed in more detail.

Chapter 8

Development of Separation Structures into the Flow

The previous chapter described and discussed the limiting streamline pattern of different areas on the car. In the following it shall be discussed how the near wall flow develops into the freestream and which flow structures are created.

8.1 Antenna flow

The surface flow pattern around and downstream of the antenna shows several characteristic features. To investigate which structures develop from the near wall flow, 2D streamlines and the vorticity distribution are studied in different crossplanes. Figure 8.1 shows the perspective view onto a crossplane 100 mm behind the antenna base, where the

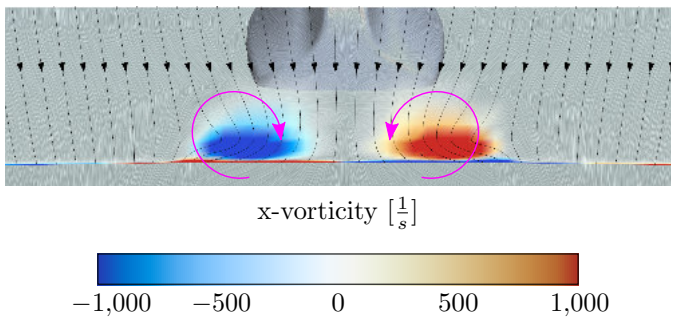

Figure 8.1: *Crossplane* 100 mm *behind the antenna base; coloured by x-vorticity*

plane is coloured by x-vorticity; further the 2D streamlines of velocity are drawn on this plane.

The vorticity distribution shows two spots, indicating two vortices rotating in counter clockwise direction. The 2D streamline pattern however does not show clear foci structures in the area where the vorticity spots are. Further, Figure 7.7 shows a x-vorticity surface pattern behind the antenna, where it was expected to find a vortex with a positive sense of rotation to the left (looking from behind) and a vortex with a negative sense of rotation to the right (looking from behind). However, Figure 8.1 gives exactly the opposite. A closer look at Figure 8.1 shows that below the vorticity spots a thin layer with the opposite x-vorticity is created. From the limiting streamline pattern it was expected to find vorticity leaving the surface along the observed convergence line. To understand this development, further crossplanes are studied; starting 20 mm upstream the antenna base.

Figure 8.2a shows that the overall flow direction has a down wash and slight in wash (pointing towards the centreline). Additionally two vorticity spots are found on the antenna back. These are growing and moving further downstream, as can be seen in Figure 8.2b and 8.2c. It can be assumed that the observed spots are part of two small vortices created at the inclined edge of the antenna rear end. Overall these have a large transverse component rotating around the z axis. An indication of such vortices is already given, looking at the limiting streamline pattern in Figure 7.8. Looking into a plane, 1 mm behind the defined antenna base (Figure 8.2c) also two foci start to appear. These emanate from the node point N_2 and its respective symmetric correspondent (see Figure 7.4c). The surface x-vorticity in N_2 is negative; hence the focus developing from N_2 has also a negative sense of rotation. Within the downstream 4 mm, the foci structures in the 2D streamlines grow in diameter (Figure 8.2d). Further it can be seen that the vortices created on the antenna back start to merge with the antenna base vortices, resulting in a L-shape distribution of x-vorticity. Figure 8.2e shows that next to the primary focus a second focus is created, which disappears again before reaching the $x = 15$ mm plane (Figure 8.2f). Moving further downstream (Figure 8.2h) the x-vorticity distribution continues showing the antenna base vortices, however, the 2D streamlines indicate that they dissipate. The traces from the transverse vortices identified in the upstream planes, become weaker 15 mm behind the antenna base and are barely present in the most downstream plane (Figure 8.2h).

The most surprising observation is the fact, that the sense of rotation of the antenna base vortices does not match the x-vorticity distribution on the surface. Previously it was explained that the antenna vortices are created by a node point of separation from the antenna base; however, the limiting streamline pattern lead to the conclusion that a crossflow separation is created. A closer look into Figure 8.2 shows that both phenomena occur. In Figure 8.2d to 8.2h it can be seen that underneath the created base vortices a thin layer x-vorticity with contrary sign is built. To the left and right of these layers, the boundary layer vorticity changes sign again. The layers underneath the base vortices tend to distribute away from the centreline. As the layers hit the the boundary layers with contrary x-vorticity, small ears are created, which show the attempt of the vorticity to separate from the surface. However, the antenna base vortices are growing and seem

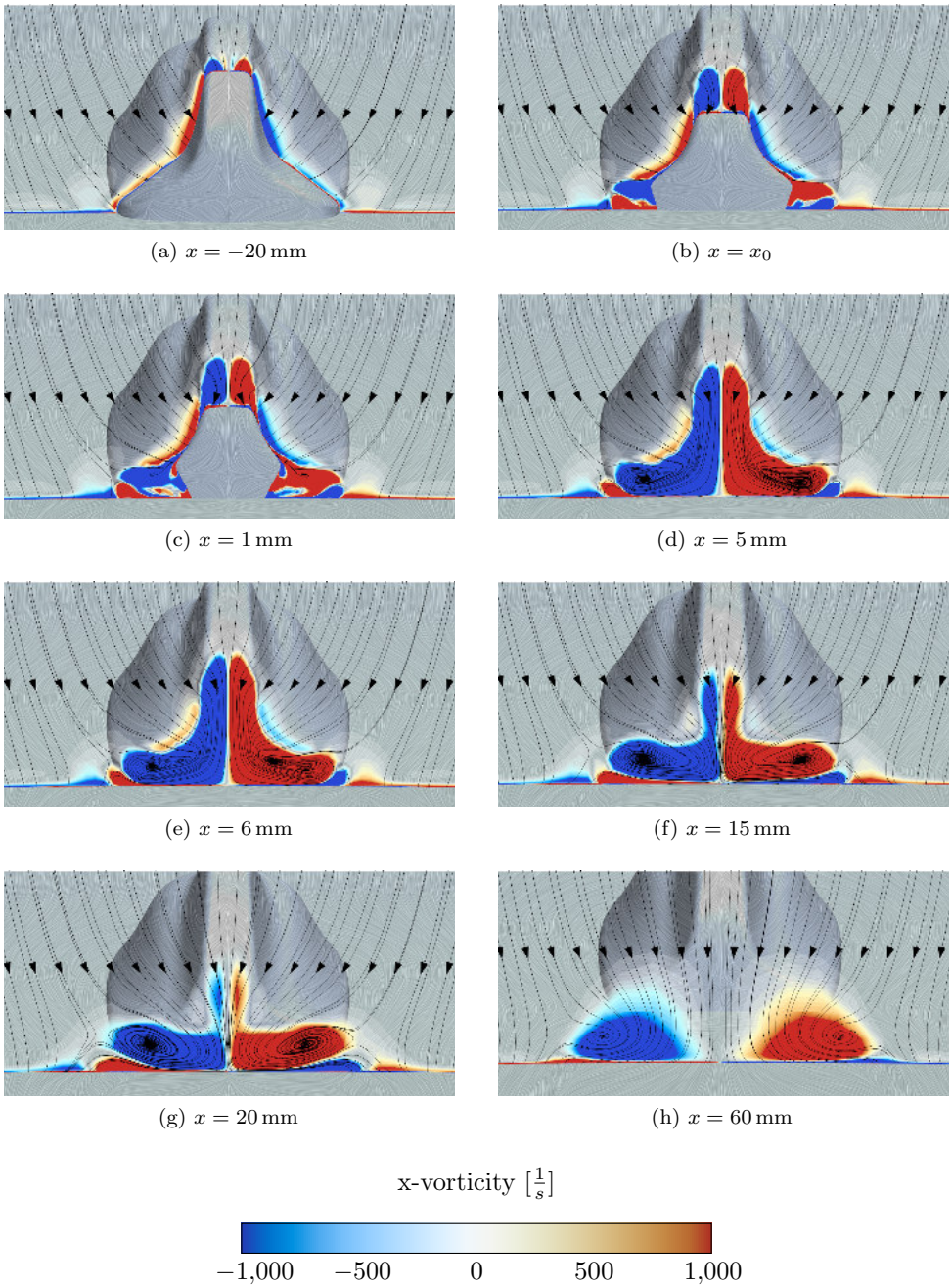

(a) $x = -20\,\text{mm}$ (b) $x = x_0$

(c) $x = 1\,\text{mm}$ (d) $x = 5\,\text{mm}$

(e) $x = 6\,\text{mm}$ (f) $x = 15\,\text{mm}$

(g) $x = 20\,\text{mm}$ (h) $x = 60\,\text{mm}$

Figure 8.2: *Crossplanes downstream of the antenna base; coloured by x-vorticity*

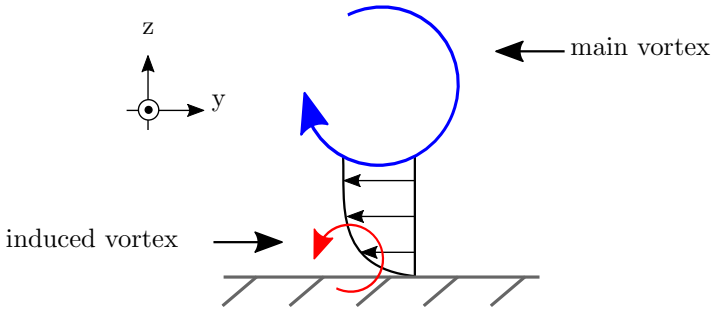

Figure 8.3: *Schematic, explaining the development of induced vorticity*

to suppress this crossflow separation, by rolling out the x-vorticity ears.

Remaining questions are, how these two phenomena are connected and why the observed boundary layer vorticity is created underneath the antenna base vortices. To explain this observation, Figure 8.3 sketches the situation. The main vortex is rotating in clockwise direction. At its lower edge, the transverse velocity points to the left. Due to the close proximity to the wall and the no-slip condition at the wall, a boundary layer is built. This boundary layer results in induced vorticity at the wall, rotating in counter clockwise direction, and in the observed vorticity layer of contrary sign underneath the antenna base vortices. It can be said, that the surface vorticity is a reaction onto the created antenna base vortices.

To visualise the 3D structure of the observed vortices, Figure 8.4 shows the Q isosurface (Q=500000) coloured by vorticity magnitude. The high Q value is chosen to isolate the structures of the transverse and longitudinal vortices. Along the antenna back edges two transverse vortices are created, as indicated by the limiting streamline pattern and by the study of the crossplanes. Figure 8.4 shows that the two vortices follow the edges of the antenna back and merge into the longitudinal vortices. The antenna base vortices are the most dominating structures, and can be identified easily in the limiting streamline pattern and the crossplanes. Due to the very high Q level they seem to end shortly behind the antenna, however, the vortices reach downstream over the rear window as shown in Figure 8.5, where the isosurface Q=1000 is shown. Also the 2D streamlines indicate a quick dissipation of the antenna vortices. This shows that the 2D streamlines can be misleading in the identification of a vortex.

8.2 Rear window flow

The limiting streamline pattern over the rear window, showed different connections between the upstream flow, as for instance from the antenna, and characteristic features observed at lower rear window edge. The investigation of different crossplanes, as it was also done for the flow behind the antenna, gives a deeper understanding of the flow development in this area. As it was already implied by the Q isosurface in Figure 8.5, the

antenna base vortices extend over the rear window; to what extent, and how they merge with other structures will be analysed in the following section.

Figure 8.6 shows three different crossplanes over the upper rear window. The furthest upstream plane A (Figure 8.6a) shows four distinct vorticity spots. To the very left and very right, two spots are observed which are rotating in opposite direction. As will also be shown later, these are the A-pillar vortices. Left and right from the centreline, the previously discussed antenna base vortices can be seen. The 2D streamline pattern shows that the flow is directed downwards with a slight in-wash; whereby the in-wash is stronger at the sides of the vehicle. Underneath the vorticity spots a boundary layer develops. On the left hand side in Figure 8.6a the x- vorticity is negative and on the right hand side positive. Thinking of the sketch in Figure 8.3 a similar explanation can be given here. The in-wash of the bulk flow creates a boundary layer development towards the centreline, which in turn causes an induced negative x-vorticity on the left hand side and an induce positive x-vorticity on the right hand side. The A-pillar vortices rotating in the opposite direction compared to the boundary layer vorticity amplify the induced vorticity creation (explanation see Figure 8.3). Underneath the antenna base vortices the surface x-vorticity is of opposite sign to the vortex rotation, following the previous explanation. The created layer in this case is very thin and therefore hardly seen in the shown crossplane. However, the surface x-vorticity over the rear window, shown in Figure 7.14, makes the distribution clear.

At the upper left and right window edge positive bifurcation lines emanate. These were already observed in the limiting streamline pattern, Figure 7.14. The x-vorticity distribution on the surface shows a switch in sign left and right of the bifurcation lines,

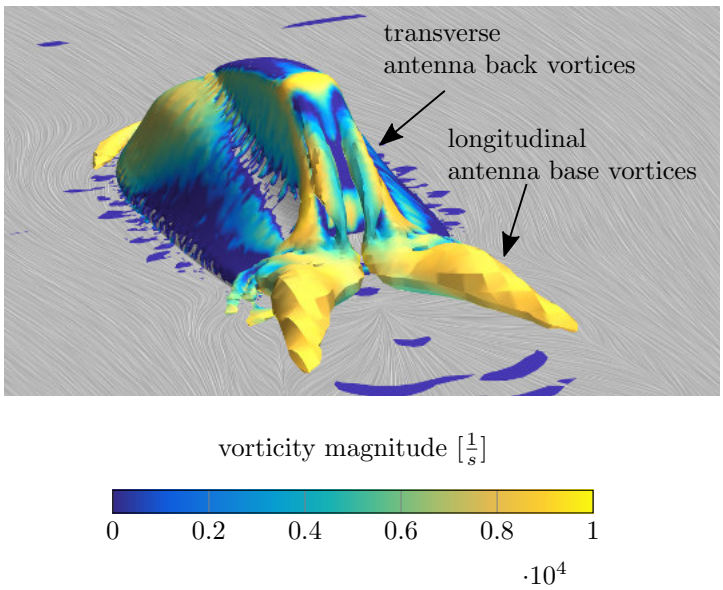

Figure 8.4: *Isosurface Q = 500000; coloured by vorticity magnitude*

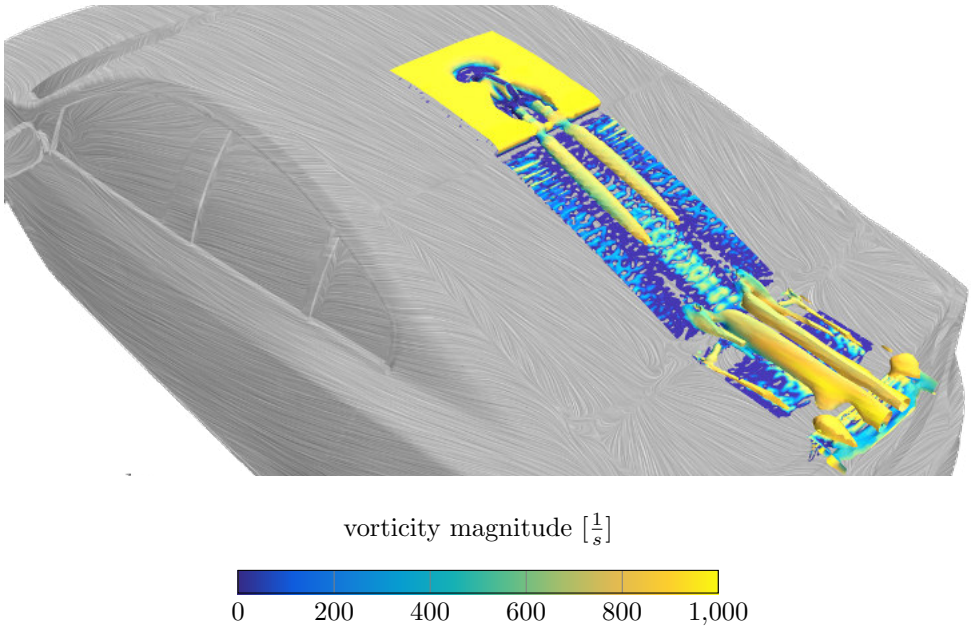

Figure 8.5: *Isosurface Q = 1000; coloured by vorticity magnitude*

which is understandable considering the local transverse flow directions. The crossplane in Figure 8.6b shows that, similar to the layer underneath the antenna base vorticities, the layer is very thin and therefore hardly visible in the crossplane. The surface x-vorticity distribution gives in that respect a better insight.

Plane C (Figure 8.6c) is located approximately where S_2 is observed in Figure 7.14. Throughout the three presented planes it can be seen that the level of x-vorticity decreases for both the A-pillar and antenna base vortices. The vorticity layer at the sides of the rear window is created by the in-wash of the flow and amplified by the A-pillar vortices. The creation of this layer is so strong, that it even covers and suppresses the boundary layer created due to the diverging flow along the positive bifurcation line. In the corners between rear window and C-pillar the x-vorticity distribution shows the development of a vorticity spot, which indicates the development of a vortex.

Figure 8.7 shows the further downstream development up to a plane close to the trunk edge. The spots in the corners were identified as potential vortices. Now even the 2D streamline pattern shows a focus structure. Left and right of the centreline four small x-vorticity spots are shown. These emanate from the foci structures observed in the limiting streamline pattern. Plane E (Figure 8.7b) is already located on the trunk. Still present are the A-pillar vortices and the corner vortices. The vortices created by the surface foci structures seem to grow and further develop. In the last crossplane in Figure 8.7c it seems that the vortices next to the centerline are dissipating, the A-pillar vortices appear to have the same x-vorticity level and also the corner vortices continue to develop.

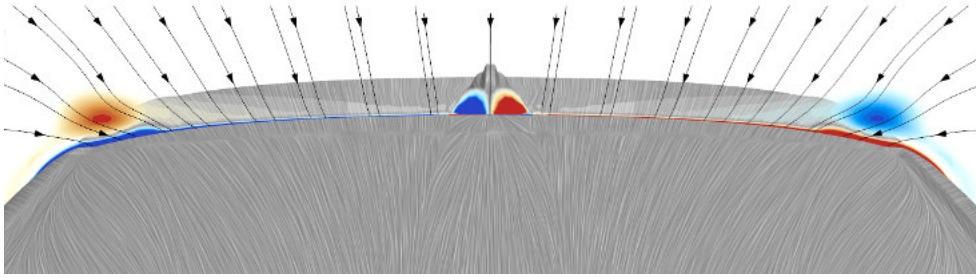

(a) *plane A*

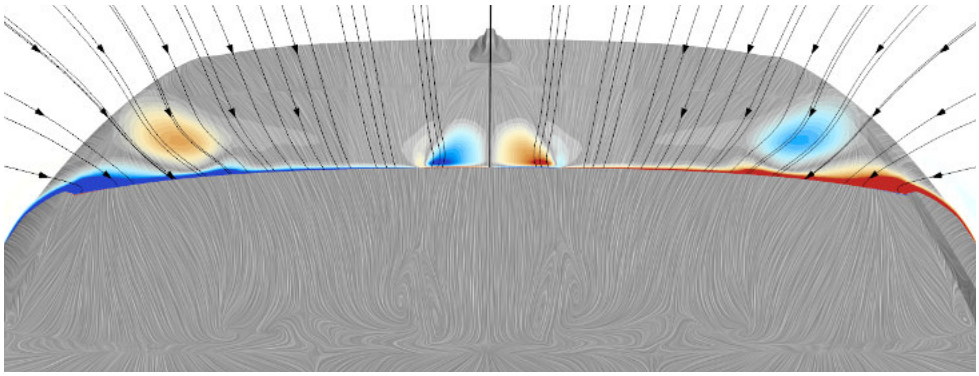

(b) *plane B (*400 mm *downstream of plane A)*

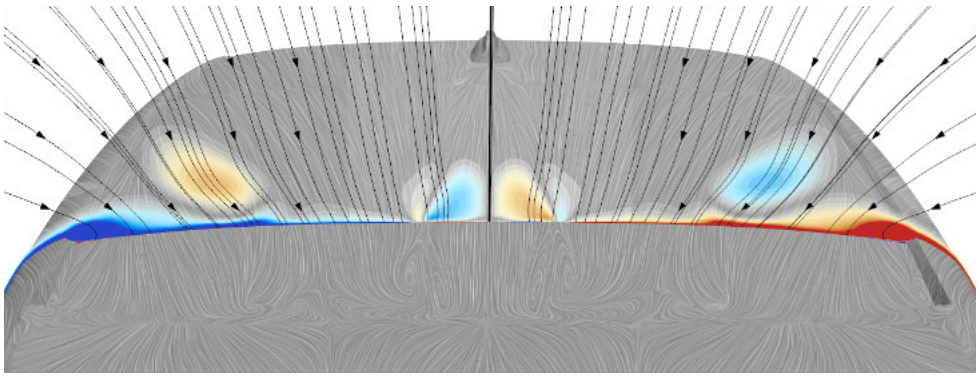

(c) *plane C (*600 mm *downstream of plane A)*

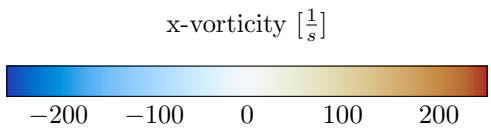

Figure 8.6: *Crossplanes over the rear window - part 1; coloured by x-vorticity*

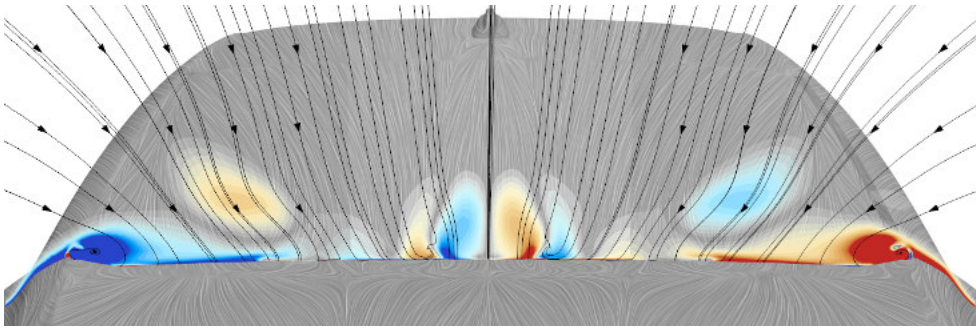

(a) *plane D (*800 mm *downstream of plane A)*

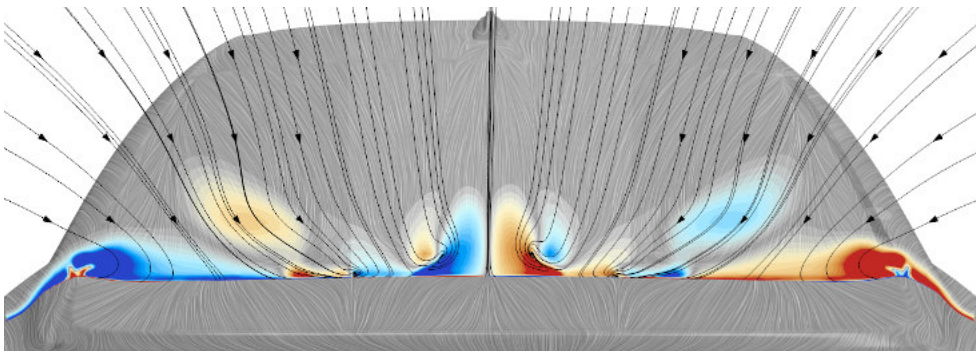

(b) *plane E (*900 mm *downstream of plane A)*

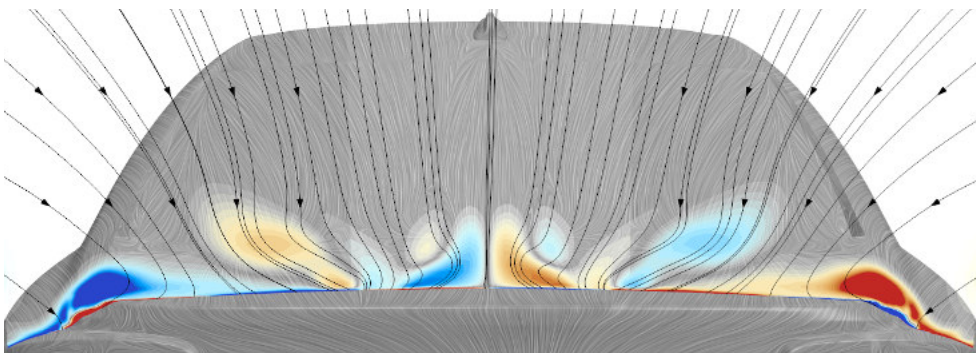

(c) *plane F (*1100 mm *downstream of plane A)*

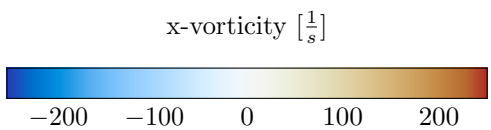

Figure 8.7: *Crossplanes over the rear window - part 2; coloured by x-vorticity*

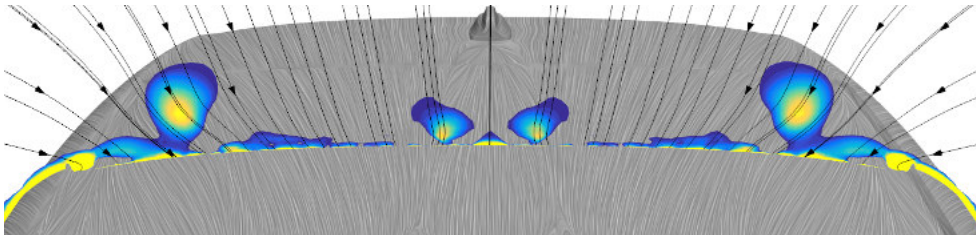

(a) *plane B*

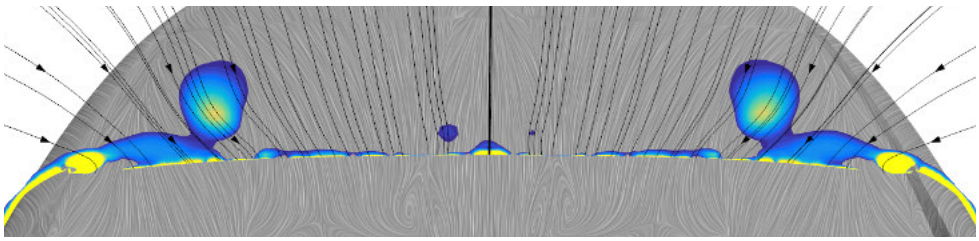

(b) *plane C*

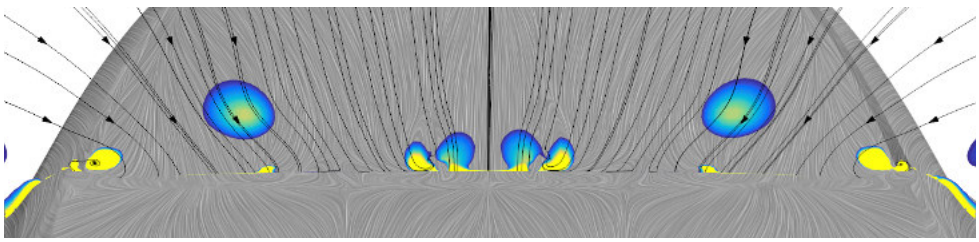

(c) *plane D*

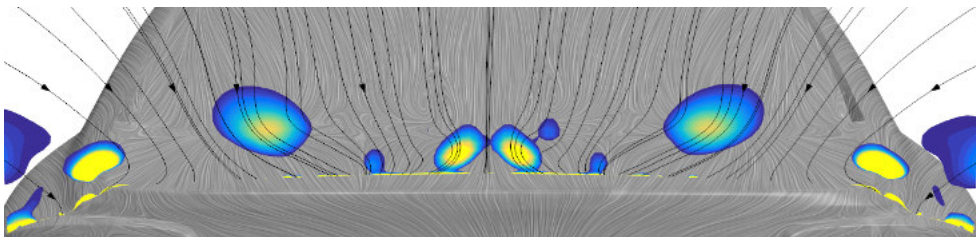

(d) *plane F*

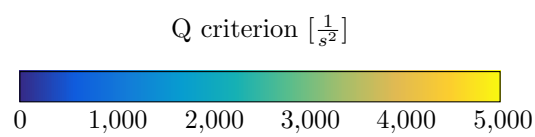

Figure 8.8: *Crossplanes over the rear window; coloured by Q criterion*

To get a better impression of the created vortices and to be able to estimate their size more quantitatively, the Q criterion is plotted in plane B,C,D and F which is shown in Figure 8.8. Plane B in Figure 8.6b showed the A-pillar vortices and the antenna base vortices. The x-vorticity gathering in the corners between window and C-pillar are not directly identified as vortices. However looking into the Q criterion (Figure 8.8a) shows a spot with positive Q, which is interpreted as a vortex. Moving further downstream to plane C, the x-vorticity distribution in Figure 8.6c shows the A-pillar vortices and leads also to the assumption that the antenna base vortices are still present. However the Q criterion (Figure 8.8b) shows that the antenna base vortices are almost dissipated. From the x-vorticity distribution and the Q criterion in plane D similar conclusions regarding the occurring vortices are drawn and also in plane F the main structures are identified with both parameters. In general, the Q criterion shows a more distinct boundary for the individual structures, while from the x-vorticity it is difficult to draw an exact border.

Comparing the x-vorticity and Q criterion distribution with the 2D streamline pattern, it attracts attention that mostly the 2D streamlines do not show a focus structure, where a vortex is identified. This difficulty is was also seen in the previous chapter and is taken up and explained in the following section on the example of the A-pillar vortex.

8.3 A-pillar flow

Based on the previous discussions, the topology on the A-pillar indicates a crossflow separation. To be able to understand how the flow leaves the surface and into which structures its develops, crossplanes along the A-pillar and over the rear end are studied. Figure 8.9 shows the longitudinal locations for the selected planes.

According to the definition, the flow leaves the surface along the negative bifurcation line and rolls up into a vortex sheet. Analysing the 2D streamlines and the vorticity in different crossplanes give insight into the vortex formation and its development. Figure 8.10 shows the perspective view onto four crossplanes. Plane A and B are located in the beginning of the A-pillar. Plane C is located approximately at the end of the A-pillar and plane H is located at the rear window of the vehicle. The crossplanes, presented in

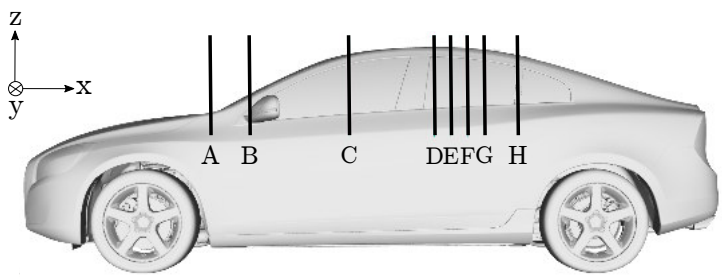

Figure 8.9: *Defined coordinate system and locations of crossplanes used in the discussion*

Figure 8.10, are coloured by vorticity magnitude and further show the 2D streamlines of the velocity components in z and y direction.

Plane A is located furthest upstream and does not show any indication of a vortex formation. Moving further downstream, the planes B and C show a focus in the 2D streamline pattern, which is rotating in counter clockwise direction (looking from behind). This A-pillar vortex results from flow leaving the surface along the convergence line. In plane C (Figure 8.10) the white and red line sketches the area where the vortex sheet

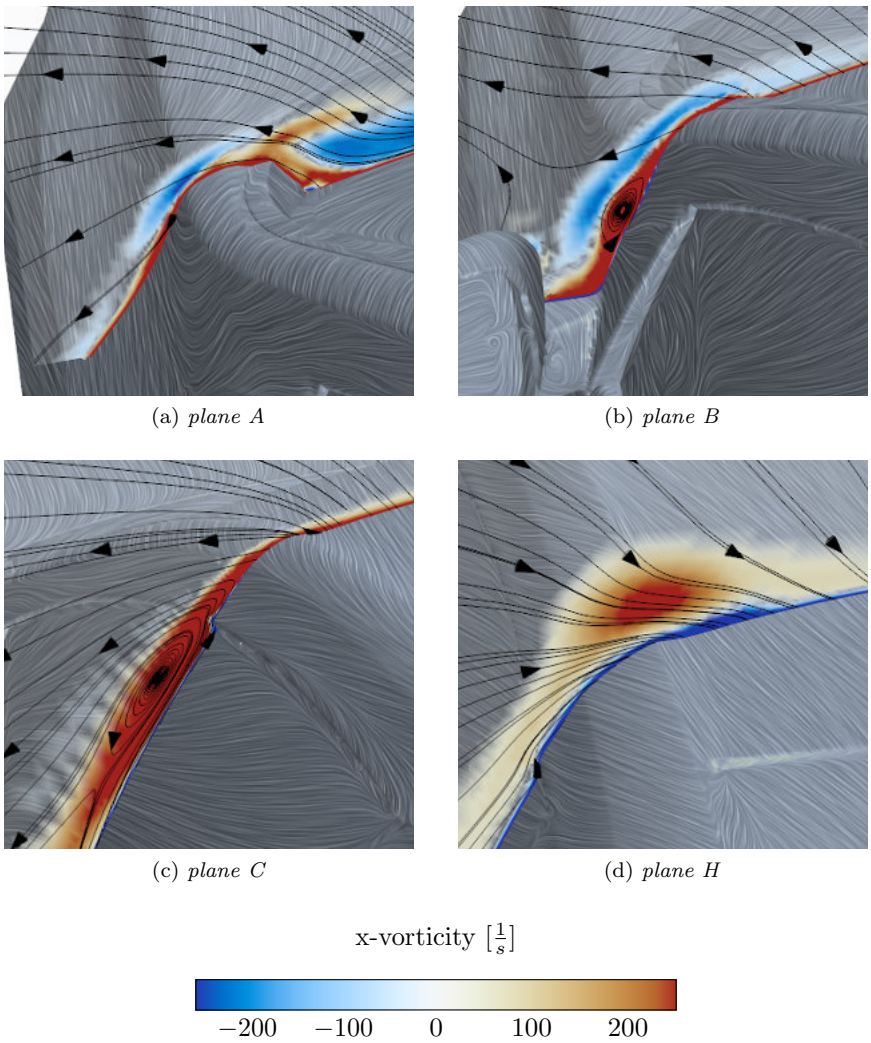

(a) *plane A*

(b) *plane B*

(c) *plane C*

(d) *plane H*

Figure 8.10: *Perspective view on four different crossplanes (A, B, C and H) along and downstream the A-pillar; coloured by x-vorticity and showing 2D streamlines in the crossplanes*

is leaving the surface. It can also be seen that the vortex core lies slightly beneath the bifurcation line rather than being created exactly on top of it. In a study done by Levy & Brancher [63] a generic A-pillar model was investigated regarding its topology and vortex development. Within this study a secondary A-pillar vortex was found. In the case of the production car, such a secondary vortex cannot be identified. Moving further downstream, the pattern in plane H does not show any longer the presence of a vortex. This leads to the conclusion that the A-pillar vortex has dissipated along the way and is no longer present.

Figure 8.11 shows the Q isosurface $Q = 0$ along and downstream the A-pillar. The isosurface is coloured by x-vorticity and shows the A-pillar vortex reaching from the beginning of the A-pillar, over the rear window into the wake. This development does not match the conclusion made from the 2D streamlines. Hence the 2D streamline pattern must be affected by additional phenomena causing the changes in the vortex representation. Therefore four additional planes are investigated (D,E,F and G). These are located in between plane C and H and cover the area where the focus in the 2D streamlines disappears (Figure 8.12).

The four planes are plotted in a distance of $\Delta x = 0.1\,\mathrm{m}$ ($\Delta x/L = 0.02$). In plane D the A-pillar vortex is still represented as a focus. The 2D streamlines over the roof are pointing in z direction (upwards). However, close to the surface the y component is dominating and the 2D streamlines point almost horizontally towards the centreline, before they are redirected in z. Slightly downstream, in plane E, the focus is still present. A drastic

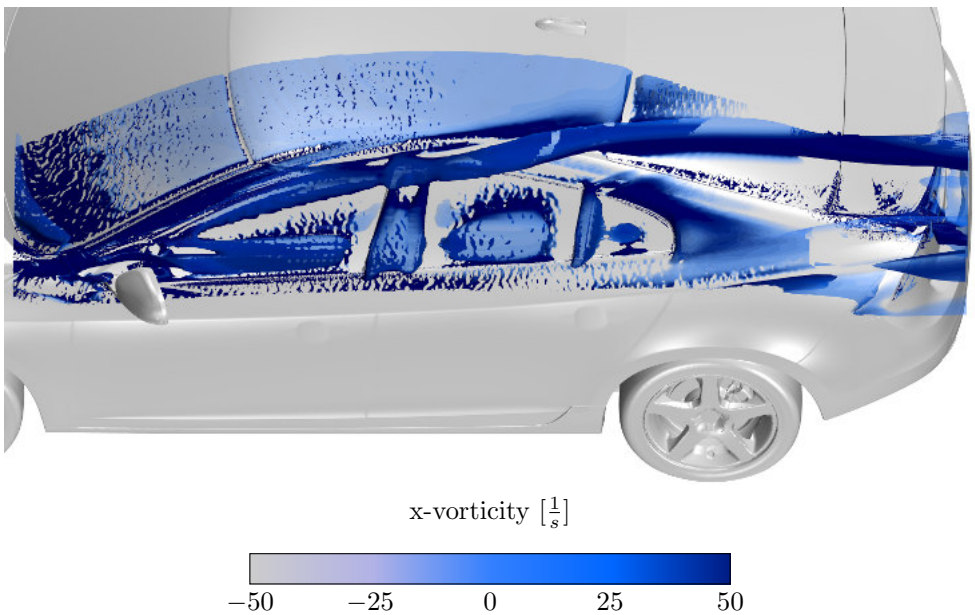

Figure 8.11: *A-pillar vortex visualized by the Q criterion Isosurface Q=0 and colored by the x-vorticity*

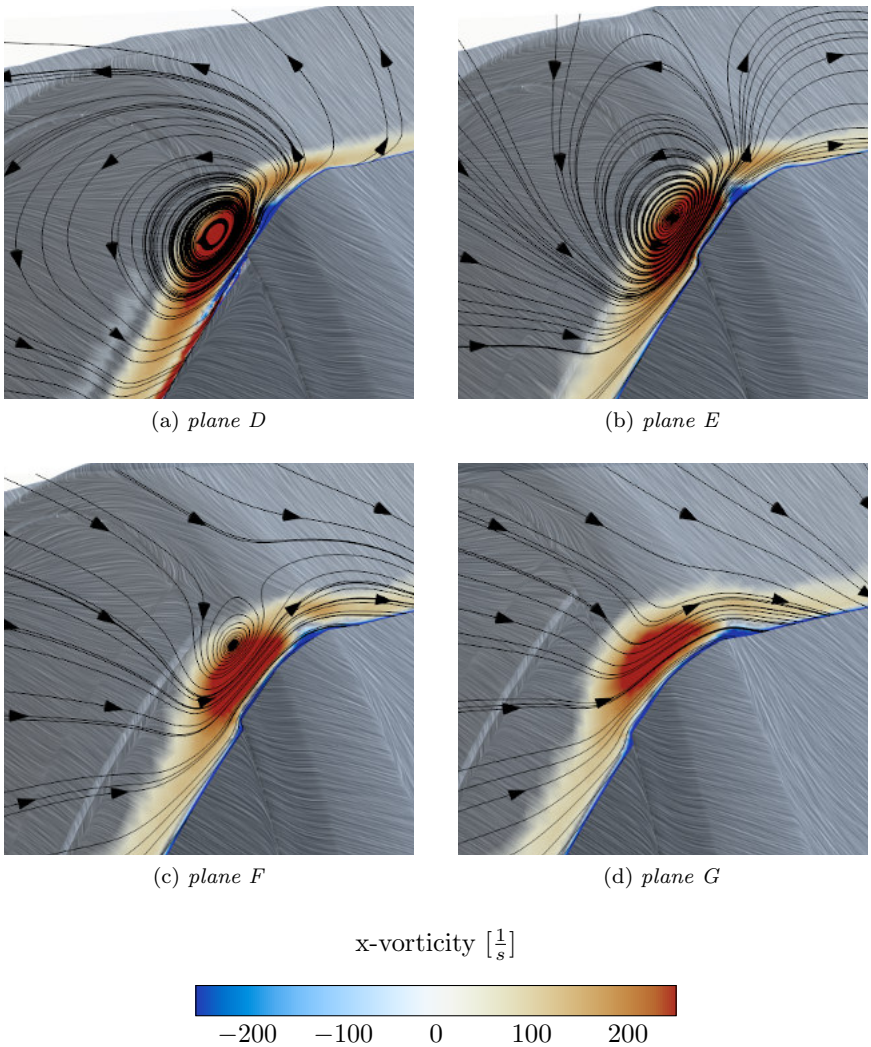

(a) *plane D* (b) *plane E*

(c) *plane F* (d) *plane G*

Figure 8.12: *Perspective view on four different crossplanes (D, E, F and G); coloured by vorticity magnitude and showing 2D streamlines in the crossplanes*

change can be seen in the 2D streamlines over the roof. In the near wall region the y component is still dominating. Compared to plane D, the 2D streamlines are now not as strongly directed up in z direction, but even curving downwards (Figure 8.12b); pointing towards the centreline. This change in direction becomes even more drastic looking into plane F. The rapid changes turning the 2D streamlines towards the vehicle surface cause the creation of a saddle point S. The saddle point S has to be present in plane E, but is located further up and therefore not captured by the shown clipping. In plane G the

vortex and the saddle point are no longer represented by the 2D streamlines. The overall direction is downwards with an in-wash towards the centreline.

The altering of the 2D streamline pattern is caused by the interaction of two phenomena. First the A-pillar vortex is created, which develops downstream along the vehicle. Over the roof of the vehicle the flow starts to curve towards the centreline. This is due to the created low pressure on the roof top which drags fluid from the sides towards the centreline. At the same time the flow decelerates over the rear window which makes the flow (and the A-pillar vortex) even more sensitive to the dragging pressure forces. The effect of the low pressure over the roof causes the in-wash and as the Q criterion shows, it also affects the path of the A-pillar vortex. The vortex is dragged towards the centreline before it merges with the vehicle wake. In summary it can be said that the vortex is present all along the vehicle length, however due to the in-wash of flow the 2D streamline representation is altered. This shows that the interpretation of the 2D streamlines can be misleading and has therefore to be analysed carefully.

8.4 Flow downstream of the front wheel arch

The limiting streamline pattern obtained from CFD and experiment (Figure 7.20) showed major differences regarding the development of a recirculation zone. Also the surface pressure distribution show dissimilar distributions. It was already mentioned that for this area the chosen numerical approach can give misleading results. Therefore the analysis on occurring flow structures is based on experimental results of the near wall flow, using time resolved pressure measurements and tuft visualisations. The obtained results were presented and discussed in Section 7.4.3.

8.5 Base wake flow

Figure 8.13 shows a crossplane at the vehicle rear end and a second one 3.7 m ($x/L = 1.8$) further downstream. In Figure 8.13a, to the left and right of the centreline, the vortices created by the antenna and amplified by the rear window horn separation, can be seen. To the left of the centreline and the antenna vortex, a larger red spot appears, which results from the A-pillar vortex. Underneath of it a negative boundary vorticity is created. To the left of the A-pillar vortex another blue spot can be detected. This is the vortex which is created at the lower C-pillar edge. To the left of the C-pillar vortex two spots with lower x-vorticity can be seen. These are emanating from the side mirrors. On the upper right trunk corner another dark blue spot appears. This must have been created at the trunk surface and seems to form another vortex. At the lower left corner several structures can be observed which are created by the flow around the rear wheel and wheelhouse, as well as from the underbody flow.

While the first plane shows many different smaller vortex structures, the plane in the wake behind the vehicle shows two developed counter rotating vortices (Figure 8.13b). The left

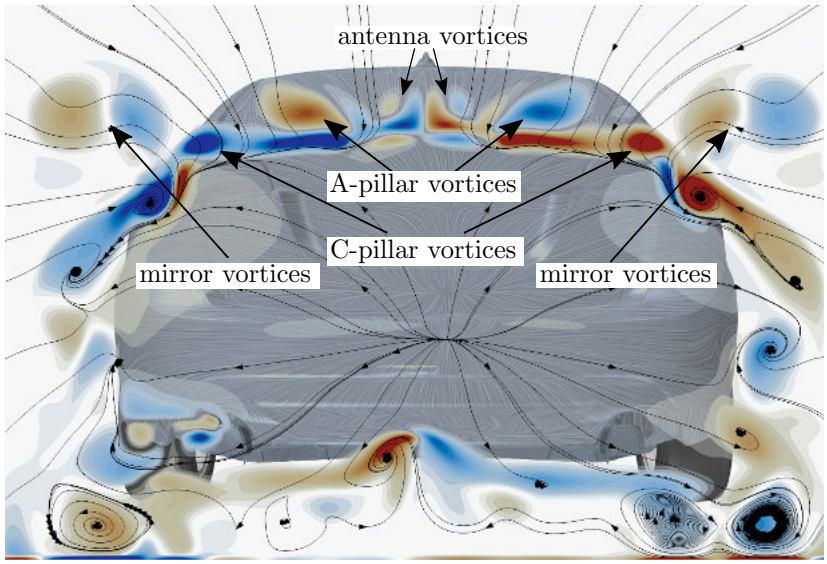

(a) $x/L = 1$ *(base plane)*

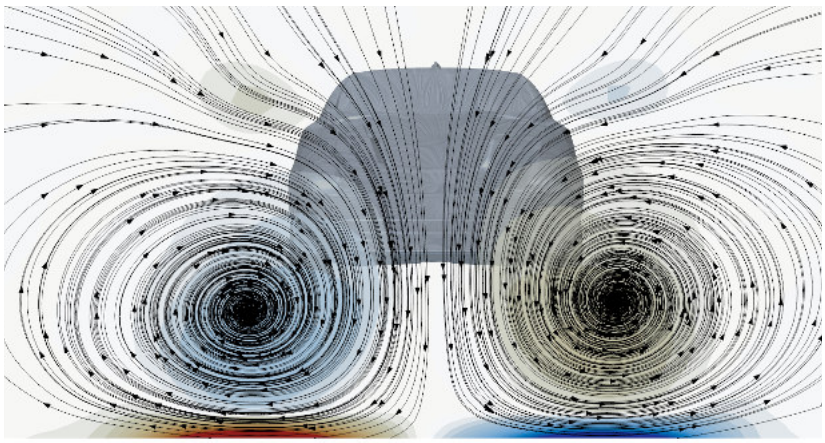

(b) $x/L = 1.8$

x-vorticity $[\frac{1}{s}]$

Figure 8.13: *Crossplane with 2D streamlines at the rear end ($x/L = 0$) and $x/L = 0.8$ downstream of the vehicle base; coloured by x-vorticity*

one rotates clockwise (negative x-vorticity), while the right one rotates counter clockwise (positive x-vorticity). Hence a downwash is produced in the centreline. These vortices are commonly known as the trailing vortices of the base wake. Underneath the two trailing vortices, a vorticity sheet with opposite sign as the vortex rotation is observable. This is an induced surface vorticity, which is created in a similar way as it was described for the antenna base vortices.

The occurring question is how and where these are created and how are the characteristics from the limiting streamline pattern related to the occurring flow structures. To investigate their development, different crossplanes are analysed. Figure 8.14 and 8.15 show eight different plane positions starting slightly upstream of the vehicle base. The first two images give a perspective view onto the vehicle and the crossplane, while the latter ones give a view from behind of the vehicle. In each plane the 2D streamlines are plotted and the plane is coloured by x-vorticity. The left trailing vortex in Figure 8.13b shows negative x-vorticity, hence it shall be traced, how this negative x-vorticity is transported throughout the planes.

In order to trace the sources of the trailing vortices, it is practical to follow the planes backwards in the upstream direction. Tracing the x-vorticity back upstream it can be seen that the negative contribution arises from the vortex spotted at the upper left trunk corner (Figure 8.14b) which emanates from N_4 (cf. Figure 7.28). The vorticity contribution from the trunk vortex merges with the small C-pillar vortex, which has as well a negative sense of rotation, and with negative vorticity created behind the rear wheel (Figure 8.15b). Figure 8.15c and 8.15f show that even the negative rotating part of the side mirror vortex is entrained into the vorticity cloud until the developing structure forms the trailing

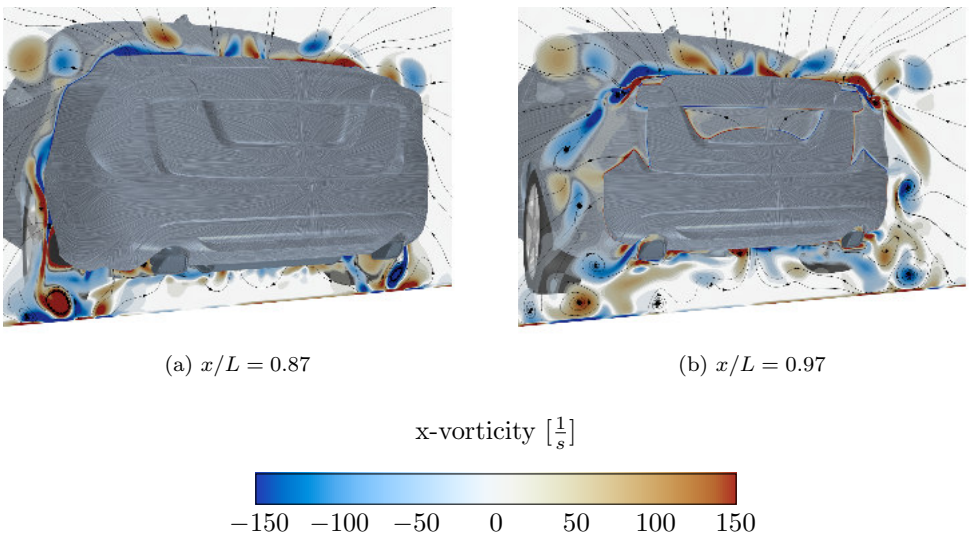

(a) $x/L = 0.87$ (b) $x/L = 0.97$

Figure 8.14: *Crossplanes upstream of the vehicle base - part 1; coloured by x-vorticity*

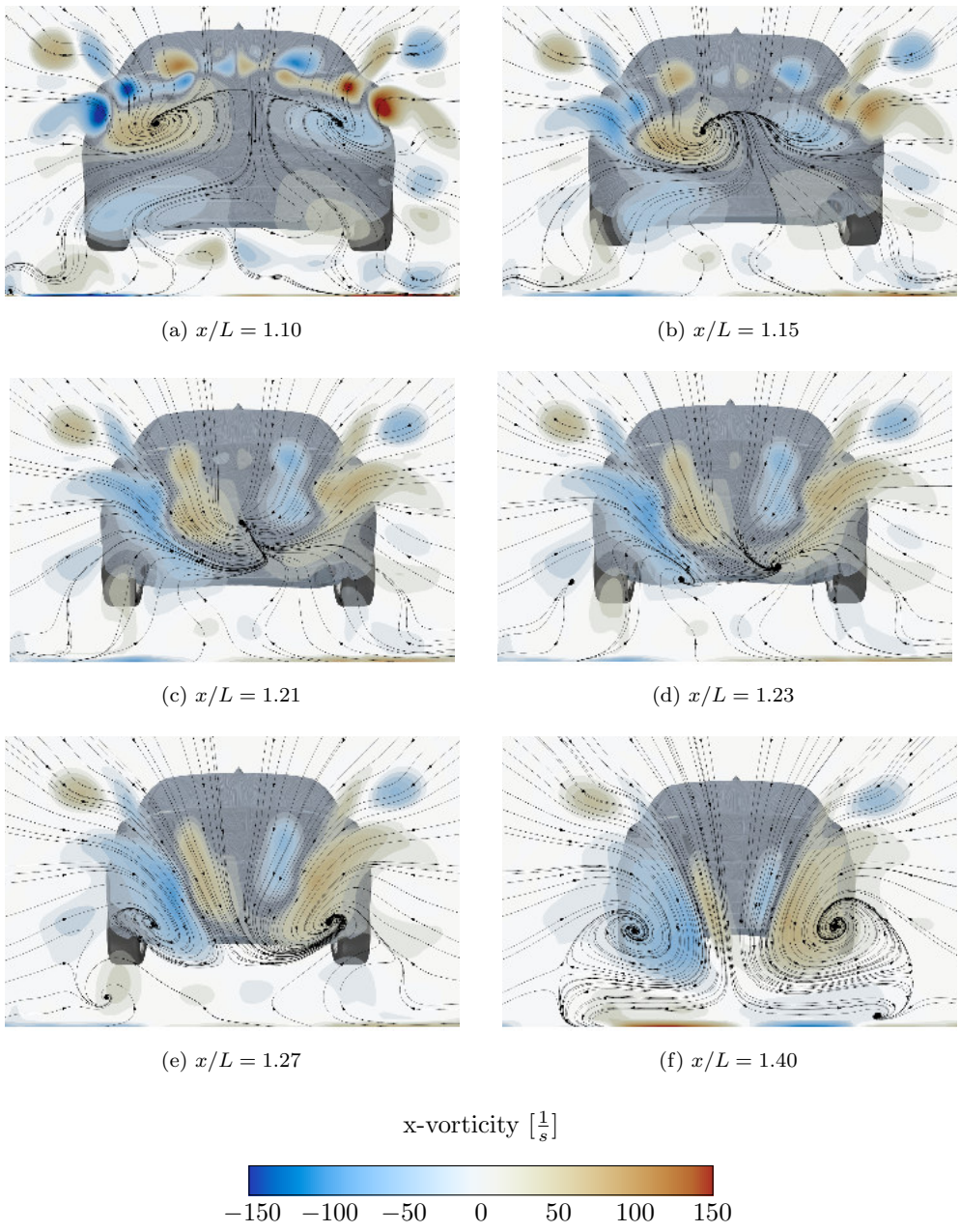

(a) $x/L = 1.10$ (b) $x/L = 1.15$

(c) $x/L = 1.21$ (d) $x/L = 1.23$

(e) $x/L = 1.27$ (f) $x/L = 1.40$

Figure 8.15: *Crossplanes upstream and downstream of the vehicle base - part 2; coloured by x-vorticity*

vortex. This suggests that the trailing vortices originate on the vehicle base and that the containing vorticity is a result of a merge of different phenomena. This is contrary to many explanations given in literature, where it is stated that the trailing vortices are a pure result from the C-pillar separation and hence also often called the C-pillar vortices.

An additional perspective shall be given by looking at the Q criterion. Further it shall be investigated, how the described vorticity clouds interact with the recirculation zone, described in section 7.5. Figure 8.16 to 8.19 show crossplanes together with its 2D streamlines, similar to Figure 8.14 and 8.15; additionally the 2D streamlines in the longitudinal centre plane are shown.

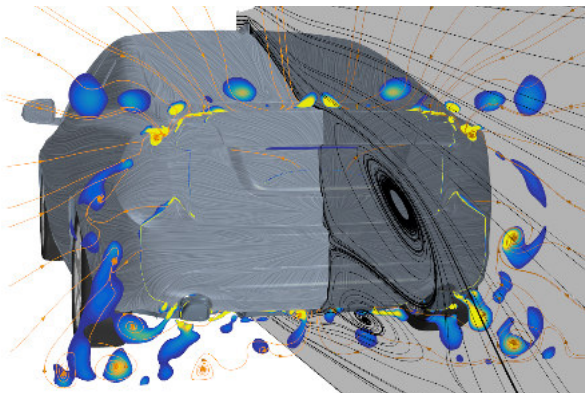

(a) $x/L = 0.97$

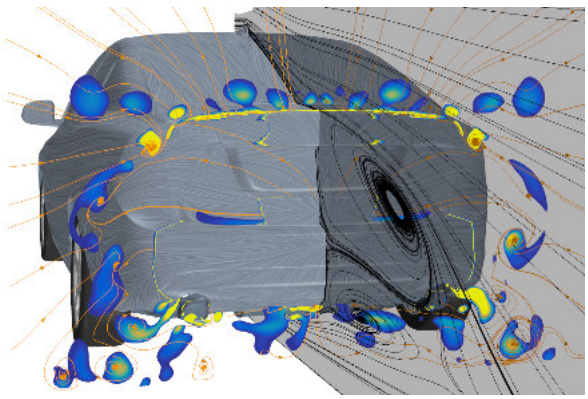

(b) $x/L = 0.98$

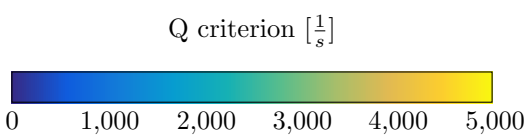

Figure 8.16: *Crossplanes upstream of the vehicle base coloured by Q criterion, $Q > 0$ - part 1*

Figure 8.16a shows a plane slightly upstream the vehicle base (corresponding to Figure 8.14b). The Q distribution shows clearly the A-pillar vortex, the mirror vortices and many smaller structures around the vehicle. In the area of the upper left corner of the trunk, two bright yellow spots appear. The smaller one, located between mirror and A-pillar vortex, is the resulting structure from the C-pillar separation (C-pillar vortex). The yellow spot located below, results from the separation node N_4 (cf. Figure 7.28) and corresponds to the negative vorticity spot described in connection with Figure 8.13a. Contrary to the vorticity distribution, the Q criterion shows that these two structures are not connected.

Figure 8.16b shows a plane 40 mm further downstream. The orange streamlines in the crossplane show an almost horizontal bifurcation line at the height of the upper trunk edge. This is the line building the vortex sheet, which separates the flow from inside the recirculation region from the flow coming over the trunk. Looking back to Figure 7.28 this separation surface is created by the crossflow separation emanating from the centreline saddle S_3. The described converging 2D streamlines are oriented away from the centreline and end in the vortex structure created by N_4.

At the defined vehicle base ($x/L = 0$), shown in Figure 8.17a, it can be seen that the attachment point N_3, shown in Figure 7.28 results from the reattachment of the recirculation region. This point thus splits the flow in the upper and lower recirculation regions. Flow emanating from this point is directed away until it joins different structures. Fluid directed vertical upwards converges towards the separation-surface-line described previously. Between N_3 and S_3 smaller local separations occur, due to the corners. In the base plane Figure 8.17a this trunk-separation-surface line does not any longer end in the vortex created by N_4 but merges with the vortex created by the focus F_2. Fluid above the attachment point seems to belong to the upper recirculation structure, while flow below the attachment node seems to create the lower recirculation structure. Fluid distributed to the side joins the vortex created by F_1 and fluid directed towards the ground merges with different smaller structures created by the underbody and wheel flow.

Further 40 mm downstream (Figure 8.17b), the crossplanes show the development of two large foci to the left and right of the centreline. The upper foci are connected by convergence lines which close the recirculation region at the top. Around the sides and at the area close to the ground, no such distinct convergence lines can be detected. It rather seems that flow is entrained by the recirculation region. The distribution of the Q criterion shows that the areas where the rotation is dominating, forms a circular shape around the wake, which seems to be filled. The vortex emanated from N_4 still appears as a bright yellow spot, while the vortex created by the C-pillar appears to become smaller. The two described vortices did not merge together so far. Close to the closure point of the recirculation region, the observed foci in the crossplanes are gone (Figure 8.18a).

The blue spot to the upper left is the primary mirror vortex. The spot slightly below is the trunk corner vortex (N_4). The detected C-pillar vortex is no longer present. Compared to the vorticity distribution in Figure 8.15b this image shows a much clearer picture of the occurring structures. While the vorticity distribution suggests a merge off different vortices to one large structure, the Q criterion shows that the vortex emanating from

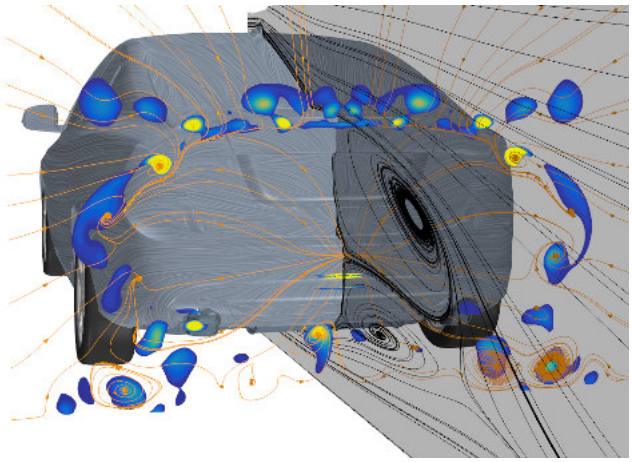

(a) $x/L = 1$

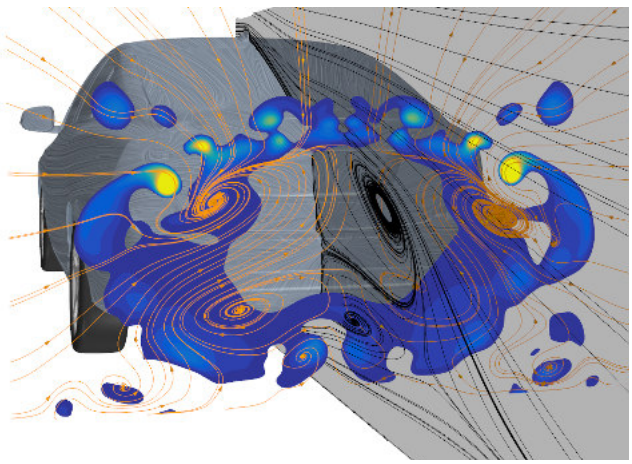

(b) $x/L = 1.06$

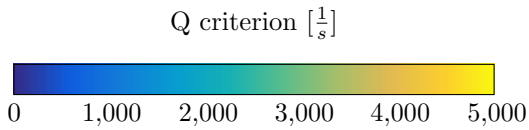

Figure 8.17: *Crossplanes downstream of the vehicle base coloured by Q criterion, $Q > 0$ - part 2*

N_4 is the dominant one. Directly after the wake closure point (Figure 8.18b), the 2D streamlines in the crossplane show two new foci to the lower left and right of the centreline. The blue spot in the upper left is the mirror vortex and the spot below is the N_4 vortex, which seems to grow in size. The blue spot observed in the centre of Figure 8.18a is dissipated.

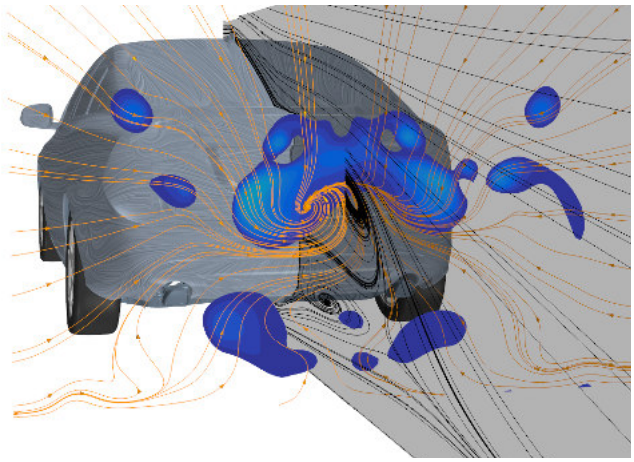

(a) $x/L = 1.15$

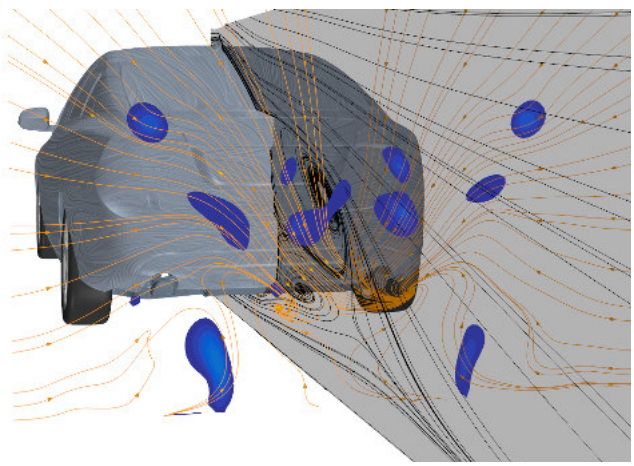

(b) $x/L = 1.24$

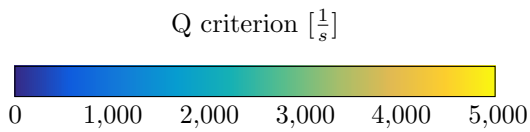

Figure 8.18: *Crossplanes downstream of the vehicle base coloured by Q criterion, $Q > 0$ - part 3*

The last crossplane shown (Figure 8.19), is located at $x/L = 1.40$, downstream of the vehicle base, and was already shown coloured by x-vorticity in Figure 8.15f. The 2D streamlines show the two trailing vortices and the Q criterion shows two large spots in this area. These are the vortices traced all the way from N_4. On their path downstream, they grew in size and moved closer towards the centreline and towards the ground, until they

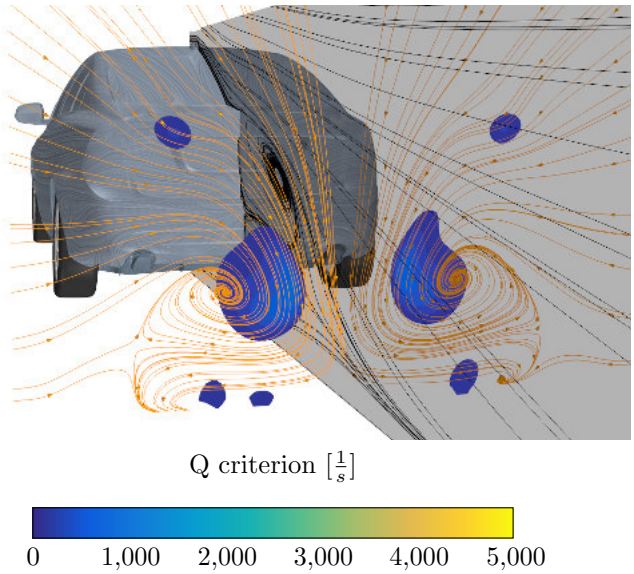

Figure 8.19: *Crossplane $x/L = 1.40$; coloured by Q criterion, $Q > 0$*

form the distinct vehicle wake vortices. Already from their beginning, they were located outside of the described recirculation zone. After the recirculation zone was closed, these vortices could develop and grow. Tracing the flow structures through different planes in the downstream flow showed where these trailing vortices emanate from and that they are created on the vehicle base and not at the C-pillar.

The x-vorticity was investigated to understand the development of longitudinal vortices which result in the trailing vortices. Together with the Q criterion it is possible to identify the single vortex structures and to trace where the sources lie. The following Figure 8.20 shows the distribution of the vorticity magnitude. From the $x/L = 0$ plane in Figure 8.20a, it can be seen that the largest amount of vorticity, entering the wake, is produced over the trunk deck. At the base itself, the vorticity is very low. This was already expected, looking at the wall shear stress distribution in Figure 7.29, where the base showed a low wall shear stress magnitude. Around the recirculation zone a circular band appears which contains higher vorticity than its surrounding. Within the recirculation zone the vorticity is zero or almost zero. Moving further downstream,this area is successively filled with with vorticity.

A similar observation is made in Bonitz et al. [8]. In this work the flow field was investigated using the local drag formulation [70]. Based on the crossflow velocities a local drag can be calculated which can be attributed to regions of drag creation. The work by Bonitz et al. [8] showed that the highest local drag is observed in a circular band of the shape of the vehicle rear end. However, in the centre area the local drag was low. Moving further downstream, the local drag in the centre increased and decreased in the outer band due to momentum transport.

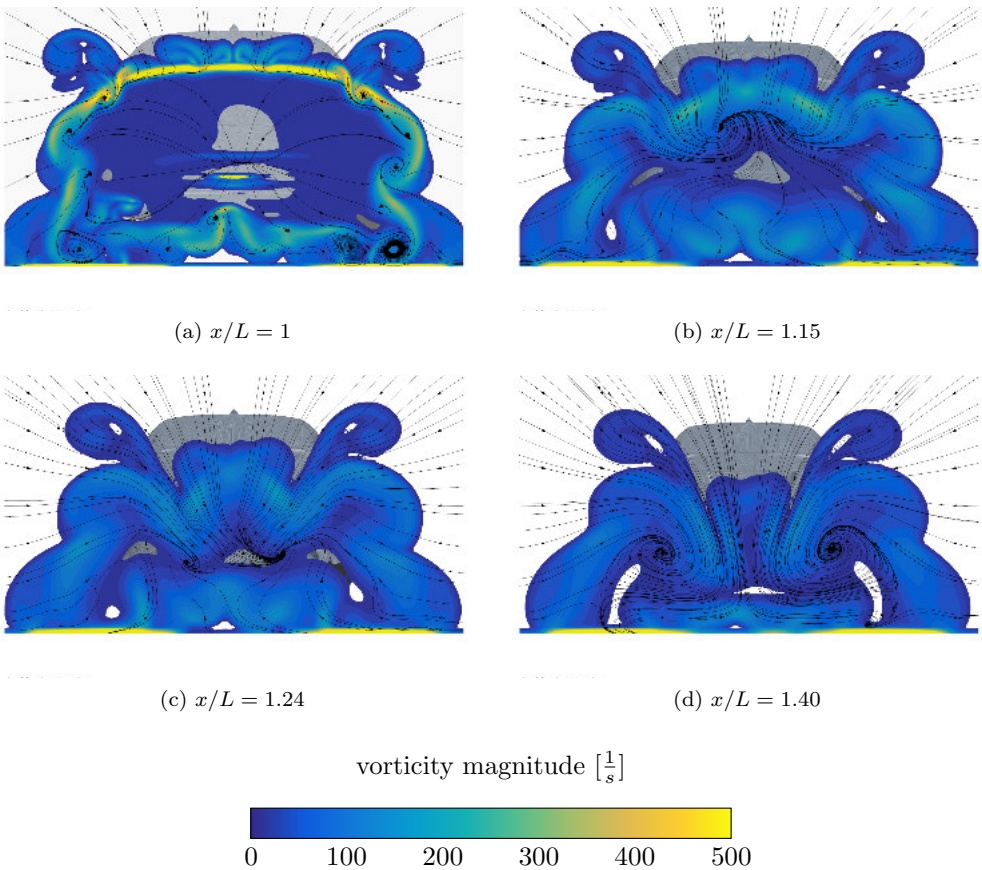

(a) $x/L = 1$

(b) $x/L = 1.15$

(c) $x/L = 1.24$

(d) $x/L = 1.40$

Figure 8.20: *Crossplanes downstream of the vehicle base; coloured by vorticity magnitude*

Chapter 9

Discussion

The previous chapters described the identification of potential separation regions by means of limiting streamlines, followed by an analysis on how the near wall flow develops into the freestream and showed the possibilities for description and characterisation of evolving separation structures. In order to interpret the observed patterns, parameters influencing the created picture have to be understood and how sensitive they are towards different changes. The sensitivity of the limiting streamline pattern will be investigated by changing different parameters. First the effect of the Reynolds number is discussed. Second, the geometry is altered by i) smoothing the rear window to be able to analyse the flow pattern created, when the flow stagnations are reduced and ii) by removing the antenna to be able to understand the influence of its created flow pattern. As a last aspect, it is shown how the pattern differs using the steady state approach compared to an unsteady solution.

Apart from the changes in the surface pattern, it shall also be investigated how the dominant flow structures might be altered. Further it will be discussed how the limiting streamline pattern and surface properties can be used to predict developing flow structures.

9.1 Reynolds number effects

In order to analyse the effect of the Reynolds number, the case at 100 km/h is compared to a case at 140 km/h. The mesh was the same for both cases and the wall y^+ distribution for the two cases is shown in Figure 9.1. It can be seen that the y^+ values are slightly higher for the 140 km/h case, however they are still below one on the exterior. The pattern around the antenna does not show any differences for the two inflow velocities and also the topology along the A-pillar does not change. Over the rear window the pattern is similar to the one for the driving condition at 100 km/h. The only difference which can

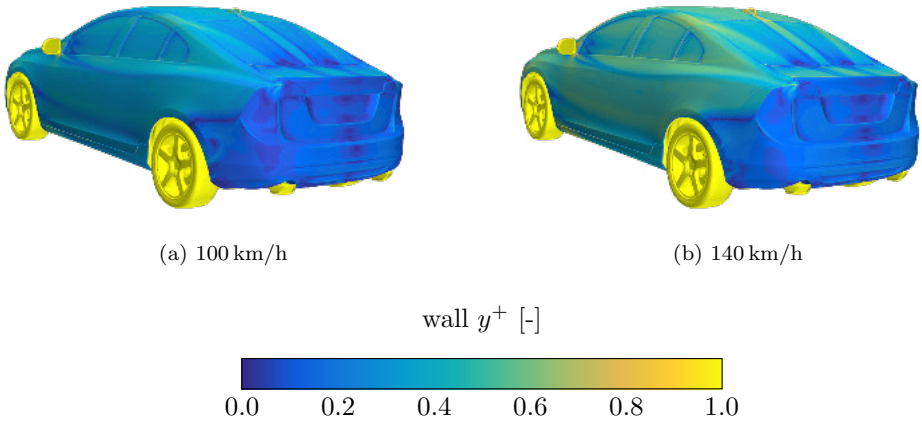

(a) 100 km/h (b) 140 km/h

Figure 9.1: *Wall* y^+ *distribution for* 100 km/h *and* 140 km/h

be noticed, concerns the foci F_3, F_4 and S_4 shown in Figure 7.9b. These three singular points melt together for the pattern observed at 140 km/h, resulting in one focus. The singular points of this node-saddle-node combination laid already very close together at 100 km/h. As it was described by Chapman & Yates [36] such combinations can appear as one node when the points are melting together and causes no problems in the discussion on the topological pattern. Hence this change is not seen as crucial and it can be said that the pattern is not affected by the Reynolds number. This was also shown in the work by Depardon et al. [55] on a scale model.

9.2 Effects of geometry changes

Changes in the geometry can influence the flow development and the creation of structures. In the following section it is discussed how the limiting streamline pattern and the resulting flow field changes, when i) the the rear window is smoothed and ii) the shark fin antenna geometry is removed.

9.2.1 Smoothed rear window

In section 7.2 it was observed that the limiting streamline pattern obtained by experiment and CFD showed slight differences. It was explained that small differences in the geometry could change the flow stagnation at the lower rear window edge, when the trunk is reached. To investigate the effect of flow stagnation in this area, a configuration with a modified rear window is investigated. The rear window surface was extruded, to connect without any edges to the C-pillar, as well as to the trunk.

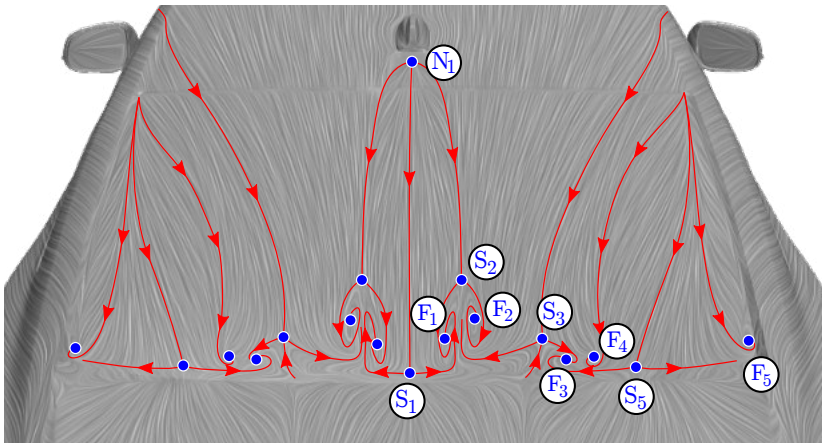

(a) *original window geometry*

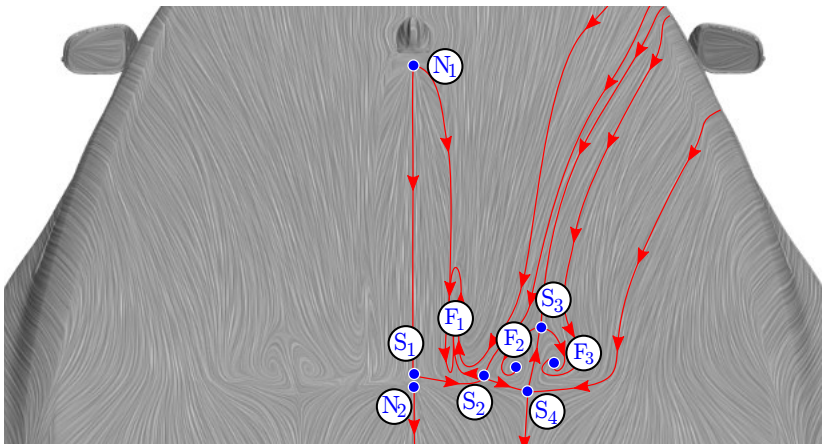

(b) *smoothed rear window geometry*

Figure 9.2: *Limiting streamline pattern for the two rear window geometries*

The limiting streamline pattern for the smooth configuration is shown in Figure 9.2. With the smooth rear window, the stagnation at the lower window edge is reduced; especially at the centreline. It can be seen that for this configuration on each side two larger counter rotating foci are created (F_2 and F_3 in Figure 9.2b). The separatrix from their saddle point S_3 is a limiting streamline coming over the roof. The observed focus pair F_2-F_3 is similar to the one observed in experiments, as shown by the paint visualisation (Figure 7.9c) as well as the tuft visualisation (Figure 7.10). The initial simulation showed foci structures directly to the left and to the right of the centreline (F_1 and F_2 in Figure 9.2a). For the smoothed case, these seem to be stretched out along the bifurcation lines created behind the antenna, resulting in one stretched focus F_1. In summary it can be said that the modified rear window geometry, with the reduced stagnation causes a

limiting streamline pattern similar to the experimental results; hence the assumptions and explanations stated before seem to hold.

To what extent the different surface pattern changes the developing structures will be investigated by comparing the crossplanes for these two configurations. The identification of the planes is according to the locations used in section 8.2. In plane A which is located upstream of the rear window, no differences occur. Moving downstream, Figure 9.3 shows plane B for the two configurations. The A-pillar vortices occur in both configurations at the same location and also their vorticity level does not change significantly. The antenna base vortices over the smooth configuration shows a higher vorticity area compared to the original geometry; however their appearance and location match. The boundary vorticity seems to be the same in both cases as well. Although the vorticity layer is thicker for the original case in the side edges, the general distribution is comparable. Similar observations can be made for plane C. This is expected, as the most significant differences in the limiting streamline pattern appear further downstream.

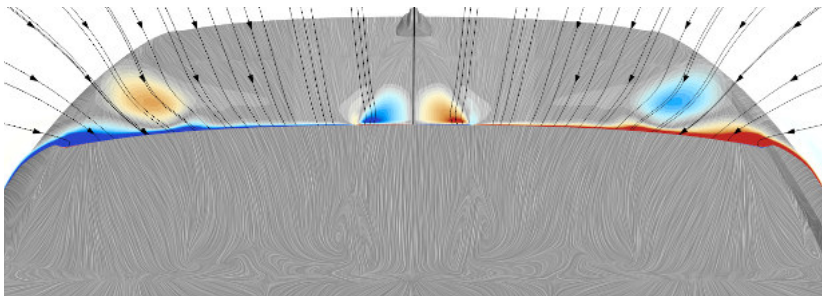

(a) *original rear window*

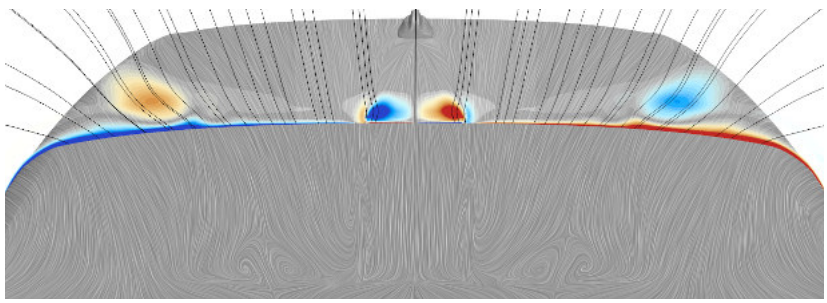

(b) *smooth rear window*

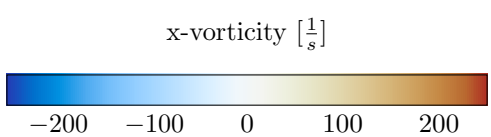

Figure 9.3: *Comparision of the flow field in Plane B*

Closer to the transition between rear window and trunk (plane C) the limiting streamline pattern shows significant differences. However, the crossplanes shown in Figure 9.4 look surprisingly similar; nevertheless changes can be observed. First of all the vortices created at the C-pillar edges do not develop in the smooth configuration, which is expected. The A-pillar vortices were expected to be unchanged, as can be seen in the figure. Though it was expected to see significant differences in the area between the A-pillar vortices. Figure 9.4 shows a very similar x-vorticity distribution, which leads to the conclusion that the altered surface pattern does not affect the longitudinal vortex development.

This observation can be confirmed looking into plane D, which is located on the trunk. Figure 9.5 shows plane D coloured by positive values of the Q criterion. Comparing the two crossplanes over the trunk, shows that the differences are minor. Even the C-pillar vortices, which showed to develop in Figure 9.4a, could be identified as similar structures. This observations are interesting as it was expected to see larger effect onto the developing flow structures, as soon as the surface pattern is changed. This comparison though showed that the the dominating structures, resulting from the flow over the rear window did not

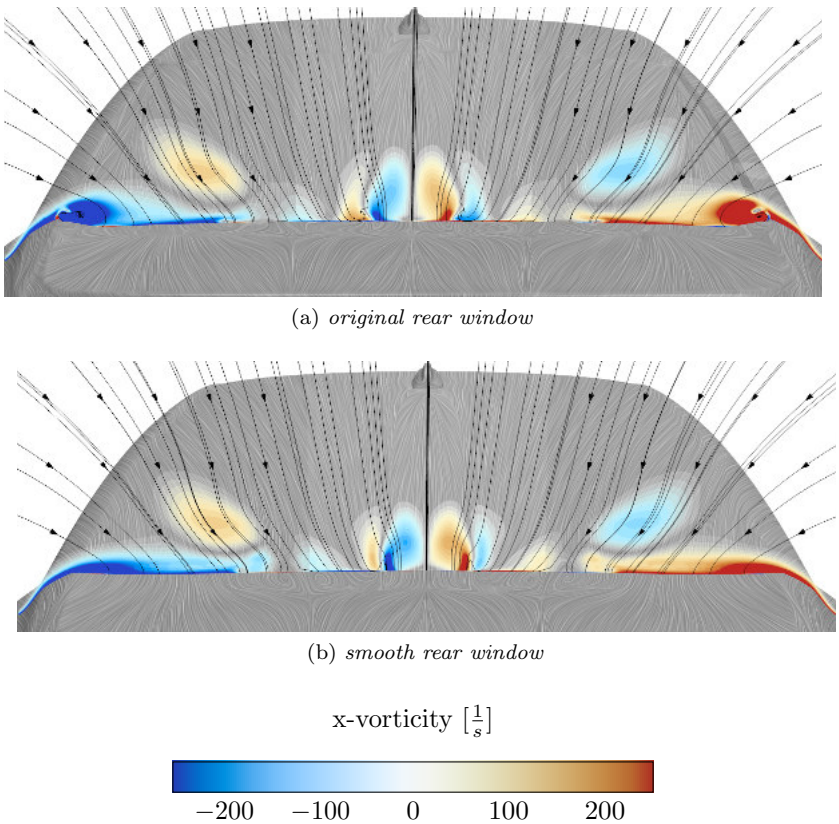

(a) *original rear window*

(b) *smooth rear window*

Figure 9.4: *Comparison of the flow field in Plane D; coloured by x-vorticity*

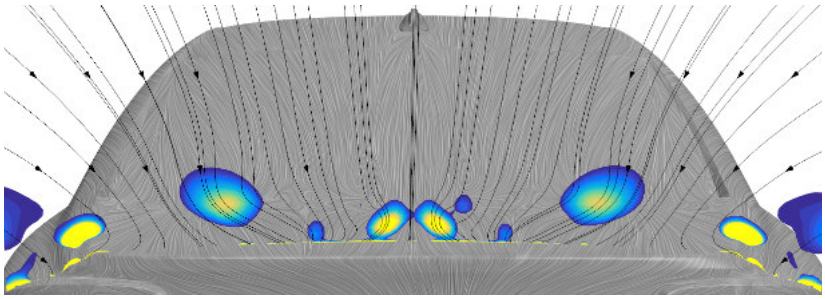

(a) *original rear window*

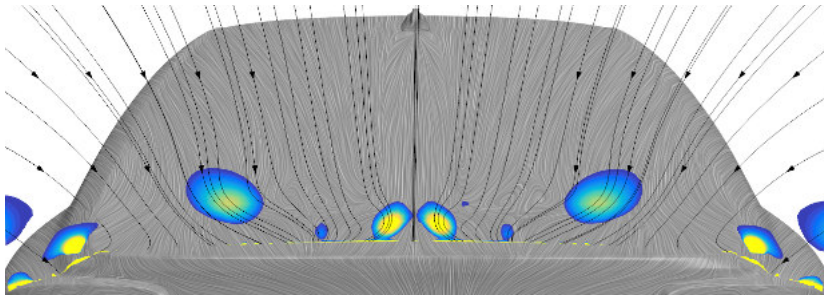

(b) *smooth rear window*

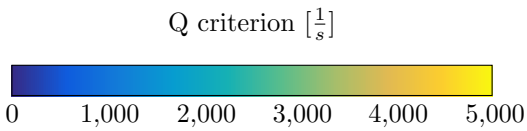

Figure 9.5: *Comparision of the flow field in plane F (*1100 mm *downstream of plane A); coloured by Q-criterion*

change significantly for the two configurations. The resulting structures observed are the two A-pillar vortices, the two antenna vortices, two small vortices which could be identified as C-pillar vortices and two small vortices created in between the A-pillar and antenna vortices. A comparison of the calculated drag values underlines the very little changes for the two configurations.

9.2.2 Flow development without the antenna geometry

Another interesting result is how the flow over the rear window is altered, when the antenna geometry is removed. Figure 9.6 shows the wall shear stress pattern and surface coloured by x-vorticity. Compared to Figure 7.14 only the distribution along the centreline is changed. The distribution towards the sides does not differ. Due to the in-wash of the flow the limiting streamlines are directed towards the centerline. This causes the negative surface x-vorticity to the left and the positive x-vorticity to right. With the presence of

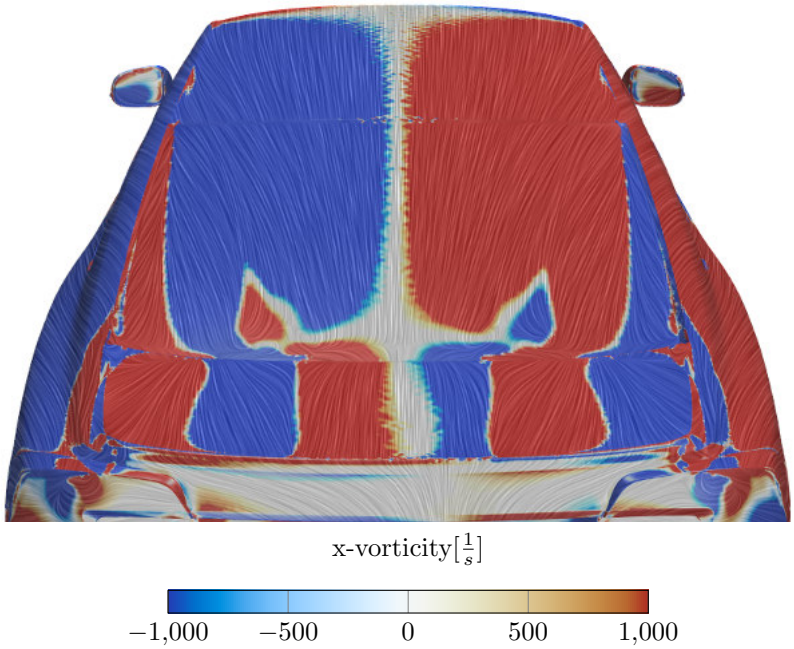

Figure 9.6: *Wall shear stress pattern over the rear window, without an antenna; surface coloured by x-vorticity*

the antenna, a narrow band existed, where the flow was directed away from the centreline, which caused two negative bifurcation lines. Further, the antenna base vortices induced a surface x-vorticity, which lead to a surface vorticity with an opposite sign as the antenna base vortices. It can now also be seen that the absence of the antenna changes the foci structures at the lower window edge. Before the negative bifurcation lines caused by the antenna end in a saddle point, from which two counter rotating foci were created. These do not exist for the case without the antenna. Instead, the flow stagnating at the lower window edge splits in the saddle point and create a focus on each side of the centerline, next to the foci structure created beneath S3.

The Figure 9.7 shows the vortex development over the rear window for the configuration without the antenna. Comparing the occurring structures to Figure 9.4a it can be observed, that the A and C-pillar development are the same, the small structures created next to the centreline (Figure 9.4a) do not occur in the case without the antenna. This is expected, as the surface foci structures next to the centreline, which are observed in the baseline case, do not develop. This development is also shown by the Q criterion in Figure 9.8, where it shows a crossplane over trunk, for the configuration without the antenna. The same plane for the case with antenna is shown in Figure 9.5a. Apart from the vortices created by the foci structures next to the centreline, no significant changes can be observed. This shows that the antenna vortices do not impact the the surrounding vortices

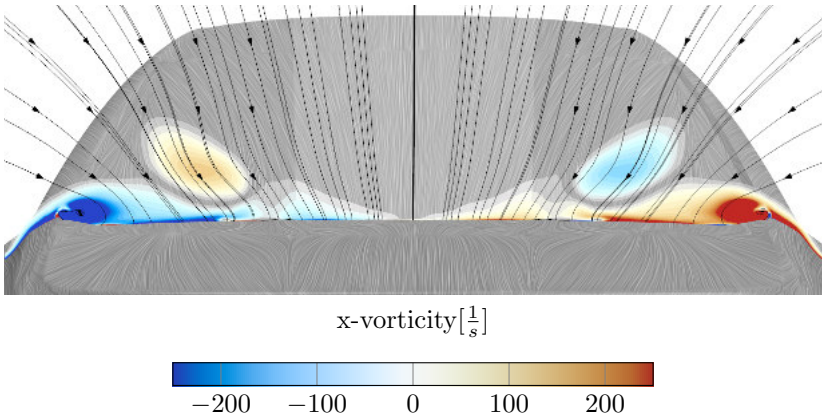

Figure 9.7: *Crossplane over the rear window without an antenna; coloured by x-vorticity*

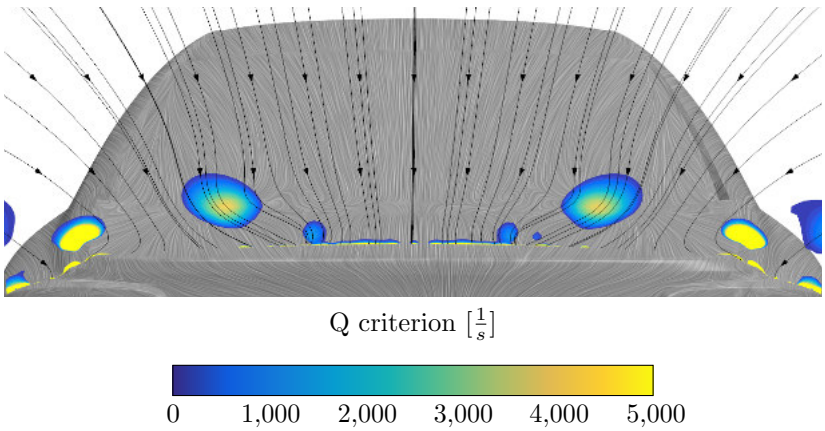

Figure 9.8: *Crossplane over the trunk without antenna; coloured by Q-criterion*

9.3 Simulation method

As a third aspect on the sensitivity of limiting streamlines, it is investigated how an unsteady calculation differs from the steady state case. The numerical method and setup for the presented unsteady results, using an IDDES approach, is described in Hobeika [71, 72]. The results presented for the unsteady case show the time averaged solution of the respective parameter. All shown parameters are averaged individually throughout the simulation.

Antenna flow

The limiting streamline pattern on and around the antenna is very similar for both simulation methods. The distribution of the surface x-vorticity components is also comparable in both cases. An investigation of the crossplanes show similar results as well.

Rear window flow

Figure 9.9 compares the rear window topology of the steady and unsteady result. In both

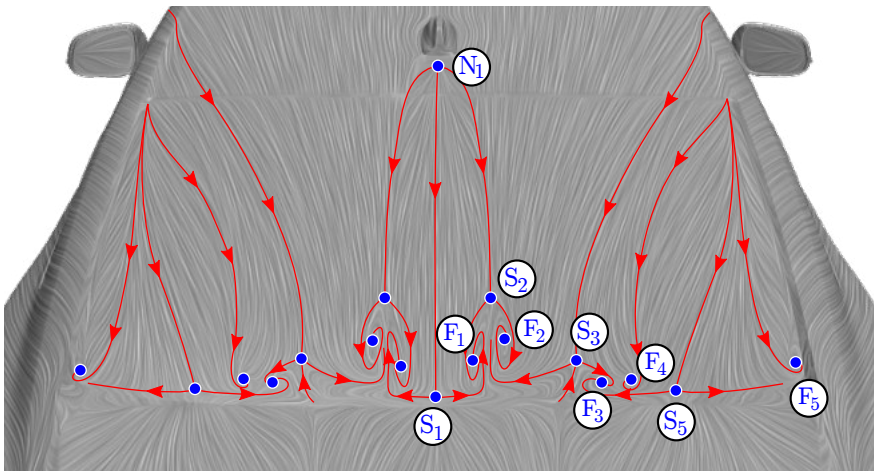

(a) *steady result*

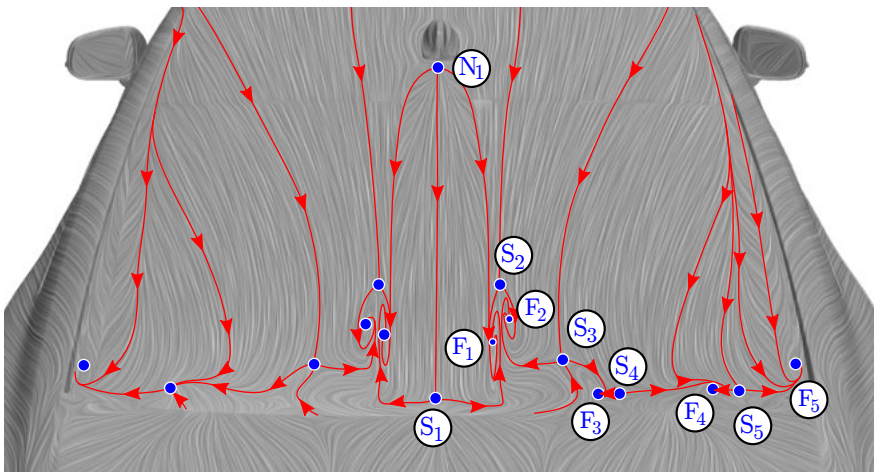

(b) *unsteady result*

Figure 9.9: *Limiting streamline pattern over the rear window for a steady and unsteady solution*

cases two bifurcation lines emanate behind the antenna and go over the rear window. At the lower window left and right of the centreline two foci pairs appear (F_1 and F_2 with their symmetric respective). In each pair the foci are counter rotating (see F_1 and F_2). For the unsteady case the pairs seem to be located slightly upstream compared to the steady solution and more squeezed together. Left and right of the focus pair F_1 and F_2, a saddle point S_3 is created in both cases. Again it seems that this is located slightly upstream in the unsteady solution. Moving further to the window sides, the unsteady solution shows less details on the left hand side, compared to the right. To the right, both solutions show two further foci structures (F_3 and F_4). The foci centres are slightly further away from each other in the unsteady case. At the lower window side edges in both cases a focus is created (F_5). The observed positive bifurcation line exits also in both cases. Between this bifurcation line and the side edge, the unsteady solution shows a clear negative bifurcation line ending in F_5. This is also existent in the steady solution, though located almost in the corner between window and C-pillar.

In general it can be said that the differences between steady and unsteady solution are negligible. All main features and characteristic points occur in both cases, with negligible differences in their location. It should also be noted that an unsteady approach showed the same differences in the limiting streamline pattern as the steady approach, comparing to the experimental results. In general the pattern over the rear window seems to be more sensitive to changes than in other regions. This explains also the many different distributions, of similar sets of singular points, reported in literature.

The investigation of the flow field shows slight differences in the shape, size and magnitude of the vorticity spots observed. However the same structures are identified with the two methods. The A-pillar vortices are identifiable along the rear window. Compared to the steady result, their shape in terms of vorticity are less elliptical, but show a slight L shape. The C-pillar vortex development looks similar in both cases and also the development of the antenna vortices and the vortices created by the rear window foci is comparable.

A-pillar flow

Along the A-pillar no significant changes were observed regarding the occurring crossflow separation. The x-vorticity distribution on the surface and the limiting streamline pattern are comparable and lead to the same conclusions for both methods.

Flow downstream of the wheelhouse

The limiting streamline pattern calculated by the steady state approach was shown in Figure 7.20a. Figure 9.10a shows the topology obtained by an unsteady approach. Compared to the steady state pattern, the unsteady pattern does not predict a recirculation downstream of the the wheel arch edge. The same observation was made comparing the experimental result with the steady state pattern. Figure 9.10a shows similarly to the experimental streamline pattern (Figure 9.10b) that the wall shear stress lines are bent down in the upper region before they are redirected horizontally downstream. At

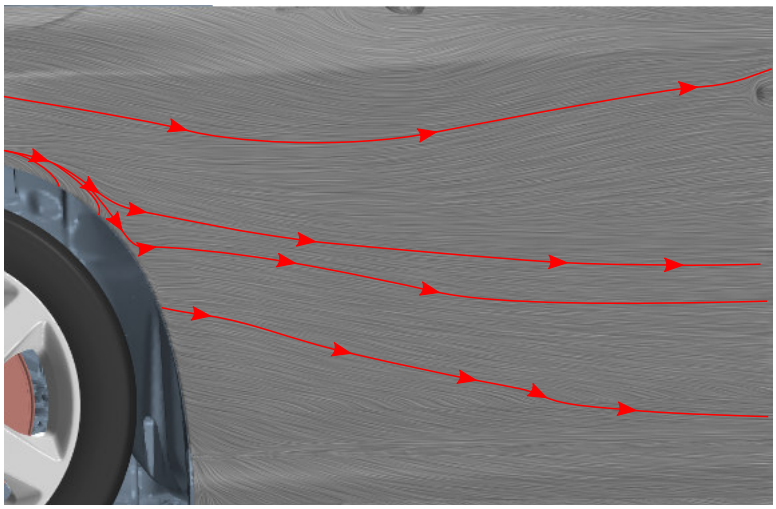

(a) *CFD unsteady*

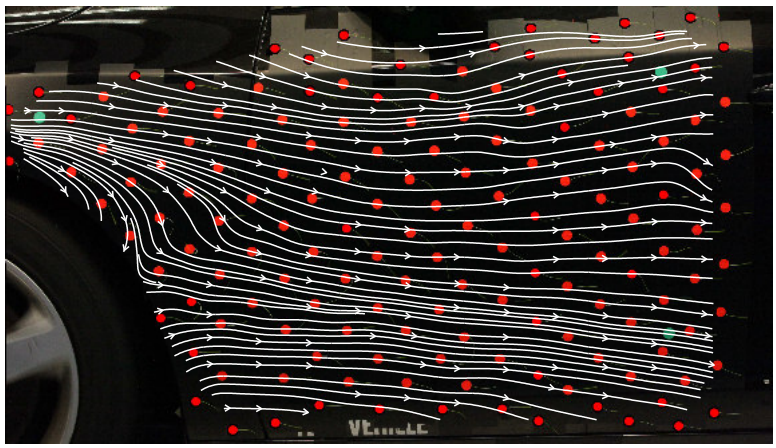

(b) *experiment*

Figure 9.10: *Limiting streamline pattern downstream of the front wheel; comparision between an unsteady CFD solution and experimental results*

the lower wheelhouse edge, the limiting streamlines indicate an edge separation at the wheel arch edge, where the limiting streamlines develop downstream, with slight down wash. Compared to the experimental topology, the wall shear stress lines bent down in a narrower region and align horizontally within a shorter distance. The horizontal alignment as well as the down wash of the limiting streamlines emanating at the lower wheelhouse edge can be seen in both the experimental and unsteady method.

Base wake flow

The wake flow downstream of the vehicle, shows for both simulation methods the characteristic trailing vortices. Closer to the vehicle base, the results of the two methods show similar features regarding the occurring vorticity spots and the 2D streamlines, but also main differences. The unsteady result was obtained using a sliding mesh approach, which has an influence onto the prediction of the wheel flow. Regarding the simulation time it is suspected that it would require to run the simulation longer than 2s averaging time to get a smooth time-averaged distribution of the gradients as vorticity and Q criterion. Further the two vehicle geometries have differences in their geometrical representation as for instance the suspension or the struts used in the wind tunnel, to keep the car in place.

9.4 On the identification and prediction of separation phenomena

The previous chapters presented the surface flow topology and the flow structure development on different areas on a passenger car. In order to identify and to analyse the flow, different methods were used, such as limiting streamlines, 2D streamlines and the Q criterion. The advantages and disadvantages of the methods used shall be discussed in the following section 9.4.1.

The second section 9.4.2 will discuss the correlation between characteristic topological features and the used surface properties and how a picture of the flow and separation structures can be derived.

9.4.1 Discussion on different methods to identify and predict separation

To identify and predict occurring separation phenomena, the following methods were used:

- limiting streamline pattern
- 2D streamlines
- vorticity
- Q criterion

The limiting streamline pattern allows to identify singular points and bifurcation lines to be able to characterize the surface flow topology. Even in experiments fairly simple methods exist to obtain a limiting streamline pattern as was shown using paint visualisations and tufts attached to the surface. From the topological picture it is possible to identify points and lines of separation as well as points and lines of attachment. The analysis

of the numerical results provided a higher resolution of the flow field and therefore a more detailed insight into the pattern. It was shown that singular points and bifurcation lines can be of small scale why it can be hard to identify some characteristics directly, as for instance the crossflow separation along the trunk edge. However, it is possible to reconstruct the pattern, considering the flow directions in the surrounding.

The 2D streamlines are often used to identify flow structures in planes. Mainly occurring foci patterns are in the focus as these are meant to show occurring vortices. Further they are useful to identify the local flow direction. The analysis of different areas around the vehicle showed that 2D streamlines can partly be misleading. The investigation of the A-pillar vortex development and the vortices created downstream of the antenna showed that the foci pattern in the 2D streamlines disappeared although a vortex was still present. This was explained by the altered flow situation due to the interaction of different flow phenomena.

Vorticity, and especially its components is often used as a vortex identification method. As by definition a vortex is an area of high vorticity concentration this is a helpful criteria. The single components further deliver the information of the sense of rotation. However, it is difficult to draw a concrete boundary which characterizes a vortex shape. Further, it is problematic to distinguish between vortex structures in the sense of a tube like shape, like a longitudinal vortex and the boundary layer or free shear layer. This difficulty was for instance described in the analysis of the development of the trailing vortices in the wake of the vehicle. As soon as the vorticity distribution of different phenomena merged together it was no longer possible to distinguish which source structure caused the trailing vortices development.

The Q criterion serves as a good vortex identification method as it defines the area where rotation is larger than the shear contribution. This allows to identify vortex structures in the flow as they appear as connected regions where $Q > 0$. However, close to the surface the vorticity production is high which makes it difficult to distinguish between the boundary layer and other occurring vortex structures. Also in areas where several structures occur, it can be that these lie close to each other and therefore appear as one large object in the Q representation. Nevertheless, it allowed for instance to trace the source of the trailing vortices in the wake of the car, which was not possible using the x-vorticity distribution.

9.4.2 Correlation between characteristic topological features and surface properties

In singular points, the wall shear stress is zero, that makes it possible to locate singular points on the surface. Additionally, it was found that the wall shear stress is low along negative bifurcation lines, which locates lines of crossflow separation. In some cases, as for instance the A-pillar the wall shear stress shows a jump along the bifurcation line.

The surface pressure distribution did not give distinct insight into the occurrence of characteristic features. This is mostly due to the fact that the surface pressure is influenced

by many different effects, as the geometry and interacting separation phenomena. Further, the representation and identification of different features is highly dependent on the chosen colour range. Hence it is difficult to use the surface pressure in order to identify and predict separation. A similar problem was described in [8] where the static pressure was used for vortex identification in the flow field.

The vorticity distribution was analysed on the surface and in the flow field. Especially the usage of vorticity components was helpful to identify occurring phenomena. On the surface the usage of the x-vorticity showed very promising results in order to identify longitudinal vortices created by crossflow separation, but also smaller structures as the transverse vortices at the antenna could be identified. This is due to the direct connection between wall shear stress lines and vorticity lines. The jumps in vorticity over a convergence or divergence line were also explained in a more general way by Wu et al. [37] (see also Section 4.3.5). As vorticity lines are always perpendicular to wall shear stress lines, their pattern on the wall across a negative bifurcation line can be drawn as shown in Figure 9.11a. Drawing the x and y components for a vorticity line shows that the y component does not change its direction, while the x component switches its sign crossing the convergence line. The observation of a rapid change in x-vorticity matches Wus' criterion regarding the observation of a crossflow separation. Hence the converging wall shear stress lines and the switch of x-vorticity direction characterizes crossflow separations.

This connection also allows to derive from the limiting streamline pattern, if the surface vorticity component switches from negative to positive or from positive to negative across a bifurcation line. The main near wall flow direction in Figure 9.11a is oriented in positive x direction. Due to the converging limiting streamlines the vorticity lines are bent, which causes a x-vorticity component. Looking in the main near wall flow direction (positive x direction) it can be seen that the x-vorticity switches from negative to positive across the negative bifurcation line going in positive y direction.

Now consider a divergence line as shown in Figure 9.11b. It can be seen that the sign of the x vorticity component switches from positive to negative across the bifurcation line going in positive y direction. The two schematics show further, that a large curvature radius results in a flat gradient across the bifurcation line and hence an observable zero vorticity component region, while a small curvature radius causes large gradients in the vorticity component, which results in the observation of distinct jumps. It can be said that the larger the curvature radius of the vorticity line, the lower the chance of a crossflow separation.

Knowing the limiting streamline pattern, it is possible to identify singular points of separation and attachment. Bifurcation lines show potential separation and attachment lines. Further, it is possible to derive parts of the surface vorticity distribution, due to the direct connection between limiting streamlines and vorticity lines. If a separation line is identified, it is of interest to tell, which sense of rotation the developing vortex will have. This means to know if the negative or the positive vorticity sheet will leave the surface. An indication can be given by the overall flow direction. For instance over the front screen, the flow is distributed towards the sides to go around the vehicle as well as over the vehicle. Looking at the A-pillar at the drivers side (left A-pillar when

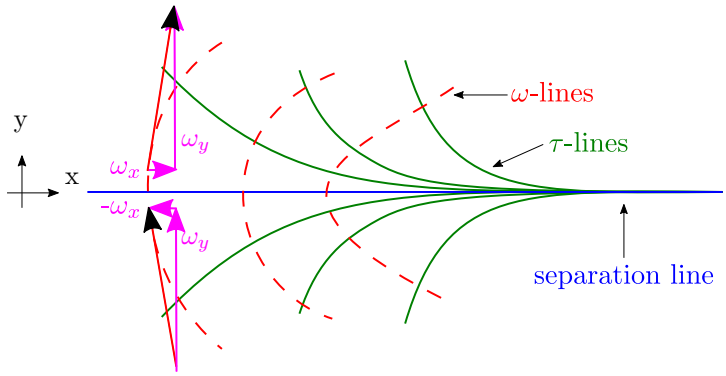

(a) *change in x-vorticity across a negative bifurcation line*

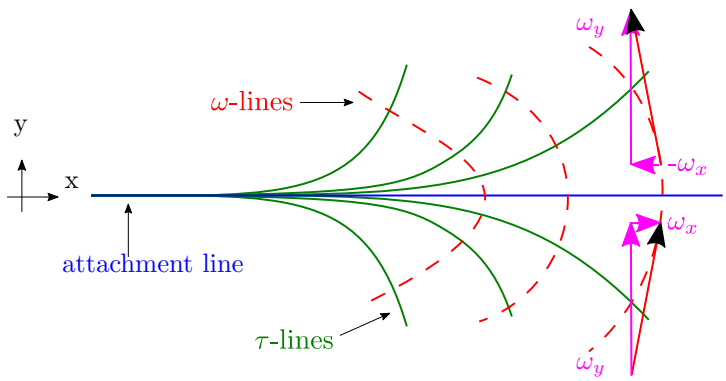

(b) *change in x-vorticity across a positive bifurcation line*

Figure 9.11: *Change in x-vorticity across a bifurcation line*

looking from behind), the flow is directed outwards in negative y direction, hence it can be expected to observe a developing longitudinal vortex structure with a positive sense of rotation. Similar consideration can be made by looking at the left C-pillar vortex (looking from behind). At the rear of the vehicle, overall flow direction is towards the centreline which supports the development of the negative vorticity sheet (in x-direction), causing a longitudinal vortex with negative sense of rotation.

Chapter 10

Conclusions

The presented work investigated different areas on a passenger car regarding occurring separation phenomena and how they develop into the flow. Three general separation patterns, were considered as relevant for this study: i) the bubble separation, the horn type separation and the crossflow separation (CFS). On a passenger vehicle several of these separation types can be found. These can vary in size and not all of them must develop into a significant large scale structure.

Around the vehicle exterior, five areas were presented where characteristic pattern in the flow topology were found. The flow on and around the antenna, the flow over the rear window and the trunk, the flow along the A-pillar, the flow downstream of the front wheel and the flow on and behind the vehicle base. The chosen regions show characteristic limiting streamline patterns and cover different flow situations. The antenna geometry for instance represents a 3D junction flow, while the area downstream of the front wheel is characterized by many different flow interactions.

The analysis was carried out in two steps. First the flow topology was investigated by studying the limiting streamline pattern and different surface properties in order to identify potential separation regions. Second, the development of identified separation structures into the flow was investigated. This was done analysing a number of crossplanes together with their 2D streamlines and different parameters, as vorticity (components) or the Q criterion.

Conclusions from the antenna flow

The limiting streamline pattern obtained from CFD matched well the observations from the paint visualisations. However, the CFD provided a more detailed insight. On the antenna several singular points and bifurcation lines were observed. In front of the antenna nose the characteristic saddle point for junction flows was found. On the inclined

edges at the antenna base, two small transverse vortices were created. This was indicated by negative bifurcation lines and a change in surface z-vorticity. Further, two node points of separation occurred on the left and right base corners, which resulted in two trailing vortices. Looking from behind, the left one rotates in clockwise direction (negative x-vorticity) and the right one in counter clockwise direction (positive x-vorticity). Hence, a downwash is created in the centreline.

The analysis of the crossplanes showed further that the created antenna base vortices change the surface vorticity distribution on the surface. Due to the rotation of the vortices, a vorticity sheet with the opposite sign is induced on the roof surface. This change was also shown comparing two vehicle configurations, one with and one without the antenna. Due to the induced vorticity, additional two crossflow separations were created. These were observable as two negative bifurcation lines downstream of the antenna, which caused a small crossflow separation. Following the antenna base vortices downstream showed that they exist over the entire rear window. This was best identifiable by using the Q criterion and the x-vorticity representation. The 2D streamlines were misleading in this analysis, as the two foci in the crossplane disappeared shortly behind the antenna base.

Conclusions from the rear window flow

Over the rear window the bifurcation lines created by the antenna base vortices ended in the foci structures at the lower window edge. These attract attention looking at the limiting streamline pattern, however the analysis of the cross planes showed that their resulting flow structures are comparably small. It was explained that the focus structures at the lower window are created by the flow stagnation in the corner between rear window and trunk. It could also be shown that the development of these foci structures is sensitive to the corner stagnation and hence the picture can differ slightly comparing CFD and experiments. Along the C-pillars a further crossflow separation was found. This could be identified by the bifurcation line and a distinct change in sign of the x-vorticity distribution. From the crossplane analysis, the A-pillar vortices could be identified, as well. However these lie too high above the surface to leave any footprint on the rear window.

Conclusions from the A-pillar flow

The flow along the A-pillar showed the creation and development of a fairly isolated CFS, leading to a longitudinal vortex which exists along the whole vehicle length and joins the rear wake. The converging streamlines and the change in x-vorticity sign on the surface showed the exact location. It was even possible to qualitatively locate the starting point of the CFS, due to the change of sign in the x-vorticity. The crossplanes showed the development of the A-pillar vortex and its path. While the x-vorticity and Q criterion gave very good information on the location and the development of the vortex, it was shown that the 2D streamlines can be misleading. Due to the overall vehicle geometry, the 2D streamlines are influenced also by other effects than merely the vortex, which leads to a disappearing focus structure in the 2D streamlines although the vortex was

still present. This was also observed behind the antenna; hence it is not recommended to look only at the 2D streamline development.

Conclusions from the front wheel flow

The flow downstream of the front wheel is characterized by many different flow interactions and hence the comparison of the experimental and numerical (steady) limiting streamline pattern showed significant differences. Looking at the results from an unsteady simulation showed much better agreement of the near wall flow. However it has to be noted that the main effect towards a more realistic prediction is due to the sliding mesh approach used to simulate the wheel rotation instead of the MRF method. Unsteady surface pressure measurements gave a good insight in the propagation of the near wall flow. It could be shown that two phenomena are present, which are independent from each other. One exiting at the upper wheelhouse area, and one at the lower wheelhouse edge. Studying the correlation signals, further allowed to estimate the propagation direction and speed.

Conclusions from the base wake flow

The analysis of the vehicle base allowed to locate the recirculation stagnation point, from which the near wall flow is distributed over the base. It was also shown that at the trunk edge a crossflow separation takes place, which created a separation surface separating the flow from over the trunk, from the flow inside the recirculation bubble. Further main singular points were found at the lower vehicle side, where two foci on each side occurred. Two other important singular points were less obvious from the first look, but turned out to develop into the dominating trailing vortices. These were the node points of separation occurring at the upper left and right base edges. Analysing the Q criterion in downstream moving crossplanes showed the development of these trailing vortices. Contrary to often cited literature these trailing vortices are not created by the C-pillar crossflow separation. It could be further shown that these vortices always lie outside of the recirculation region. As soon as the recirculation bubble is closed these were able to fully develop into the well known trailing vortices. Hence it can be said, that the trailing vortices and the recirculation area are two individual separation phenomena occurring behind the vehicle base. It is further conjectured that the trailing vortices at the base and the trailing vortices created at the antenna base are similar phenomena. The base wake study also showed that the recirculation zone is successively filled with vorticity created at the vehicle surface and then transported into the wake. This was also indicated by the wall shear stress distribution, which showed very low values on the base. The vorticity analysis further showed that the highest amount of vorticity is created on the trunk surface.

General conclusions

The surface topology gives insight into the resulting flow development. However, its interpretation requires scientific judgement regarding the circumstances. For instance, if the pattern is observed isolated from disturbances or if there are other interactions involved, creating the observed pattern, as it was described for the antenna flow.

It was shown that the flow topology is not Reynolds number dependent and that using a steady state approach was accurate enough in most of the investigated areas. However, in areas characterized by highly unsteady flow interactions as the flow downstream of the wheelhouse, significantly different predictions were observed. If a flow region is dominated by unsteady interactions as downstream of the front wheel, an unsteady approach should be used.

The surface pattern allows to identify evolving phenomena, however it can not be said how strong they are and if and how they can develop into the bulk flow. In general it can be said that flow structures developing in local flow direction are the dominating ones and are the least suppressed. This was for instance shown for the horn separation over the rear window. These appear to be very dominant structures, however they are suppressed quite strongly by the flow over the rear window and trunk.

The analysis of the 2D streamlines can be misleading when they are affected by different phenomena as it was shown for the flow downstream of the antenna or the A-pillar vortex development. Hence it is important to take different parameters into account to reconstruct the full flow field picture. In the investigation under consideration this was done considering the Q criterion together with the x-vorticity distribution.

To identify and predict a crossflow separation an analysis of the limiting streamline pattern together with the surface vorticity is recommended; in particular a specific vorticity component. Distinct jumps in the sign of a vorticity component locate the occurrence of a crossflow separation and give further qualitative insight into its starting point.

The flow around an obstacle can only leave the surface through singular points of separation or through a crossflow separation. As was shown at the rear of the vehicle this implies, that the separation from an edge is a result of a crossflow separation.

Knowing only the limiting streamline pattern, as it can be obtained in experiments by tuft and paint visualisations allows to derive information regarding the surface flow and potential developing separation structures. Singular points and bifurcation lines can be located and by knowing the local flow direction it is also possible to derive if they are of separation or attachment type. Foci structures indicate with their sense of rotation also the sense of rotation of the resulting vortex. Along bifurcation lines it is further possible to qualitatively derive the surface vorticity distribution. Together with the knowledge about the overall flow direction it is even possible to suggest the sense of rotation of potential vortex structures resulting from a crossflow separation.

References

[1] S. Bonitz, L. Larsson, L. Lofdahl, and A. Broniewicz. "Structures of Flow Separation on a Passenger Car". In: *SAE International Journal of Passenger Cars - Mechanical Systems* 8.1 (2015). ISSN: 1946-4002. DOI: 10.4271/2015-01-1529.

[2] S. Bonitz et al. "Experimental Investigation of the Near Wall Flow Downstream of a Passenger Car Wheel Arch". In: *SAE International Journal of Passenger Cars - Mechanical Systems* 11.1 (2018). ISSN: 1946-4002. DOI: 10.4271/06-11-01-0002.

[3] S. Bonitz, L. Larsson, L. Löfdahl, and S. Sebben. "Numerical Investigation of Crossflow Separation on the A-Pillar of a Passenger Car". In: *ASME J. Fluids Eng.* 140.11 (2018). ISSN: 00982202. DOI: 10.1115/1.4040107.

[4] S. Bonitz, L. Larsson, and S. Sebben. "Unsteady Pressure Analysis of the Near Wall Flow Downstream the Front Wheel of a Passenger Car under Yaw Conditions". In: *International Journal of Heat and Fluid Flow* accepted for publication (2018).

[5] S. Bonitz, L. Löfdahl, L. Larsson, and A. Broniewicz. "Investigation of Three-Dimensional Flow Separation Patterns and Surface Pressure Gradients on a Notchback Vehicle". In: *International Vehicle Aerodynamics Conference*. Ed. by IMechE. [S.l.]: Woodhead, 2014, pp. 55–65. ISBN: 9780081001998.

[6] D. Wieser et al. "Surface Flow Visualization on a Full-Scale Passenger Car with Quantitative Tuft Image Processing". In: *SAE 2016 World Congress and Exhibition*. SAE Technical Paper Series. SAE International400 Commonwealth Drive, Warrendale, PA, United States, 2016. DOI: 10.4271/2016-01-1582.

[7] C. Kounenis et al. "Investigations of the Rear-End Flow Structures on a Sedan Car". In: *SAE 2016 World Congress and Exhibition*. SAE Technical Paper Series. SAE International400 Commonwealth Drive, Warrendale, PA, United States, 2016. DOI: 10.4271/2016-01-1606.

[8] S. Bonitz, L. Löfdahl, L. Larsson, and A. Broniewicz. "Flow Structure Identification over a Notchback Vehicle". In: *International Conference on Vehicle Aerodynamics*. Ed. by IMechE. Woodhead, 2016.

[9] D. Wieser et al. "Quantitative Tuft Flow Visualization on the Volvo S60 under realistic driving Conditions". In: *54th AIAA Aerospace Sciences Meeting*. AIAA

SciTech. American Institute of Aeronautics and Astronautics, 2016. DOI: 10.2514/6.2016-1778. URL: http://dx.doi.org/10.2514/6.2016-1778.

[10] H. Helmholtz. "Über diskontinuierliche Flüssigkeits-Bewegungen". In: *Monatsberichte der Königlich Preussischen Akademie der Wissenschaft zu Berlin*. 1968, pp. 215–228.

[11] A. Leder. *Abgelöste Strömungen: Physikalische Grundlagen*. Grundlagen und Fortschritte der Ingenieurwissenschaften. Braunschweig and Wiesbaden: Vieweg, 1992. ISBN: 978-3-528-06436-5.

[12] R. H. Aungier. *Turbine Aerodynamics: Axial-Flow and Radial-Flow Turbine Design and Analysis*. Three Park Avenue New York, NY 10016-5990: ASME, 2006. ISBN: 0791802418. DOI: 10.1115/1.802418.

[13] T. Wang. "A brief review on wind turbine aerodynamics". In: *Theoretical and Applied Mechanics Letters* 2.6 (2012), p. 062001. ISSN: 20950349. DOI: 10.1063/2.1206201.

[14] G. Corten. *Flow separation on wind turbine blades*. 2001. ISBN: 90-393-2582-0.

[15] T. V. Lawson, ed. *Building aerodynamics*. London: Imperial College Press, 2002. ISBN: 978-1-86094-187-0. DOI: 10.1142/p161.

[16] W.-H. Hucho. *Aerodynamik der stumpfen Körper: Physikalische Grundlagen und Anwendungen in der Praxis ; mit 56 Tabellen*. 2nd ed. ATZ-MTZ Fachbuch. Wiesbaden: Vieweg + Teubner, 2011. ISBN: 978-3-8348-1462-3.

[17] L. Larsson, H. C. Raven, and J. R. Paulling. *Ship resistance and flow*. Principles of naval architecture. Jersey City, N.J.: Society of Naval Architects and Marine Engineers, 2010. ISBN: 978-0-939773-76-3.

[18] D. Liepsch. "An introduction to biofluid mechanics—basic models and applications". In: *Journal of Biomechanics* 35.4 (2002), pp. 415–435. ISSN: 00219290. DOI: 10.1016/S0021-9290(01)00185-3.

[19] J. Mazumdar, S. Sircar, A. Saha, and K. Wong. *Biofluid mechanics*. 2nd ed. Singapore: World Scientific Publishing Co. Pte. Ltd, 2016. ISBN: 9814719005.

[20] G. Maier et al. *Sport Aerodynamics*. Vol. 506. Vienna: Springer Vienna, 2008. ISBN: 978-3-211-89296-1. DOI: 10.1007/978-3-211-89297-8.

[21] T. N. Crouch, D. Burton, Brown, N. A. T., M. C. Thompson, and J. Sheridan. "Flow topology in the wake of a cyclist and its effect on aerodynamic drag". In: *Journal of Fluid Mechanics* 748 (2014), pp. 5–35. ISSN: 0022-1120. DOI: 10.1017/jfm.2013.678.

[22] R. H. Barnard. *Road vehicle aerodynamic design: An introduction*. St. Albans: MechAero Publ., 2009. ISBN: 0954073479.

[23] T. Schütz, ed. *Hucho Aerodynamik des Automobils*. [s.l.]: Springer, 2013. ISBN: 3834819190.

[24] E. C. Maskell. *Flow Separation in Three Dimensions*. Aero 2565. RAE Report, 1955.

[25] R. L. Panton. *Incompressible flow*. Third edition. Wiley, 2005. ISBN: 1118713079.

[26] J.-Z. Wu, H.-Y. Ma, and M.-D. Zhou. *Vorticity and Vortex Dynamics*. Berlin, Heidelberg: Springer Berlin Heidelberg, 2006. ISBN: 978-3-540-29027-8. DOI: 10.1007/978-3-540-29028-5.

[27] V. Kolář. "Vortex identification: New requirements and limitations". In: *International Journal of Heat and Fluid Flow* 28.4 (2007), pp. 638–652. DOI: 10.1016/j.ijheatfluidflow.2007.03.004.

[28] J. C. Hunt, A. Wray, and P. Moin. "Eddies, stream, and convergence zones in turbulent flows". In: *Center for turbulence research report CTR-S88* (1988), pp. 193–208.

[29] L. Prandtl. *The mechanics of viscous fluids. Aerodynamic Theory, WF Durand (Ed.), Vol. 3*. 1924.

[30] D. J. Tritton. *Physical fluid dynamics*. 2nd ed. Oxford science publications. Oxford [England], New York: Clarendon Press and Oxford University Press, 1988. ISBN: 978-0-19-854493-7.

[31] E. Eichelbrenner and A Oudart. *Observations sur un critère de décollement laminaire dans la couche-limite tridimensionnelle*. 1954.

[32] E. Eichelbrenner and A Oudart. *Le décollement laminaire en trois dimensions*. 1955.

[33] Lighthill M. J. "Attachment and separation in three dimensional flows". In: *Laminar boundary layers*. Ed. by L. Rosenhead. Dover books on physics and chemistry. New York: Dover Publications, 1988, c1963, pp. 72–76. ISBN: 9780486656465.

[34] M. Tobak and D. J. Peake. "Topology of Three-Dimensional Separated Flows". In: *Annual Review of Fluid Mechanics* 14.1 (1982), pp. 61–85. ISSN: 0066-4189. DOI: 10.1146/annurev.fl.14.010182.000425.

[35] H. Werle. "Separation on axisymmetrical bodies at low speed". In: *La Recherche Aeronautique* 90 (1962), pp. 3–14.

[36] G. T. Chapman and L. A. Yates. "Topology of Flow Separation on Three-Dimensional Bodies". In: *Applied Mechanics Reviews* 44.7 (1991), p. 329. ISSN: 00036900. DOI: 10.1115/1.3119507.

[37] J. Z. Wu, R. W. Tramel, F. L. Zhu, and X. Y. Yin. "A vorticity dynamics theory of three-dimensional flow separation". In: *Physics of Fluids* 12.8 (2000), p. 1932. ISSN: 10706631. DOI: 10.1063/1.870442.

[38] A. Surana, O. Grunberg, and G. Haller. "Exact theory of three-dimensional flow separation. Part 1. Steady separation". In: *Journal of Fluid Mechanics* 564 (2006), pp. 57–102. ISSN: 0022-1120. DOI: 10.1017/S0022112006001200.

[39] J. Sternéus, T. Walker, and T. Bender. "Upgrade of the Volvo Cars Aerodynamic Wind Tunnel". In: Paper No: 2007-01-1043. Warrendale and PA: SAE International, 2007. DOI: 10.4271/2007-01-1043.

[40] P. Elofsson and M. Bannister. "Drag Reduction Mechanisms Due to Moving Ground and Wheel Rotation in Passenger Cars". In: *SAE 2002 World Congress & Exhibition*. SAE Technical Paper Series. Warrendale, PA: SAE International, 2002. DOI: 10.4271/2002-01-0531.

[41] E. Mercker and H. W. Knape. "Ground Simulation with Moving Belt and Tangential Blowing for Full-scale Automotive Testing in a wind Tunnel". In: Warrendale, PA: SAE International, 1989. DOI: 10.4271/890367.

[42] E. Mercker, N. Breuer, H. Berneburg, and H. J. Emmelmann. "On the Aerodynamic Interference Due to the Rolling Wheels of Passenger Cars". In: Warrendale, PA: SAE International, 1991. DOI: 10.4271/910311.

[43] E. Mercker, H. Soja, and J. Wiedemann. "Experimental investigations on the Influence of Various Ground Simulation Techniques on a Passenger Car". In: Conference on Vehicle Aerodynamics. Proceedings Roy. Aer.Soc, 1994.

[44] G. Wickern. "The Effect of Moving Ground on the Aerodynamic Drag of a Production Car". In: *SATA Conference*. 1991.

[45] E. Ljungskog. "Investigations of Flow Conditions in an Automotive Wind Tunnel". Licentiate Thesis. URL: http://publications.lib.chalmers.se/publication/249000-investigations-of-flow-conditions-in-an-automotive-wind-tunnel (visited on 10/16/2017).

[46] L. Sterken. *Analysis of the unsteady flow field of a passenger vehicle*. Vol. 3870. Doktorsavhandlingar vid Chalmers tekniska högskola. Ny serie. Göteborg: Chalmers University of Technology, 2015. ISBN: 9175971895.

[47] S. Vey, H. M. Lang, C. N. Nayeri, C. O. Paschereit, and G. Pechlivanoglou. "Extracting quantitative data from tuft flow visualizations on utility scale wind turbines". In: *Journal of Physics: Conference Series* 524 (2014), p. 012011. ISSN: 1742-6596. DOI: 10.1088/1742-6596/524/1/012011.

[48] D. Wieser, H. Lang, C. Nayeri, and C. Paschereit. "Manipulation of the Aerodynamic Behavior of the DrivAer Model with Fluidic Oscillators". In: *SAE International Journal of Passenger Cars - Mechanical Systems* 8.2 (2015). ISSN: 1946-4002. DOI: 10.4271/2015-01-1540.

[49] R. Martinuzzi and C. Tropea. "The Flow Around Surface-Mounted, Prismatic Obstacles Placed in a Fully Developed Channel Flow (Data Bank Contribution)". In: *ASME J. Fluids Eng.* 115.1 (1993), p. 85. ISSN: 00982202. DOI: 10.1115/1.2910118.

[50] J. C. R. Hunt, C. J. Abell, J. A. Peterka, and H. Woo. "Kinematical studies of the flows around free or surface-mounted obstacles; applying topology to flow visualization". In: *Journal of Fluid Mechanics* 86.01 (1978), p. 179. ISSN: 0022-1120. DOI: 10.1017/S0022112078001068.

[51] R. L. Simpson. "Junction Flows". In: *Annual Review of Fluid Mechanics* 33.1 (2001), pp. 415–443. DOI: 10.1146/annurev.fluid.33.1.415.

[52] F. Chometon. "Simultaneous Use Of Oil-Flow Patterns And Total Pressure Tomographies For A More Complete Understanding Of Flow Structures Around A Car". In: Warrendale, PA: SAE International, 1988. DOI: 10.4271/885137.

[53] L. N. Jenkins. "An Experimental Investigation of the Flow Over the Rear End of a Notchback Automobile Configuration". In: Warrendale, PA: SAE International, 2000. DOI: 10.4271/2000-01-0489.

[54] B. R. Gilhome, J. W. Saunders, and J. Sheridan. "Time Averaged and Unsteady Near-Wake Analysis of Cars". In: Warrendale, PA: SAE International, 2001. DOI: 10.4271/2001-01-1040.

[55] S. Depardon, J. J. Lasserre, L. E. Brizzi, and J. Borée. "Scale VehicleWake Pattern Analysis using Near-Wall PIV". In: Warrendale, PA: SAE International, 2006. DOI: 10.4271/2006-01-1027.

[56] A. P. Gaylard, J. P. Howell, and K. P. Garry. "Observation of Flow Asymmetry Over the Rear of Notchback Vehicles". In: Warrendale, PA: SAE International, 2007. DOI: 10.4271/2007-01-0900.

[57] D. Wieser et al. "Experimental Comparison of the Aerodynamic Behavior of Fastback and Notchback DrivAer Models". In: Warrendale, PA: SAE International, 2014. DOI: 10.4271/2014-01-0613.

[58] D. Sims-Williams, D. Marwood, and A. Sprot. “Links between Notchback Geometry, Aerodynamic Drag, Flow Asymmetry and Unsteady Wake Structure”. In: *SAE Int. J. Passeng. Cars – Mech. Syst.* 4 (2011). DOI: 10.4271/2011-01-0166. URL: http://dx.doi.org/10.4271/2011-01-0166.

[59] L. J. Janssen and W. H. Hucho. “Aerodynamische Formoptimierung von VW Golf und VW Scirocco”. In: *AUTOMOBILTECHN Z* 77.11 (1974), pp. 49–70.

[60] C. Hoarau, J. Borée, J. Laumonier, and Y. Gervais. “Unsteady wall pressure field of a model A-pillar conical vortex”. In: *The Fifth International Symposium on Turbulence and Shear Flow Phenomena (TSFP5)* 29.3 (2008), pp. 812–819. ISSN: 0142-727X. DOI: 10.1016/j.ijheatfluidflow.2008.02.015.

[61] J. Howell, J. B. Fuller, and M. Passmore. “The Effect of Free Stream Turbulence on A-pillar Airflow”. In: *SAE World Congress & Exhibition*. SAE International, 2009. DOI: 10.4271/2009-01-0003. URL: https://doi.org/10.4271/2009-01-0003.

[62] B. Levy, P. Brancher, and A. Giovannini. “Experimental characterization of the velocity and wall pressure fields of an A-pillar vortex”. In: *14th AIAA/CEAS Aeroacoustics Conference (29th AIAA Aeroacoustics Conference)* (2008). URL: https://www.scopus.com/inward/record.uri?eid=2-s2.0-78249269843&partnerID=40&md5=6c86d1db3c9652d01bec377705872f89.

[63] B. Levy and P. Brancher. “Topology and dynamics of the A-pillar vortex”. In: *Physics of Fluids* 25.3 (2013), p. 037102. ISSN: 1070-6631. DOI: 10.1063/1.4792710.

[64] B. Levy and P. Brancher. “Experimental investigation of the wall dynamics of the A-pillar vortex flow”. In: *Journal of Fluids and Structures* 55 (2015), pp. 540–545. ISSN: 0889-9746. DOI: 10.1016/j.jfluidstructs.2015.03.020.

[65] Ahmed and W. Baumert. “The structure of wake flow behind road vehicles”. In: *Joint ASME-CSME Applied Mechanics, Fluids Engineering, and Bioengineering Conference: Aerodynamics of Transportation, Niagara Falls, NY*. 1979, pp. 93–103.

[66] S. R. Ahmed. “Wake Structure of Typical Automobile Shapes”. In: *Journal of Fluids Engineering* 103.1 (1981), p. 162. ISSN: 00982202. DOI: 10.1115/1.3240767.

[67] S. R. Ahmed. “Influence of Base Slant on the Wake Structure and Drag of Road Vehicles”. In: *Journal of Fluids Engineering* 105.4 (1983), p. 429. ISSN: 00982202. DOI: 10.1115/1.3241024.

[68] T. Nouzawa, K. Hiasa, M. Yoshimoto, and S. Haruna. “Influence of Geometry of Rear part on the Aerodynamic Drag and Wake Structure of a Vehicle”. In: 1987.

[69] T. Nouzawa, S. Haruna, K. Hiasa, T. Nakamura, and H. Sato. “Analysis of Wake Pattern for Reducing Aerodynamic Drag of Notchback Model”. In: Warrendale, PA: SAE International, 1990. DOI: 10.4271/900318.

[70] T. Ivanic and P. Gilliéron. “Aerodynamic drag and ways to reduce it”. In: *LECTURE SERIES-VON KARMAN INSTITUTE FOR FLUID DYNAMICS* 5 (2005), p. 2.

[71] T. Hobeika and S. Sebben. “CFD investigation on wheel rotation modelling”. In: *Journal of Wind Engineering and Industrial Aerodynamics* 174 (2018), pp. 241 –251. ISSN: 0167-6105. DOI: https://doi.org/10.1016/j.jweia.2018.01.005. URL: http://www.sciencedirect.com/science/article/pii/S0167610517307286.

[72] T. Hobeika. “Wheel modelling and cooling flow effects on car aerodynamics”. PhD thesis. Gothenburg, Sweden, 2018.